AN ABSTRACT OF THE THESIS OF

Kristin Noel Duckworth Richardson for the degree of Master of Science in Water Resources Science presented on February 9, 2017.

Title: Role of Extreme Events on Sedimentation in Loon Lake, Oregon Coast Range, USA.

Abstract approved:

_____

Robert A. Wheatcroft Jeff A. Hatten

Sediment cores were retrieved from a landslide-dammed lake, recording events back to the 5th century AD in a forested, mountainous catchment. These cores provide an opportunity to compare the impacts of known recent perturbations, including floods and timber harvesting with those of the early period of the core, flood, fire, and earthquake. A multi-parameter approach was used to measure characteristics of sediment with high-resolution grain size, %TC, %TN, and magnetic susceptibility analysis. ^{137}Cs atmospheric deposition and radiocarbon dating techniques were used for age control, as well as a varved record in the last 75 years. The estimated mean mass accumulation rate from 1939 to 1978 AD, the time of peak timber harvest and a cool wet phase of the Pacific Decadal Oscillation (PDO), was 0.79 (0.74-0.92) g cm^{-2} y^{-1}, significantly higher than estimated mean rates of both the more recent contemporary period, 1979-2012 AD, at 0.58 (0.48-0.70) and the entire early period, 0.44 (0.41-0.46). Several event beds are coeval with estimated ages of eight Cascadia subduction zone earthquakes in the early period, including the 1700 AD M_w 9.0 earthquake. These beds are predominantly hyperpycnites, as are the known flood deposits in the contemporary period, with the exception of one debris flow within a 23-cm thick event bed deposited at approximately 700 AD. The high mass accumulation rate and high concentration of thick event beds and layers during the early contemporary period point to the extraordinary role of timber harvesting in priming the landscape for subsequent sedimentary delivery during floods.

Role of Extreme Events on Sedimentation in Loon Lake, Oregon Coast Range, USA

by
Kristin Noel Duckworth Richardson

A THESIS

submitted to

Oregon State University

in partial fulfillment of
the requirements for the
degree of

Master of Science

Presented February 9, 2017
Commencement June 2017

Master of Science thesis of Kristin Noel Duckworth Richardson presented on February 9, 2017.

APPROVED:

_____

Co-Major Professor, representing Water Resources Science

_____

Co-major Professor, representing Water Resources Science

_____

Director of the Water Resources Graduate Program

_____

Dean of the Graduate School

I understand that my thesis will become part of the permanent collection of Oregon State University libraries. My signature below authorizes release of my thesis to any reader upon request.

_____

Kristin Noel Duckworth Richardson, Author

ACKNOWLEDGEMENTS

The author expresses sincere appreciation of advisors Dr. Rob Wheatcroft and Dr. Jeff Hatten and other committee members, Dr. Joe Stoner and Dr. Phil Mote. Dr. Wheatcroft and Dr. Hatten were dedicated to retrieving cores, to discussing key concepts throughout the research, and to providing learning opportunities. Dr. Stoner provided valuable information on magnetic susceptibility and lake sediment studies in general. Dr. Mote supported the exam process as the Graduate Council Representative.

Beyond the structure and foundation set by the committee, other individuals, groups, and agencies contributed both small and large amounts of time, equipment, effort, and expertise. The author expresses gratitude for the following:

Those who participated in coring: Franco Bolaño Guerrero, Ken Richardson, Christine Wheatcroft, Max Taylor, Laura Woodbury, Greta Krost for Coos Bay District Bureau of Land Management (BLM)

OSU faculty, staff, and labs: Dr. Mary Santelmann, Director of Water Resources Graduate Program; Dr. Wheatcroft's Sediment Dynamics Lab and group; Dr. Hatten's Forest Soils Lab and group and manager Yvan Alleau; Miguel Goni's geochemistry lab; Fred Prahl's lab; National Science Foundation Marine Geology Repository and staff; College of Forestry statistics support Ariel Muldoon

Other agencies and labs: National Energy and Technology Lab, Albany, Oregon, Kelly Rose and Corinne Disenhof; University of Washington Chuck Nittrouer and lab group; University of Minnesota LacCore Lab and Anders Noren; Weyerhauser, Maryanne Reiter, hydrologist; NOSAMS Woods Hole Oceanographic Institute; BLM - Coos Bay District, Mike Kelly and staff

Those who provided feedback at various phases of the research: Dan Gavin, Patrick Pringle, Jerry Phillips, Ray Simms, Ann Morey Ross, Sarah Lewis, Fred Swanson, Catalina Segura, Bill Burns

Funding entities: EPA grant #83518602 for research assistantship and material funds; College of Earth, Ocean, and Atmospheric Sciences (CEOAS) teaching assistantship

Family and friends: Ken Richardson, who took care of almost every aspect of life so the author could focus on this research, Zion Richardson (technology/software advising), Venice Richardson (lab help, canoeing), Mom (every lake adventure), Karen and Andy Nousen and Richardson family (exploring the landslide scarp, spending a week at the lake), Kim Braasch (site exploration and inspiration), Dad and Nora Duckworth (unending motivation)

TABLE OF CONTENTS

LIST OF FIGURES

LIST OF TABLES

LIST OF APPENDICES

LIST OF APPENDIX FIGURES

LIST OF APPENDIX TABLES

Role of Extreme Events on Sedimentation in Loon Lake, Oregon Coast Range, U.S.A.

CHAPTER 1 -- INTRODUCTION

As sedimentary sinks, lakes are an important component of the earth's sediment-routing system, in which mineral matter is eroded from the hinterlands, moved to fluvial systems, and delivered to lowland sinks and the ocean. Since lakes capture the eroded and delivered sediment, they have the potential to record events in the catchment within their accumulating sediment. Within mountains at tectonically active continental margins, where climate physically and chemically interacts with an uplifting critical zone, erosion rates can be high (e.g., 0.05 to 0.3 mm y^{-1} in Oregon Coast Range; Reneau and Deitrich, 1991; Heimsath et al., 2001). As climate can act as an abrupt perturbation to the landscape in the form of extreme storms and wet periods, so can earthquakes and denudation of vegetation on the landscape by fire and anthropogenic land clearance. Small mountainous river systems in such regions deliver ~50% of the world's total fluvial sediment to the oceans (Milliman & Syvitski, 1992). Therefore, lakes in these environments are in a strategic location to capture an integrated record in the sedimentary stratigraphy of this sediment routing system and its response to and censoring of erosion and subsequent delivery of sediment driven by extreme events within its catchment. Possessing such a sedimentary record and being able to decipher its meaning contributes to an understanding of earth system processes over a broad range of timescales, including the human time scale (Allen, 2008).

Scientists' ability to look into this record to understand events within the catchment and sediment delivery mechanisms partly depends upon the stratigraphic fidelity; that is, how well the deposition reflects characteristics of unique events (e.g. Wheatcroft et al., 1990; Jerolmack and Paola, 2010; Romans et al., 2016). The degree to which the stratigraphy records the timing and magnitude of the actual events depends on many factors, both within the sediment-routing system (Allen, 2008) and the lake system itself (Schillereff et al., 2016). For several reasons, lakes can provide a high-fidelity record of events in a catchment. As an inland sink, a lake has accommodation space to trap a high proportion of inflowing particulates from the catchment

(Owens & Slaymaker, 1993). It is energetically and hydrodynamically unfavorable to transport material out of the lake basin once sediments are settled (Wetzel, 2001), especially if the lake is deep (Dearing, 1991). Additionally, a low-oxygen bottom water and sediment environment has been shown to lead to preservation of sediment layers in lakes (e.g., Edmondson, 1991; Page et al., 1994, 2010), because of the low intensity of bioturbation. The relatively small catchment area-to-sink area ratio of a lake allows a rapid response to environmental changes and forcing variables, and there is a high degree of depositional continuity (Cohen, 2003; Beck, 2009). Lastly, sediment accumulation can be rapid (e.g., 0.08 -4 cm y^{-1}), resulting in higher resolution (Cohen, 2003; Orpin et al., 2010), sometimes seasonal or annual, and often decadal.

Lakes not only record events in the catchment but also record autochthonous processes. Lakes contain micro-habitats, where myriad biological and biogeochemical processes occur. Aquatic flora, fauna, and algae thrive in these habitats and their decomposing mass and by-products settle to the bottom of the lake (Dodson, 2005). Allochthonous inputs such as dust, pollen and leaves from nearby vegetation, and elemental particulate and minerogenic matter from fluvial inputs are integrated in the lake. These are all manifest in the sediments, often on a seasonal basis as annually deposited layers, i.e., varves (Zolitschka et al., 2015). In-lake physical processes, such as seasonal water column mixing and stratification also influence aquatic conditions and sediment deposition (Whitlock et al., 2008), as can occasional episodic subaqueous deltaic or steep slope failures (e.g. Karlin et al., 2004; Page et al., 2010) which re-suspends sediment.

The purpose of this research was to investigate changes in sedimentation in a lake in the Oregon Coast Range whose catchment has been heavily impacted by land clearance, especially timber harvest, and road building since the early 20th century. By obtaining sediment cores spanning the past ~1500 years, we were able to compare the relative contributions of sediment production and delivery by the four major perturbations within this catchment, earthquakes, forest fire, flood, and human impact, and to address the following questions and hypotheses: How are these forcings recorded in the lake sediment, i.e., what is the structure of the recorded beds, and

what is their frequency? What role do large hydrologic events have in the sedimentation of the lake? We hypothesized that earthquakes would be recorded since this work is conducted within the Cascadia subduction zone (CSZ), but asked the question: how are they manifested? Also, how does sediment accumulation rate (SAR) change in response to events and through time? Finally, can the effects of timber harvest and changes in forestry practices after 1972 be detected within the sedimentary column? We hypothesized that timber harvesting would increase sediment accumulation rates, and that improvements in forest harvest practices would result in lower SAR. An annually-resolved record in the last 75 years allows a narrative of the interaction of hydrologic and anthropogenic forcings in the contemporary period, and a window to an understanding of the forcings in the past, represented by the stratigraphy of the early period within the longest cores.

CHAPTER 2 – METHODS

2.1 Study area

Loon Lake (43.585º N, 123.839º W), a 4-km long landslide-dammed lake, is perched at 128 m a.s.l within the Oregon Coast Range (OCR) 30 km east of the Pacific Ocean (Figure 1). It has a surface area of 1.2 km^2, and lies within the coniferous western hemlock (*Tsuga heterophylla*) vegetation zone (Franklin and Dyrness, 1988). The 230-km^2 catchment has a relief of 680 m, and is underlain by both Tyee and Elkton formations (Baldwin, 1974), which contain rhythmic, thickly bedded sandstone and interbedded carbonaceous siltstone. Within these steep and deeply dissected mountains, shallow landslides and debris flows dominate the sediment transport out of unchanneled valleys on low-order tributaries (i.e. Dietrich & Dunne, 1978; Heimsath et al., 2001). Other processes, such as tree-throw (Roering et al., 2010) and bioturbation (Heimsath et al., 2001), also contribute to soil production and transport. Bedrock landslides (deep-seated) such as that which formed Loon Lake within the Tyee formation of the OCR (Baldwin, 1958, 1981; Beaulieu and Hughes, 1975), also act as geomorphic agents in these mountains (Lane, 1987; Roering et al., 2005).

In Cascadia, at the northwestern margin of the North American continent, natural forcings are numerous. These may be recorded in sedimentary sinks in the region: extreme floods, megathrust subduction zone earthquakes, and fire. Winter storms saturate the soil in the winter and provide impetus for sediment transport. Occasionally, high intensity and/or long-duration rainfall saturates the landscape as episodic and frontal storms termed ‘atmospheric rivers’ (Ralph & Dettinger, 2012), punctuating usual winter time low-intensity precipitation. Water years (WY) 1965, 1982, 1996, and 1997 were the most recent extreme precipitation events in this area (Table A1). Average annual precipitation in Loon Lake catchment is 1700-2400 mm y^{-1} (Figure 1), falling mostly as rain primarily in November – April, with very dry summers. Winter storminess is influenced by decadal-scale oscillations of Pacific Decadal Oscillation (PDO; Mantua et al., 1997).

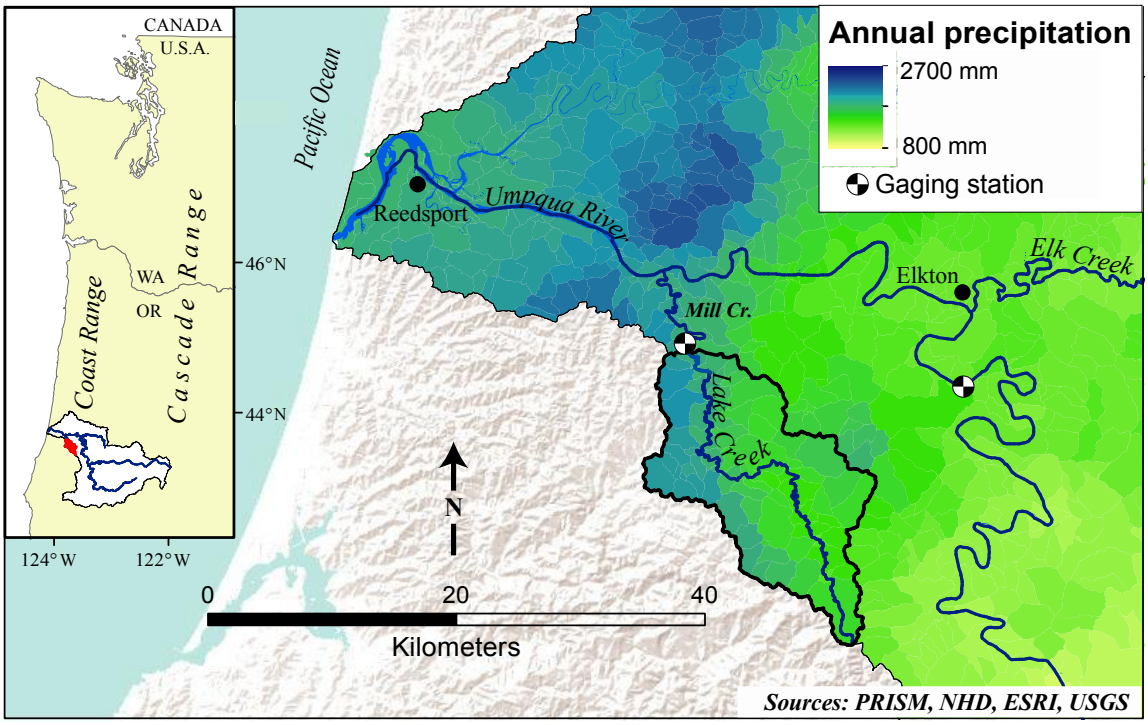

Figure 1. Lower Umpqua River Basin and precipitation. Loon Lake catchment is red on the regional map (left), and outlined in black on the Umpqua basin and precipitation map. Loon Lake is at the north end of the catchment, south of the gaging station at Mill Creek (USGS #14323000). Elkton gaging station (USGS# 14321000) is ~20 km east of Loon Lake catchment. Sources: PRISM Climate Group, National Hydrology Data set (NHD), Environmental Systems Research Institute (ESRI), 1998.

Lying within the Cascadia subduction zone (CSZ), Loon Lake catchment has experienced several earthquakes resulting from full- and possibly partial-rupture of the fault boundary (USGS, 2012). These megathrust earthquakes periodically shake the regolith (Nelson et al., 2006) at a recurrence interval of between 260 and 600 years, depending on along-margin location (Witter et al., 2012), and have magnitudes estimated to range from 8 to 9.0 (Goldfinger et al., 2012) during the estimated existence of Loon Lake. Because the ground shaking can weaken the substrate of an entire basin, it serves to prime it for co- or post-seismic landsliding (Crozier, 1986; Dadson, 2004; Hovius et al., 2011). Research globally has shown that for years to decades following earthquakes, landslides may persist due to the weakening of the substrate and lowering of a threshold for failure (Hovius et al., 2011; Howarth et al., 2012). For example, landsliding

increased in mountains of Taiwan following the 1999 AD Chi-Chi earthquake. Intense typhoons in 2001 further increased landsliding, and increased sediment loads in rivers.

Fire in the Coast Range ecosystem prior to anthropogenic suppression recurred every 230 +/- 30 years (Long et al., 2007). Debris flows after fire increase immediately and for years (May and Gresswell, 2003; Swanson, 1981), and may account for a significant fraction, 10% – 25%, of the long-term erosion in the OCR (Swanson, 1981; Roering & Gerber, 2005; Jackson & Roering, 2009). Forest fires can leave the hillslopes more susceptible to landsliding than would otherwise have been with forest cover and healthy root reinforcement (Reneau and Dietrich, 1989; Montgomery et al., 2000; Roering and Gerber, 2005; Jackson and Roering, 2009). The only large fires in the catchment historically recorded and inferred through dendrochronology occurred at about 1765 and 1868 AD (Morris, 1934; Zybach, 2003; ODF, 2011). Given that the last large significant fire occurred in 1868 AD, and that the last CSZ earthquake occurred in 1700 AD, the catchment has been free of these two disturbances for ~150 y.

Land clearance, timber harvest, road building, and associated activities have impacted the catchment since the late 19th century (Table A1). These activities have been shown regionally to increase erosion and alter peak flows (Beschta, 1978; Jones & Grant, 1996), increase sediment production and delivery (Reid and Dunne, 1984; Montgomery et al., 2000), and compact soil and decrease infiltration rates, leading to surface erosion (Johnson & Beschta, 1980). At the time of peak logging in much of western Oregon in the 1960s, increases in sediment accumulation rates were shown to occur in the offshore margin near the mouth of the Umpqua River (Wheatcroft et al., 2013), and were attributed to timber harvest. Although timber was being harvested around the lake early in the century (USDI, 2005), it did not begin in earnest until the 1940's in the Elliott State Forest and BLM lands (USDI, 2005) as well as in the upper catchment (Sims, 1998; Phillips, 2015, pers. com.). During this time the lake was used as a log dump into the 1950's (USDI, 2005; Phillips, 2015, pers. com.). In the 1960's, timber harvest sharply increased by the largest landowner, a private company (Figures 2a, A1), and by 1971, about 20% of the catchment had been harvested. From 1972 to 2012, ~50% more of the entire Loon Lake

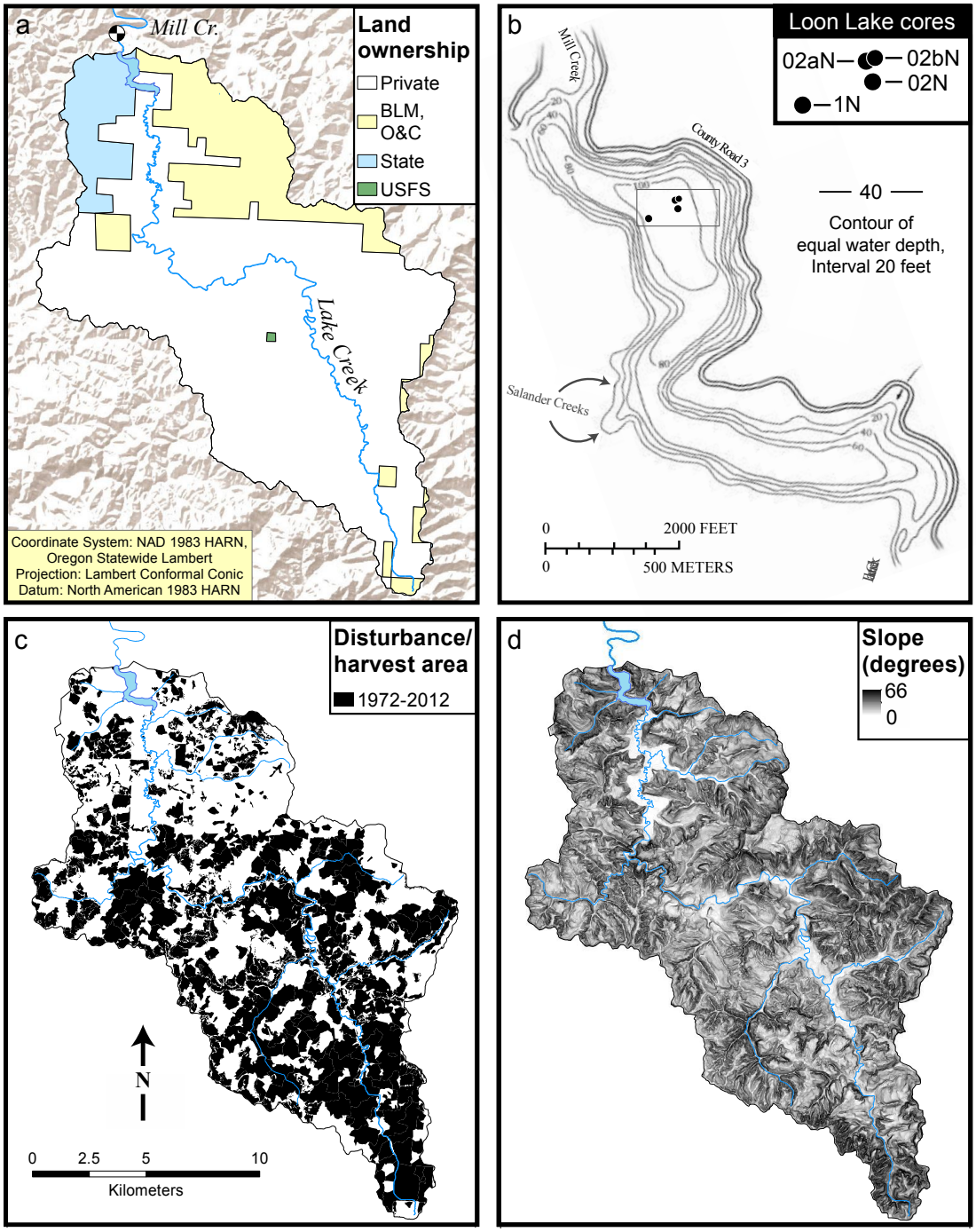

Figure 2. Loon Lake catchment: land ownership, lake bathymetry, harvest, slope. a) Land ownership and Mill Creek gaging station location. b) Loon Lake bathymetry and core locations of key cores (map adapted from Rinella, 1979 and Curtiss et al., 1984). c) Harvest area 1972-2012 AD detected by remote sensing (Cohen et al., 2002, Kennedy et al, 2012). d) Slope of terrain; flat valley south and above lake (shown as white) is probably the old lake bed.

catchment had been harvested (Figure 2c), reaching peak harvest here in the 1970's (Appendix A1, A2).

Several years before peak logging, the 1971 Oregon Forest Practices Act was passed (Oregon, 2001), and as a result, rules on best management practices (BMP's) in timber harvest on state and private lands began to be implemented in 1972 (Hairston-Strang et al., 2008). This may have helped prevent some erosion and stream damage by improving harvest activities and road building. It is assumed that conditions improved but that there would have been a lag in time before practices lessened soil and water impacts.

Another source of sediment by anthropogenic influence has been contributed since Euro-American settlement in the alluvial Ash Valley above the lake, which was previously lake surface, now filled in (Baldwin, 1958; Figure 2d). This flat-bottomed valley was converted from hardwood forest to pasture and partly drained. The alluvial fill is a constant source of sediment, especially during high discharge events, as meandering Lake Creek erodes its unvegetated banks on the way to the lake (USDI, 2005).

Physical properties of the lake itself provide additional information on sedimentation. The lake's formation date is often cited as 1460 +/- 80 y BP by a conventional ^{14}C date on submerged wood (Fergusson and Libby, 1962). The lake has an average and maximum depth of 16 and 32 m, respectively, and flows out over the sandstone landslide-debris dam as Mill Creek (Figure 2a-d). The lake develops a strong thermocline in the summer and becomes isothermal in the winter (Curtiss et al., 1984). During and following high-discharge precipitation events, the lake level rises and the water becomes turbid for days to months (Sims, 1998; personal observation). Beyond episodic storm turbidity, water quality is a concern. During the time the lake was used as a log dump, the water color was said to be brown (Sims, 1998; Phillips, pers. com., 2015). The likely effect of rapid extinction of light at shallow depths may have had an effect on the lake bottom water and sediment (Schuytema and Shankland, 1976; Appendix A4). In November 1977, the USGS measured dissolved oxygen and other parameters, and found the water at the bottom of the lake (hypolimnion) to be anoxic (Rinella, 1979). In the 1980's it was noted that algae

populations in the water column increased in the summer and that dissolved oxygen was again depleted in the hypolimnion (Curtiss et al.,1984). Finally, the lake was shown to be somewhat productive (mesotrophic) in the 1990s (ODEQ, 1992).

A gaging station on Mill Creek measured daily discharge for 7 years in 1907-1917 (Figure 2a), and during this time, recorded a high of 283 $m^3 s^{-1}$ in November 1909, during a coastal-region extreme precipitation event (e.g., Eilers, 1996). This flow was an order of magnitude higher than the typical winter discharge, and five orders of magnitude higher than typical summer low flows.

2.2 Coring

Three sampling expeditions in 2013 yielded a collection of twenty cores (Table 1). A Nesje piston corer (Nesje, 1992) was used to recover the two longest cores (02aN and 02bN, 6.26 and 7.03 m in length, respectively), which were taken in the deepest basin approximately 5 m apart. These act as parallel companion cores, and most of the sediment analyses was done with these and gravity cores also from the deep basin (02N and 1N; Figure 2b). The long Nesje cores were cut at the field site in a minimal number of pieces usually > 1.5 m in length, and, for the two parallel cores, at different lengths to preserve representation of all stratigraphy. During the cutting process, some mass of sediment was lost at each cut due to the release of pressure, and most of this sediment was captured, bagged, and labeled on-site, and weighed later. This mass represents up to 1.8% of the linear length of the core, and was not used for any analysis, and not considered in any further calculations. Cores were placed in an upright position until cut and split, and were refrigerated at 3°C upon return to the Oregon State University Marine and Geology Repository (OSU-MGR) within approximately 9 hours after coring, or less when refrigeration was available at the field site.

Table 1. List of sediment cores retrieved from Loon Lake. Coring devices used were Nesje percussion piston corer (PC; Nesje, 1992), large-diameter gravity corer (GC), and a Wildco K-C gravity corer (W-GC).

Core name	Date taken	Inner core diameter (cm)	Original length (m)	Latitude (ºN)	Longitude (ºW)	Depth of water (m)	Coring device
01aS	9/11/13	7.3	4.3	43.59045	123.83855	28	PC
02aN	9/12/13	7.3	7.03	43.59166	123.83901	31	PC
02bN	9/12/13	7.3	6.26	43.59165	123.83907	31	PC
01S	9/13/13	10.1	1.92	43.59042	123.83839	28	GC
02N	9/13/13	10.1	1.67	43.59139	123.83894	31	GC
03S	9/13/13	10.1	1.77	43.59016	123.83820	28	GC
1S	7/23/13	10.1	0.6	43.5896	123.83923	31	GC
1N	9/9/13	10.1	1.32	43.59101	123.84047	31	GC
1TU	9/10/13	10.1	0.89	43.5816	123.83257	20	GC
2TU	9/10/13	10.1	1.03	43.58269	123.83805	20	GC
3bTU	9/10/13	10.1	1.08	43.58647	123.83863	24	GC
4TS	9/10/13	10.1	1.3	43.59033	123.83866	29	GC
5TN	9/10/13	10.1	0.41	43.59219	123.84155	30	GC
2RU	4/19/13	5.0	0.48	43.5826	123.83849	23	W-GC
3RU	4/19/13	5.0	0.50	43.58474	123.84013	22	W-GC
4RS	4/19/13	5.0	0.5	43.58963	123.83798	31	W-GC
6RN	4/19/13	5.0	0.3	43.59251	123.83958	31	W-GC
5RN	4/19/13	5.0	0.4	43.59169	123.84092	32	W-GC

2.3 Sediment analysis

2.3.1. Non-destructive techniques

Cores were scanned by X-ray computed tomography at OSU's Veterinary Hospital within 8 days of coring, producing x-radiographs which allow visual inspection and digital measurement of core and stratigraphy and assessment of relative density with grayscale value (light and dark).

Prior to being split lengthwise, most cores were placed on a Multi-Sensor Core Logger (MSCL) track for measurements of wet bulk density by gamma-ray attenuation and loop magnetic susceptibility (MS; Geotek, 2015). All large gravity cores were also measured with a point-MS sensor on a line scan track (Zolitschka et al., 2001) at higher resolution. Dry bulk density (g cm^{-3}) was calculated by standard techniques from wet bulk density (Dadey et al., 1992; Appendix A4).

Large gravity cores and the Nesje cores were split and described according to standard techniques within weeks or months of coring. All split core faces were imaged using a high-resolution line-scan camera. Some images were captured immediately after splitting open the cores, but most were taken after the sediment at the split-core surface had already oxidized and changed color, which occurred within hours to days.

Cores were measured on two scales, referred to as "MSCL-" and "CT-depths". Thickness and calculated mass measurements were done on the CT images ("CT depths"). Non-destructive measurements on the MSCL and destructive sampling, as described below, were done in increments according to those assigned to the core on the MSCL track ("MSCL depth"). Because dewatering and slight compaction occurred between the time of CT scanning and MSCL measurements, the scales are different and require a key to translate between the two (Table A3).

2.3.2. Destructive sampling

Several destructive techniques were used on sediment from cores to measure the following parameters: grain size, elemental analysis of carbon and nitrogen, and radionuclides for age control, including ^{137}Cs and ^{14}C. For grain size and elemental analysis, bulk sediment samples were removed in 1-cm increments the entire length of core 02aN, and in some locations in cores 02bN and 02N after the cores were stratigraphically correlated. Methods for specific sampling for parameters will be described in their respective sections. Refer to Appendix A4 for more detail on each analysis.

2.3.3. Grain size analysis

A ~6 g sediment sub-sample from each 1-cm sample underwent a digestion process to remove organic material so that only the lithic fraction remained for grain size analysis (Gray et al., 2010). Grain size was then estimated on a 2000 Malvern Mastersizer with methods described in Sperazza et al. (2004). The output is grain sizes in 100 bins as a percentage of the total volume of sample.

2.3.4. Geochemistry

For elemental analysis, 10-20 mg of each 4-6 g freeze-dried and ground sediment sample were combusted at high-temperature in a Flash EA1112 Elemental Analyzer (EA) and through calibration software, provided estimates of % total carbon (TC) and % total nitrogen (TN) by weight of each sample. To characterize the %TC, %TN, and C:N of the thin dark laminae and thicker light layers at the top of the reconnaissance core (Figure A2), 8 structural samples of the two types of layers were collected and analyzed as above (n=16). In a separate analysis by the acidification of 30 representative samples throughout the core (Hedges and Stern, 1984), it was determined that > 95% of samples are free of inorganic material (Figure A5). Because of the

possibility of inorganic carbon (IC) being present, albeit small, the %TC will continue to be referred to as such, while recognizing the predominance of organic carbon.

2.3.5. Core chronology

To date the recent past, ^{137}Cs and ^{210}Pb activities in the cores were measured by γ-ray spectroscopy (e.g., Gilmore and Hemingway, 1995). Samples of sediment were taken iteratively from five of the large-diameter gravity cores in 0.5 and 1 cm increments from the sediment-water interface (SWI), freeze-dried, ground with mortar and pestle, and then stored in polystyrene jars. Two Canberra Low Energy Germanium (LEGe) detectors and Genie 2000 software were used to count and calculate the radionuclide activities, according to methods described in Wheatcroft and Sommerfield (2005). Once the stratum of the 1963 peak of atmospheric ^{137}Cs deposition and 1953 date of onset was identified, these locations were visually correlated to the smaller diameter Nesje cores, 02aN and 02bN. Counts of the radioisotopes ^{210}Pb and ^{214}Pb were consistently too low to be used to calculate sediment accumulation rates, and so were not considered further.

For the early period (i.e., pre-1880), the two long Nesje cores and a nearby gravity core provided terrestrial macrofossils for ^{14}C dating. Generally, 1-cm core slices were wet-sieved in search of material that was the least degraded and of sufficient mass (~1 mg). After physical cleaning, samples were chemically treated with an acid-alkali-acid wash (Olsson, 1986; Björck and Wohlfarth, 2001), dried, and sent to National Ocean Sciences Accelerator Mass Spectrometry (NOSAMS) for analysis by combustion, graphitization, and counts of carbon isotopes. The resulting ^{14}C dates were calibrated with Oxcal program v4.2.4 (Bronk Ramsey, 2009) with the IntCal13 atmospheric curve data set (Reimer et al., 2013). The output was likelihood probability distributions. By applying prior knowledge about non-uniform sediment deposition and possible outliers, Oxcal generated marginal posterior densities, and with those, calculated calibrated age ranges referred to as highest posterior densities (hpd; Figures A8 and A9; Appendix A6.1).

CHAPTER 3 – RESULTS

3.1 Stratigraphy of the core

X-radiographs of cores 02aN and 02bN yielded a rich sedimentary stratigraphy that is comprised of distinct layers, beds up to 23 cm thick, and sections of quasi-homogeneous fabric (Figure 3, Figure A3). Based on the CT, grain size, and high resolution geochemistry in cores 02aN and 02bN, seven stratigraphic units are identified: distinct layers, indistinct layered sections, mottled units, graded beds, coarse homogeneous layers, clay drapes, and a unique fine sand bed topped with weakly graded silt (Figure 4).

3.1.1. Distinct layers

Viewed in the x-radiographs, distinct layers alternate between lighter (more opaque), indicating denser material, and generally thinner, less dense dark layers (Figure 4a, Figure 3). It is apparent in the x-radiographs that these areas of layers are gassy, indicated by voids (small black splits and splotches) crossing both light and dark layers. Viewed in the photograph of a core (Figure A2) layers are relatively thin and distinct. The layers alternate in color between olive gray and dark brown or black, hereafter referred to light and dark layers, as this coincides with the x-radiograph images as well. The light layers are thicker on average throughout the core than the dark layers, with medians of 0.31 cm and 0.19 cm, and upper limits of 2.15 and 0.62 cm, respectively (Table 2). Where distinct layers are preserved throughout the core, their mass distributions are remarkably similar, except for a section in the upper part of the core at 26-67 cm where there are more layers with more mass (Figure 5). It is also within this section, including the layers above, i.e., the top 67 cm of the core, the upper and lower contacts of layers are quite sharp. In other areas of the core, the contacts are more gradual, such as around 630 cm and even less so around 570 cm, for example. Distinct layers comprise 16% of the mass of the sediment column of core 02aN.

Distinct layers have 2% total carbon (TC) and 0.18% total nitrogen (TN) as an overall average (Table 3). When light and dark layers are separated out, however, the dark layers are

found to be carbon- and nitrogen-rich (medians of 3.11% and 0.30%, respectively; Figure 6), and the light layers, which are thicker and bias the average of the distinctly layered intervals, are less so (medians of 2.04% and 0.16%, respectively). The C/N ratio of distinctly layered intervals is 12.92, the average median grain size (D_{50}) is 6.55 μm , and the percent clay, silt, and sand is 28.43, 69.01, and 2.55%, respectively, (Table 3) and so is described as clayey silt (following Shephard, 1954).

Figure 3. Stratigraphic correlation of Cores 02aN and 02bN. Depth is marked in centimeters from the x-radiographs. Event beds (e.g., E1) are labeled at their bases, except E21, and are stratigraphically correlated between the two cores. The cores are broken into four lengths, top to bottom is displayed left to right. Core 02aN is placed left in each correlated pair, Core 02bN is placed right. Locations of ^{14}C sample extraction are marked with the point of a bold triangle on the core(s) from which the material came. Across from each sample point are the calibrated median ages of ^{14}C-dated material used in the age-depth model, labeled with their sample name (e.g., LL2), along with their 95% highest posterior density ranges (hpd). On the top part of the core (0-182 cm), 2012 AD marks the first full water year varve near the sediment-water interface (SWI). 1950 AD is found by varve counting. 1900 and 1800 AD are approximate ages based on application of mass accumulation rates. Core 02bN ends above the bottom of event bed E21, so this event is stratigraphically correlated at the top of the event bed.

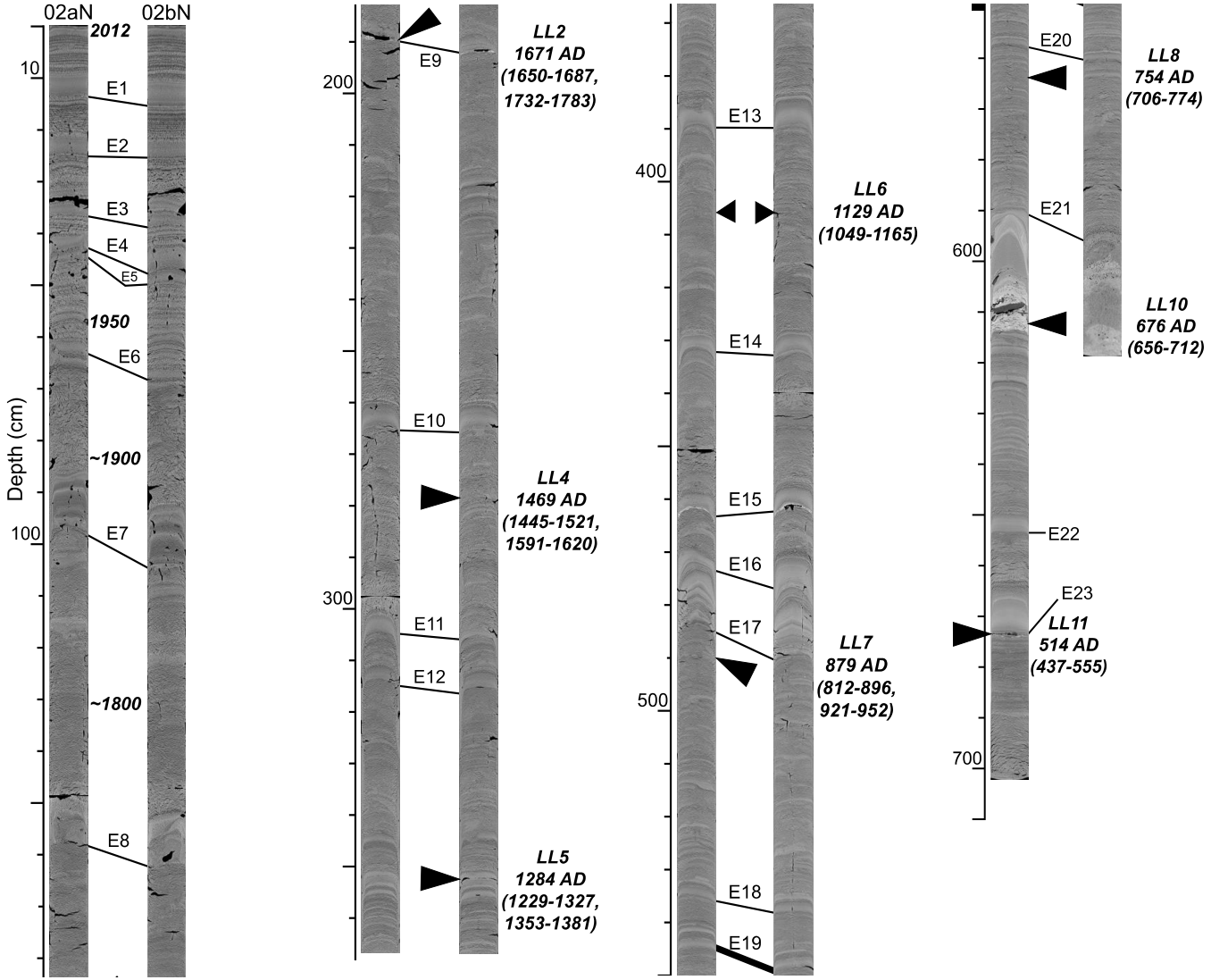
02aN
02bN
2012
10
E1
E2
E3
E4
E5
1950
E6
~1900
E7
100
~1800
E8
Depth (cm)
200
E9
LL2
1671 AD
(1650-1687,
1732-1783)
E10
LL4
1469 AD
(1445-1521,
1591-1620)
300
E11
E12
LL5
1284 AD
(1229-1327,
1353-1381)
400
E13
LL6
1129 AD
(1049-1165)
E14
E15
E16
E17
LL7
879 AD
(812-896,
921-952)
500
E18
E19
E20
LL8
754 AD
(706-774)
E21
600
LL10
676 AD
(656-712)
E22
E23
LL11
514 AD
(437-555)
700

Figure 3.

Figure 4. Seven stratigraphic units displayed by x-radiographs and parameter plots. The units in the top row (l to r) are distinct layers (DL), indistinct layered sections (IDL), and mottled sections (Mo). On the bottom row are three examples of event beds (EB): d) sand and woody debris event bed E21; e) graded bed; and f) graded bed with clay drape (CD) as gradual upper contact and homogeneous layer (Ho) at sharp basal contact. Parameters for each core piece are (l to r): %TC (total carbon), %TN (total nitrogen), C:N (atomic), and median grain size (D_{50}). Scales are different for most parameters, so most have their own ordinate axis. Scale for %TC is common vertically for a-d, b-e, c-f, respectively, and also in D_{50} for b-e and c-f. The D_{50} parameter for EB (c) fills more than half of the bottom of the figure. Core pieces are from the following CT depths in core 02aN: a) 14-33 cm; b) 367-386 cm; c) 489-508 cm; d) 588-616 cm; e) 663-675 cm; f) 457-467 cm.

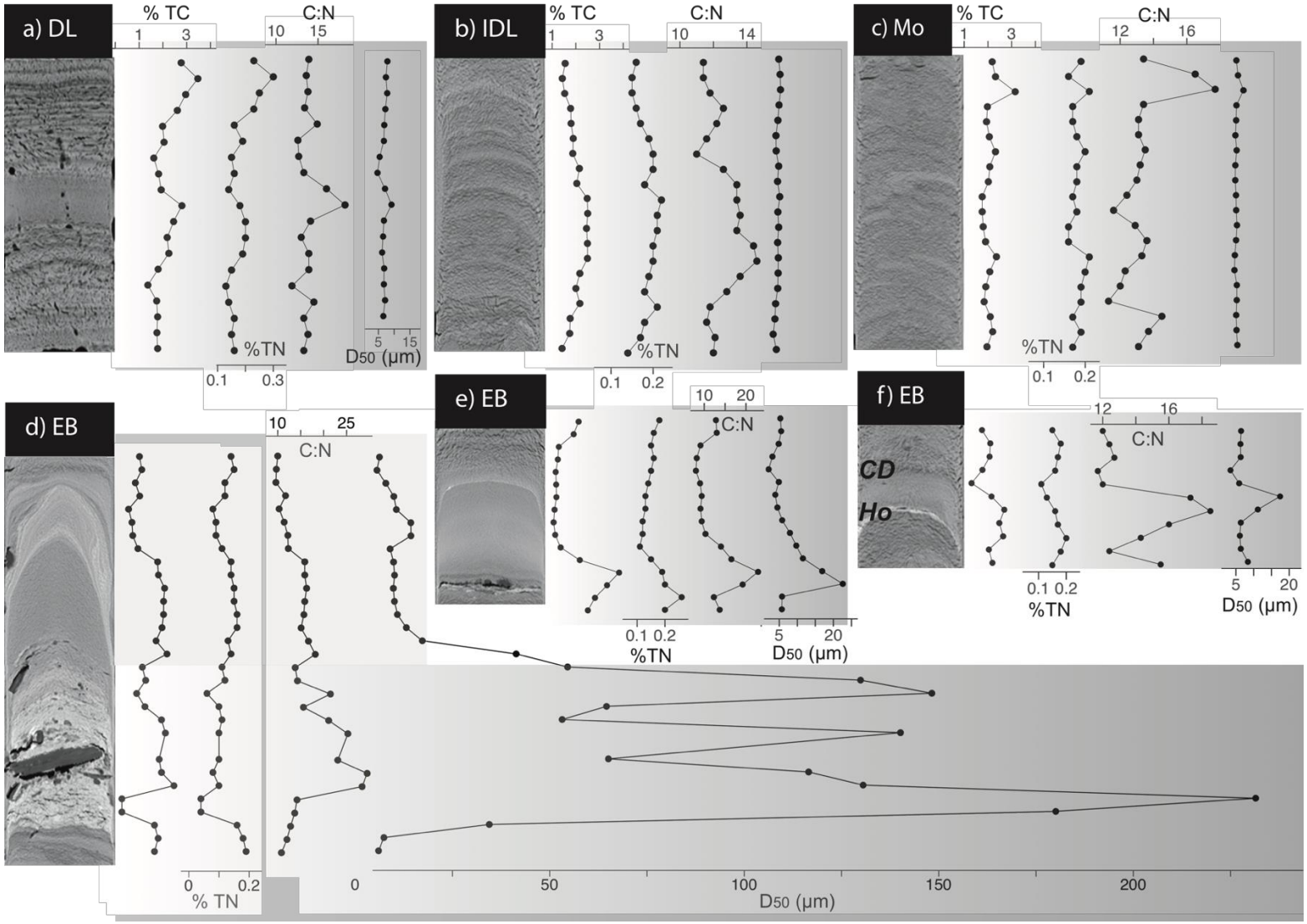
a) DL
% TC
1 3
C:N
10 15
%TN
0.1 0.3
D50 (µm)
5 15
b) IDL
% TC
1 3
C:N
10 14
%TN
0.1 0.2
c) Mo
% TC
1 3
C:N
12 16
%TN
0.1 0.2
d) EB
10 25
C:N
0 0.2
% TN
0 50 100 150 200
D50 (µm)
e) EB
10 20
C:N
0.1 0.2
%TN
5 20
D50 (µm)
f) EB
CD
Ho
12 16
C:N
0.1 0.2
%TN
5 20
D50 (µm)

Figure 4.

Table 2. Description and thickness of stratigraphic units. Descriptions are in terms of both the actual core sediment and of the x-radiograph (*Sed, CT,* respectively). Layers are broken into components to show the difference in thicknesses and parts. The sand layer is a single unique unit at the bottom of a graded layer at 6 m depth, thus only one thickness value is given. Units are combined into two associations based on origin.

Unit association	Stratigraphic unit name	Unit descriptions		Thickness (cm)		
				Mean	Median	Range
Background sedimentation	Distinct layers	*Sed:* Alternating thick olive gray and thin dark brown/black layers; *CT:* Alternating thick light (more dense) and dark (less dense) layers; gassy fabric; *Sed below 70 cm:* "light" layers are dark, as in graded beds	*Light*	0.41	0.31	0.04-2.15
			Dark	0.25	0.19	0.06-0.62
	Indistinct layered units	*Sed:* Brown homogenous mud matrix intercalated with few and faint thin dark or thick light layers; *CT:* Dark matrix with few and faint complete thicker light and thinner dark layers; gassy fabric		2.78	2.30	0.59-10.11
	Mottled units	*Sed:* Brown homogenous mud matrix with lighter-value mottles; *CT:* Dark matrix mottled with amorphous chunks of lighter (denser) sediment; gassy fabric		3.47	1.24	0.59-17.07
Event layers	Clay drape	*Sed:* Light brown layer generally with gradual contact from graded layer below to next layer above; *CT:* Darker layer atop graded layer; gassy		0.50	0.44	0.13-1.34
	Graded	*Sed:* Usually normal grading, with dark brown at base grading to light brown clay drape; *CT:* Grading upward from dark to light; variations include lighter (denser) area in middle and darker near top and/or alternating thin light and dark layers with sharp contacts at top (pulses); not gassy		4.89	3.02	1.15-23.88
	Homogeneous	*Sed:* Generally, thin dark brown layer with sharp lower contact at the base of graded beds; *CT:* Thin, bright white layer with sharp lower contact; contains much allochthonous debris; not gassy		0.47	0.47	0.12-0.90
	Sand layer	*Sed:* Dark brown layer with sharp basal contact, grading upward to clayey silt; unconsolidated; *CT:* Bright white thick layer with sharp basal contact; contains woody debris and voids		One layer; thickness = 8.89 cm		

Table 3. Stratigraphic unit summary statistics of grain size and geochemistry. Each row includes the mean (standard deviation) of six grain size parameters and three geochemical parameters, and the descriptive name for the majority and secondary clastic class of samples in the unit. The far-left column groups units into two associations based on origin. [1]Textural classification is after Shephard, 1954.

Unit association	Stratigraphic unit name	D_{10} (µm)	D_{50} (µm)	D_{90} (µm)	% clay	% silt	% sand	C:N (atomic)	% TC	% TN	Textural classification[1]
Background sedimentation	Distinct layers	2.08	6.51	22.71	28.43	69.01	2.55	12.92	2.04	0.18	Clayey silt, silt
		(0.22)	(0.81)	(11.31)	(4.17)	(4.80)	(1.69)	(1.69)	(0.48)	(0.03)	
	Indistinct layered units	2.05	6.51	22.18	28.79	68.71	2.51	13.16	2.15	0.19	Clayey silt, silt
		(0.20)	(1.00)	(4.14)	(4.01)	(4.44)	(1.47)	(1.40)	(0.42)	(0.03)	
	Mottled units	2.12	6.83	23.20	27.38	70.04	2.58	13.28	2.15	0.19	Clayey silt, silt
		(0.18)	(1.70)	(7.82)	(3.38)	(3.35)	(2.41)	(1.37)	(0.47)	(0.03)	
Event layers	Clay drape	1.49	4.49	15.85	44.16	54.68	1.16	11.74	1.59	0.16	Clayey silt, silty clay
		(0.60)	(1.16)	(4.09)	(11.13)	(10.85)	(1.36)	(1.53)	(0.31)	(0.02)	
	Graded	3.10	13.56	41.40	18.57	74.90	6.52	16.22	2.16	0.15	Silt grading to clayey silt, or to silty clay, at times with sandy silt base
		(0.95)	(9.83)	(29.95)	(9.66)	(9.52)	(9.00)	(4.92)	(1.15)	(0.03)	
	Homogeneous	3.01	13.86	71.76	15.87	70.78	13.60	17.04	2.36	0.16	Clayey silt, sandy silt
		(0.83)	(5.37)	(25.84)	(4.18)	(4.39)	(6.40)	(4.09)	(1.00)	(0.04)	
	Sand layer	7.86	125.98	454.59	6.84	28.70	64.46	20.67	1.55	0.08	Silty sand, sand
		(4.78)	(55.42)	(85.15)	(2.90)	(8.28)	(11.06)	(5.99)	(0.70)	(0.03)	

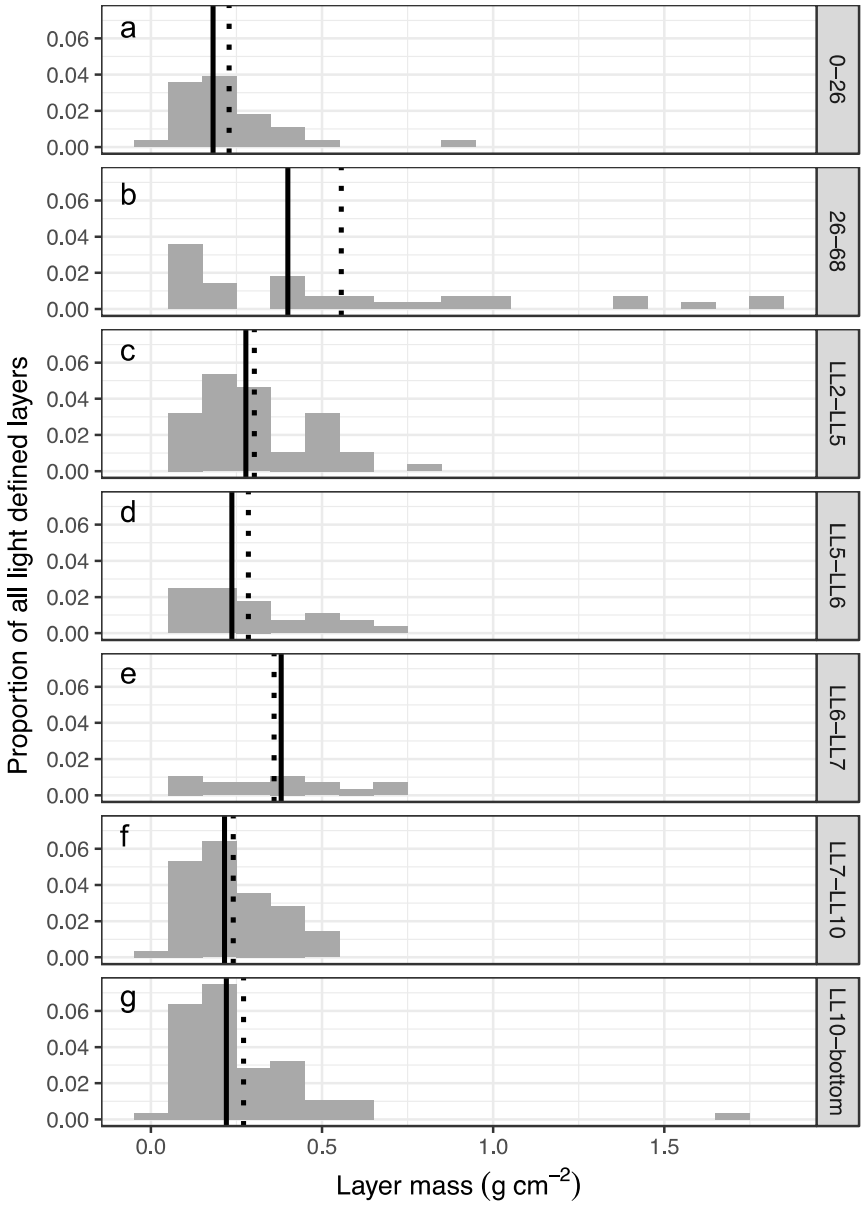

Figure 5. Distributions of light layer mass through the sedimentary column. These are represented by proportional histograms for sections through the core. Sections are delineated by location in the core which captures groups of layers, and are conveniently bounded by the ^{14}C sample intervals. The sections of the core which have the highest concentrations of distinct layers are 0-26 cm, 26-67 cm, LL5-LL6, LL7-LL10, and LL10-end. See Figure 3 for the locations on the CT scans of these intervals. The whole core is represented, except 68-190 cm (LL2) where there are only 2 preserved distinct layers. The vertical solid black line is the median of each distribution, and the dotted black line is the mean.

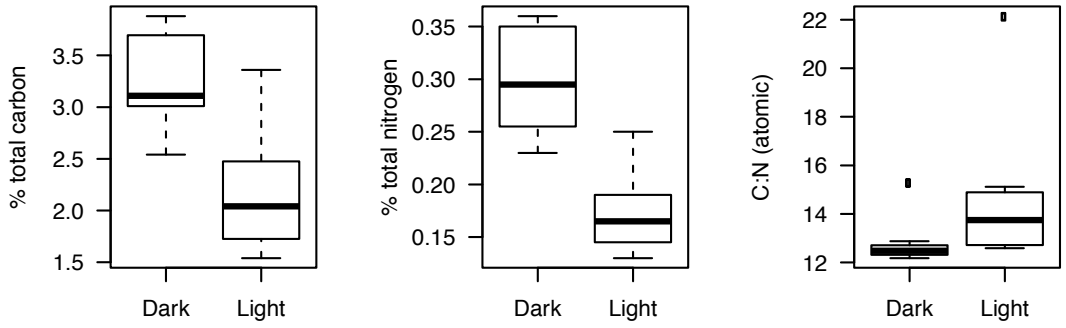

Figure 6. Structural sampling of dark and light defined layers. Geochemistry results of structural sampling are represented by boxplots of % total carbon, % total nitrogen and C/N. Dark and light layers were sampled in the top 10 cm of Core 5RN.

3.1.2. Indistinct layered and mottled units

These beds have similar characteristics in both grain size and geochemistry to distinct layers (Table 3). Their average median grain size is 6.51 μm and 6.83 μm respectively. Layers and layers exist in the indistinct layered sections, but are ephemeral and difficult to quantify in their extent and thickness (Figure 4b). In mottled sections, clasts and specks similar in value to light layers in the x-radiograph can be seen "floating" in a homogeneous matrix, and appear to be broken pieces of layers (Figure 4c). As in distinctly layered regions, the indistinct layered and mottled areas are gassy as indicated by pervasive voids in the x-radiograph. Contrasting to distinct layers, indistinct layered and mottled sections are much thicker, up to 10.1 cm and 17.1 cm, respectively. Distributed within and between the distinctly layered sections, they dominate the core, occupying 68% of its mass. Because these beds have similar variations and summary statistics as shown in boxplots of the grain size and geochemical parameters (Figure 7, Table 3), it can be concluded that the indistinct layered and mottled sections are previously deposited distinct layers in various stages of alteration due to some degree of post-depositional re-working. Therefore, these three units are combined into one association. As will be discussed in Section 4.1.1, the distinct layers, and thus the indistinct layered and mottled units, are deposited in relatively quiescent periods, so are referred to as “background sedimentation”.

3.1.3. Graded beds, clay drapes, and homogenous layers

Throughout the core, there are features that punctuate the background stratigraphy, and are interpreted to be event deposits. These are correlated, numbered, and labeled (e.g., E1) from the top to the bottom of cores 02aN and 02bN in Figure 3. Event beds are also correlated through the other cores throughout the lake (Figure A3). Twenty-three graded beds with clay drapes of at least 34% clay were identified throughout the core, ranging in thickness from 1.15 cm to 23.88 cm (Table 4). Although most event beds contain two or three subunits: a basal homogeneous layer (Figure 4f), a graded bed (Figure 4d-f and part of Figure 4a), and a clay drape (Figure 4f), the deposits manifest themselves in different ways. Their internal structure indicates a much more rapid deposition than the surrounding background sedimentation. Several beds have a thin, coarse layer, bright in the x-radiograph, with a sharp basal contact with the background stratigraphy (e.g., Figure 4f). This layer often contains allochthonous material such as relatively coarse (~1 mm) fragments of leaves, twigs, and charred and non-charred wood fragments. Even if this homogeneous layer is not present, nearly all of the event beds have a sharp basal contact.

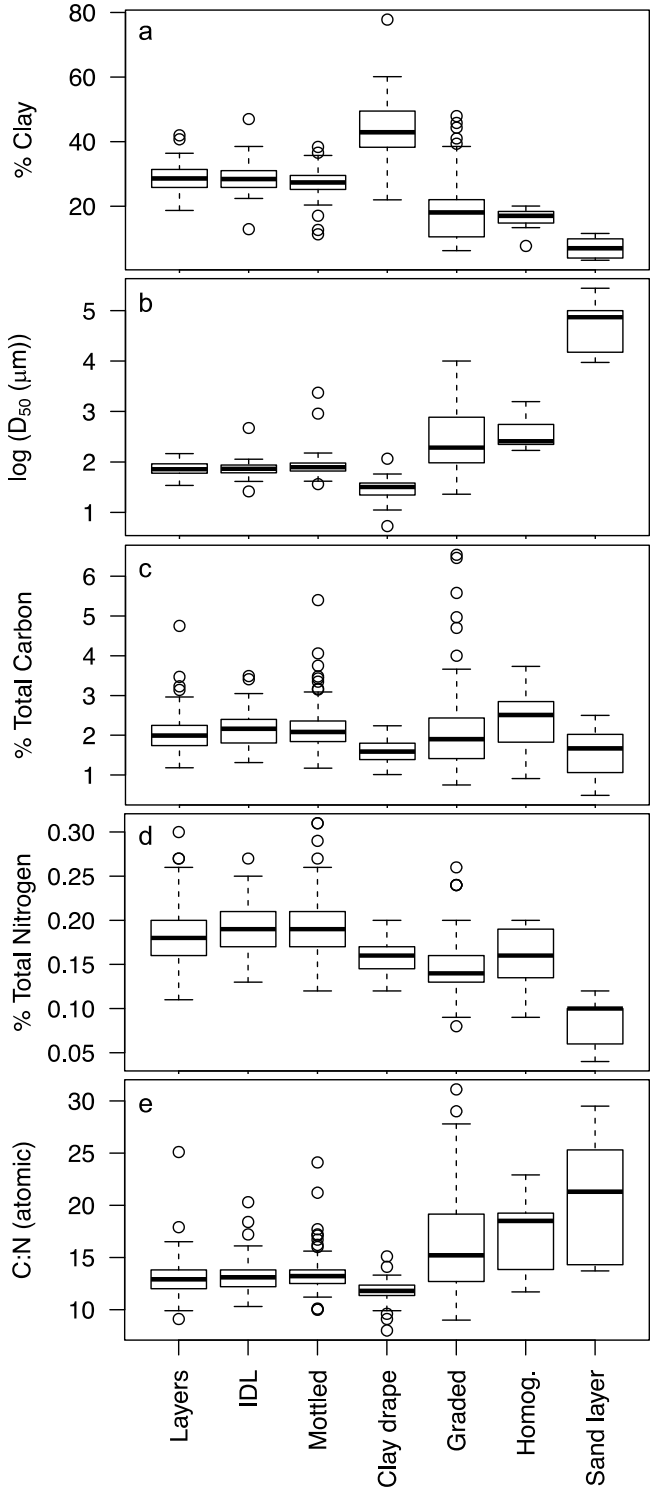

Figure 7. Variation of grain size and geochemical parameters. Boxplots display variation, median, and outliers of grain size and geochemical parameters by the 7 major depositional units in the core: distinct layers, indistinct layered sections (IDL), mottled units, clay drape, graded beds, homogeneous layers, and the sand-woody debris bed (E21). Parameters shown are % clay by volume, log of median grain size (D_{50}), weight % total carbon and nitrogen, and carbon to nitrogen atomic ratio. D_{50} is shown in log scale for viewing clarity.

Table 4. List of 23 event beds. These were defined by a minimum % of clay in the drape over the preserved graded bed. These beds were removed to calculate a background sedimentation rate. Estimated year is rounded to nearest 10 years, and is derived by varve counting for event beds 1-6, and an estimation by applying the resulting background sedimentation rate of 0.38 g cm^{-2} y^{-1} for event beds 9-23, and a background sedimentation rate of 0.54 g cm^{-2} y^{-1} for the "gap" period in between (event beds 7 and 8). Event bed depth measured according to the Multi-Sensor Core Logger (MSCL) is the scale for sampling and parameter measurements. Thickness and calculated mass measurements are derived from the x-radiographs ("depth CT").

Event bed number	Estimated water year (AD)	Event depth MSCL (cm)	Event depth CT (cm)	% clay cap	Layer thickness (cm)	Dry mass (g cm^{-2})
1	1997	11	14.0	46.7	4.7	5.1
2	1982	22	24.8	37.6	3.9	4.2
3	1971	33	36.8	43.1	2.3	2.3
4	1965	39	43.4	35.3	2.3	2.8
5	1964	41	45.5	50.8	1.7	1.4
6	1946	59	63.3	39.8	2.0	2.3
7	1890	91	96.8	34.4	9.6	7.7
8	1770	152	157.8	37.5	10.9	10.6
9	1690	185	190.0	44.1	3.4	3.1
10	1470	259	265.7	56.0	4.8	5.5
11	1370	298	304.7	42.7	3.7	4.3
12	1350	308	313.9	41.5	2.2	2.3
13	1150	383	389.4	38.9	3.0	3.8
14	1030	425	431.6	41.2	2.7	3.0
15	940	456	462.3	53.7	2.7	2.2
16	920	466	472.8	44.8	2.9	2.2
17	920	478	484.5	48.2	10.2	9.2
18	760	528	534.9	43.2	1.2	0.9
19	740	538	544.6	60.1	1.6	1.2
20	710	552	557.2	39.7	1.5	1.1
21	630	610	613.7	22.0	23.9	30.3
22	550	646	653.4	53.0	3.2	2.8
23	510	667	673.5	77.8	8.1	9.8

The main body of these beds is a graded bed, which in the x-radiograph shows as a gradation in density, most often from darker to lighter to darker (e.g., Figure 4e). This gradation is reflected in the grain size, the magnetic susceptibility (MS), and the geochemical data. In the grain size data, above the base there is usually thin inverse grading, and then thicker normal grading, first briefly coarsening from clayey silt to silt or sandy silt and then fining upward to the clayey silt or silty clay drape (Figure 4e-f; Table 3; Figure A4).

In the MS data displayed in core 1N, which is stratigraphically correlated with the tops of cores 02aN and 02bN, there is a gradual increase and then a gradual decrease in MS through the event beds, with a peak often coinciding with the lightest x-radiograph value and near the peak of grain size coarseness (Figure 8). In the geochemical data, most graded beds show a spike in %TC at the beginning of the event and a gradual drop to much lower values for the rest of the bed (e.g., Figure 4e; Figure A4).

Although the 23 event beds are remarkably similar in their grading sequence, their thicknesses vary and there are a few beds with stark differences. For example, two beds, E7 and E8, have massive, fine sand-rich beds below or above a graded bed. Additionally, E7 was captured in MS profile of core 1N at about 100 cm depth (Figure 8), and shows the lowest excursions in the entire core around this event bed. This bed also has the largest sustained %TC anomaly of the entire 02aN core (Figure A4). Six graded beds have thin faint layers near the top but within the bed. These laminae are of contrasting brightness in the x-radiograph and have sharp contacts above and below (e.g., graded bed in Figure 4a). Lastly, the thickest event bed of the core, E21 (Figure 4d), has a thick fine sandy base 8.89 cm, thick and opaque in the x-radiograph, with a sharp, possibly erosional contact with the background sediment below. Although this sandy base is analyzed as a separate unit - “sand layer” - because of unique characteristics (Tables 3 and 4; Figures 3 and 4d) such as coarse woody debris and a large void, it is integrally part of event bed E21, as it transitions to a weakly graded silt layer, for a total thickness of 23 cm.

Despite the variations within the graded beds, their grain size distributions, geochemical characteristics, and MS profiles are differentiated from the background sedimentation (Tables 3 and 4, Figure 7). When viewed over the entire core, the measured characteristics for background sedimentation are relatively constant over time but are more variable for the event beds, which are clearly outside the range of the background sedimentation (Figure 9).

The distinguishing characteristics of event beds are that % clay is lower (18% compared to 27% and 28%), the mean D_{50} is an order of magnitude higher, the %TN is lower (0.15), and C:N reaches 18 on the 75th percentile of the boxplot (Figure 7), compared to 13 for the background sediment. As expected, for all parameters, the interquartile range (IQR) is much wider for graded beds (Figures 7 and 9) than for other stratigraphic units. Homogeneous layers are similar in most of their characteristics with graded beds, but are so thin that their measurements of parameters included sediment from both the background sediment and graded bed above. Clay drapes atop the bed range in thickness from 0.13 cm to 1.34 cm. They have the highest mean clay content (44%) of all stratigraphic units, the lowest mean D_{50} (4.5 μm), and the lowest mean C/N (11.74).

These three units form an association referred to as “event beds” because they represent an anomaly in the background sedimentation, and higher-energy delivery. Together this association constitutes 16% of the mass of the core. There are several layers in the core that did not meet the criteria of having a clay drape. Some are graded, and some may be graded but the resolution of sampling could not detect this. For consistency throughout the analysis, these layers were not included in the graded beds and event layer association. As with the 23 event beds previously identified, these are distributed fairly uniformly throughout the core, except for the upper 67 cm of the core, where event beds and thicker light layers are more frequent.

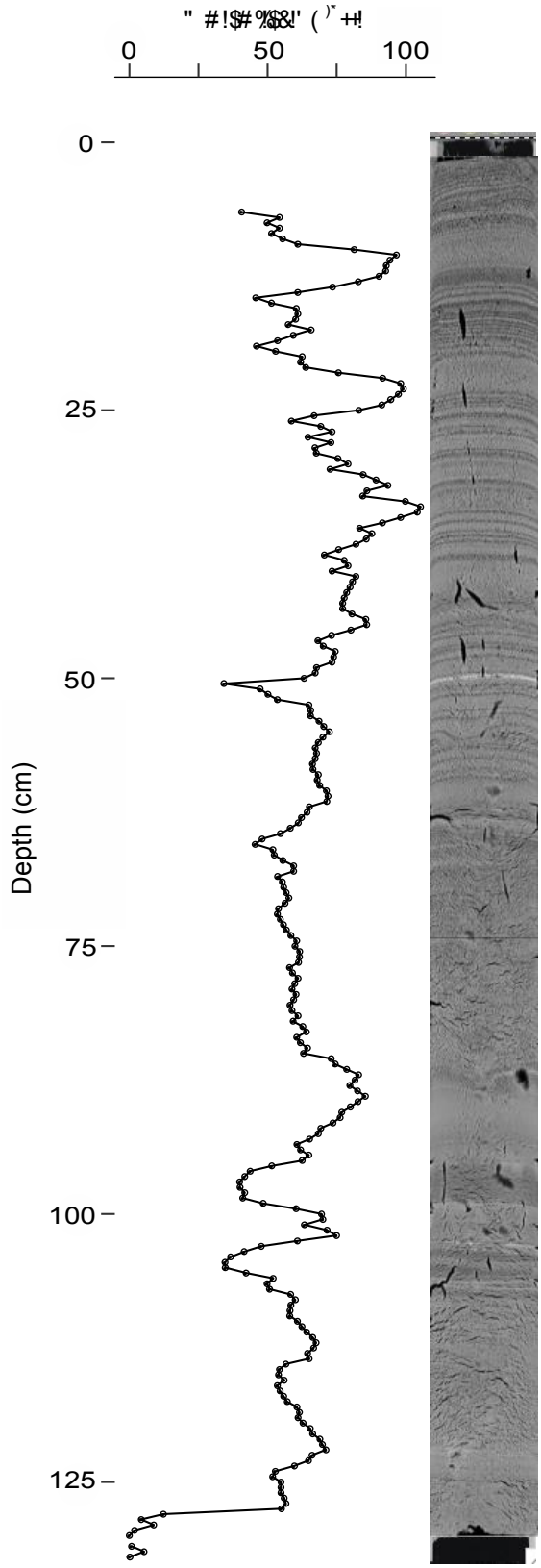

Figure 8. Magnetic susceptibility profile of Core 1N.

Figure 9. Select parameters of event beds and background sediment. Parameters included are % clay, D_{50}, %TC, %TN, C:N. Each pair consists of an event bed boxplot on the right (red) and a boxplot for the succeeding background sedimentation (yellow) on the left, up to the next event. All twenty-three event beds in the core are represented, although E4 and E5 are adjacent in the core, so were combined in this figure. Distributions consist only of values from samples whose sediment comprised approximately 100% of the two associations (events and background sedimentation). Because of small sample sizes, in three cases no values were available to report within regions/event beds 17-19, and in several cases for event beds, only one sample result was available to report (event beds 3, 6, 12, and 20), which shows as a flat bar in the figure. The bottom of event bed distribution E21 is cut off for visual clarity; it has 0.5% TC. E1-6 (blue font) represent industrial timber harvest era. E7 and 8 (red font) are during time of known wildfire.

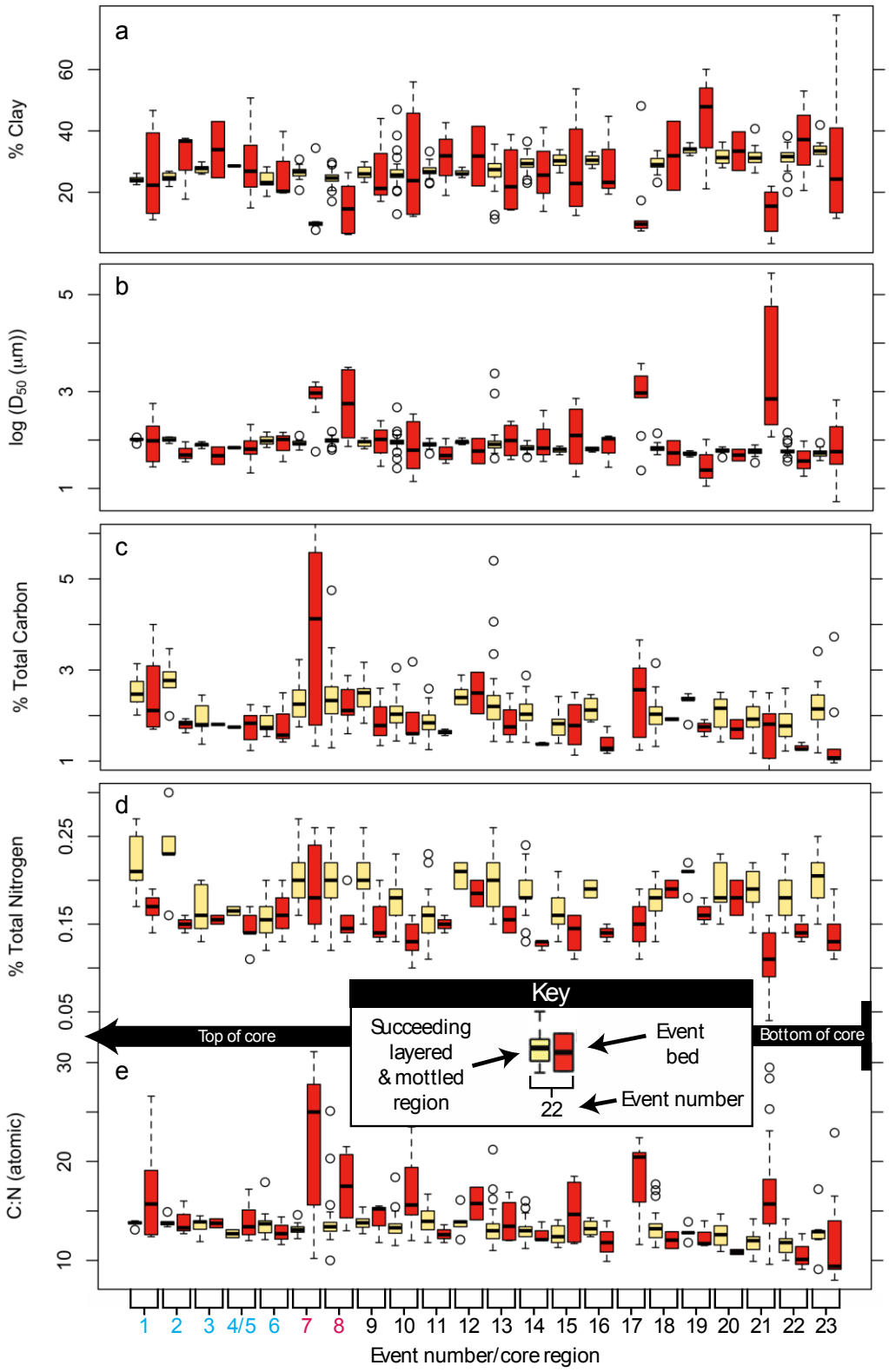
a
% Clay
20
40
60
b
log (D50 (μm))
1
3
5
c
% Total Carbon
1
3
5
d
% Total Nitrogen
0.05
0.15
0.25
e
C:N (atomic)
10
20
30
Key
Succeeding layered & mottled region
Event bed
22
Event number
Top of core
Bottom of core
1 2 3 4/5 6 7 8 9 10 11 12 13 14 15 16 17 18 19 20 21 22 23
Event number/core region

Figure 9.

3.2 Core chronology and mass accumulation rates

3.2.1. Contemporary period

The upper portion of the stratigraphic column was dated by two methods, radiometric dating of the ^{137}Cs deposition and layer counting. Once the stratum of the 1963 AD ^{137}Cs peak had been identified (Figure 10d-f), it became evident that the light-dark couplets present in the top 67 cm of the core were annually deposited, and are therefore varves (Dean and Bradbury, 1993; Edmondson, 1991). In four of five cores in which radionuclides were measured, the peak ^{137}Cs stratum was the same. The one exception was two varves different. The very top part of the two long Nesje cores and a few of the gravity cores show consistency in their layer sequencing, so it appears that the sediment-water interface (SWI) at 2013 was preserved. With the guidance of the lesser-disturbed sediment in the large gravity cores (e.g. core 1N), layers were counted upward from the 1963 stratum to the SWI at 2013 light layer. The two very thick event beds near the top are coincident with two large regional floods, WY 1982 and 1997, and additionally, another thick layer follows two layers above the 1963 layer, which is coincident with a large regional flood during WY 1965, as shown at the nearby gaging station on the Umpqua River at Elkton (Figure 1; Figure A7). Similarly, layers were counted downward in the core from 1963 until 1939, at which point the sediment becomes mottled. This boundary at 1939 divides the contemporary period from the “gap” period and early period of the core (For “gap” definition, see Section 3.2.3).

Once the varves had been identified to year, a mass accumulation rate (MAR) for the top 65.6 cm (51.4 g cm^{-2}) of the core was calculated (Table 5). A simple ratio of sediment mass accumulated by time for 1939 to 2012 is 0.69 g cm^{-2} y^{-1}. Observing the cumulative dry mass by time, a breakpoint appears to split the contemporary period into two divergent parts in terms of sediment accumulation. Based the largest p-value on a test of slope difference, the break is located between 1978 and 1979 AD (Figure 11). The MAR for before and after 1979 is 0.79 and 0.58 g cm^{-2} y^{-1}, respectively. This can be expressed as a linear sediment accumulation rate of 1.00 and 0.75 cm y^{-1}, and an overall linear rate of 0.89 cm y^{-1}, but does not account for dewatering.

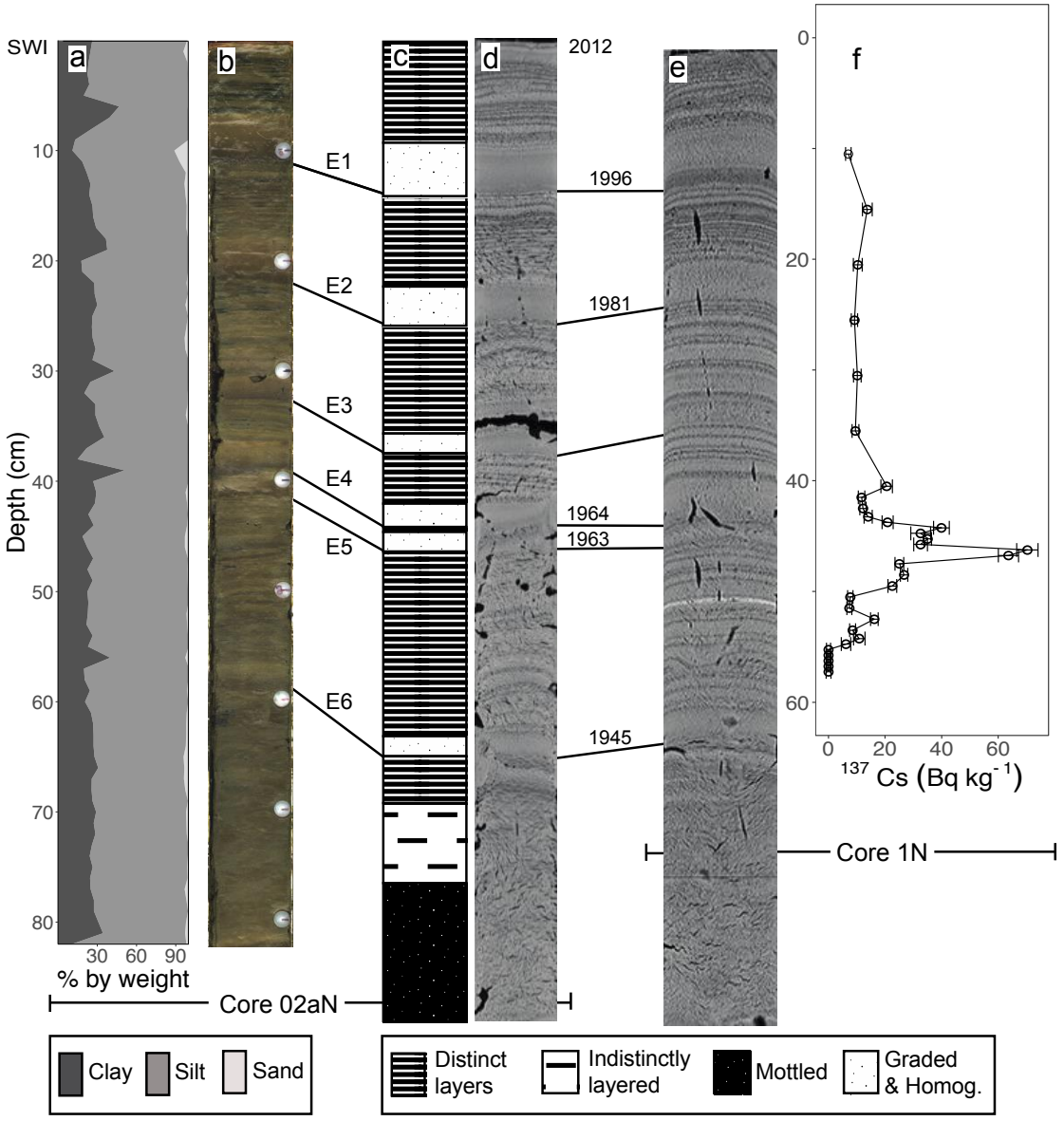

Figure 10. ^{137}Cs profile of Core 1N and stratigraphic units of Core 02aN. Upper 82 cm of Core 02aN (a-d) and stratigraphic equivalent of Core 1N (e-f), showing: a) vertical stacked area plot of % clay, silt, and sand, respectively, measured at 1-cm increments (see legend below plot); b) color photo; c) cartoon representation of the five stratigraphic units (see legend below plot); and d) x-radiograph of the center slice of the core. The stacked area plot is stratigraphically paired with the photograph and the cartoon is stratigraphically paired with the CT scan, demonstrating the disparity in length between the two pairs. This can be explained by the dewatering and consolidation of the sediment that occurred between the time of coring and immediate CT scanning, and delayed splitting, photographing, and destructive measurements of this core. Core 1N is shown on the right by e) x-radiograph and f) ^{137}Cs profile of this core. Event beds 1-6 are labeled and their stratigraphic position on both cores are indicated by lines at the base of the bed. The ^{137}Cs 1963 AD peak can be traced across the cores immediately below E5. SWI = sediment water interface.

Table 5. Mass and sediment (linear) accumulation rates. Rates for the contemporary period are calculated as simple ratios of depth to time for mass accumulation and for sediment (linear) accumulation. Rates for ^{14}C period are mean estimated slopes calculated by regression after resampling of highest probability densities of eight dated samples, LL2-LL11. Confidence intervals of the Monte Carlo (MC) type sampling are 5th and 95th quantiles of the distribution. "EFD" is event-free depth, where events have been removed and a mean estimated background accumulation rate is calculated. "All depths" have all layers present in the calculation.

Time period	Mass accumulation rate (g cm^{-2} y^{-1})		Sediment accumulation rate (cm y^{-1})	
	All depths	**EFD**	**All depths**	**EFD**
2012-1979	0.58	0.31	0.75	0.47
1978-1939	0.79	0.57	1.00	0.75
2012-1939 overall	0.69	0.45	0.89	0.63
LL2-LL11	0.44	0.38	0.40	0.35
CI for MC	(0.41-0.46)	(0.34-0.40)	(0.38-0.42)	(0.34-0.36)

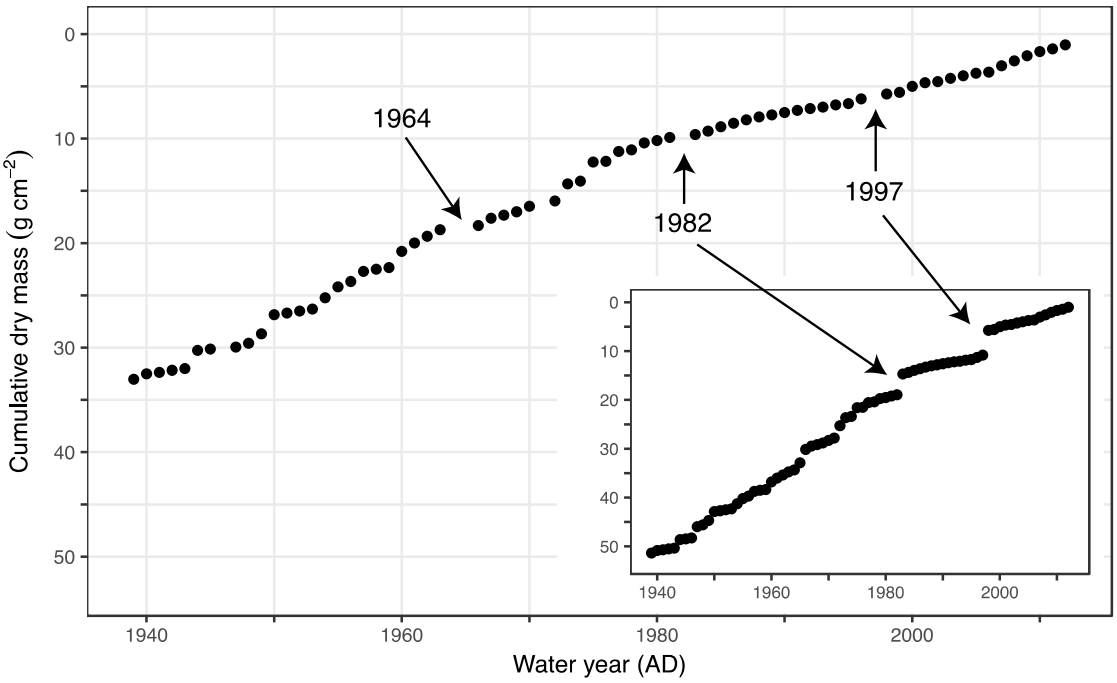

Figure 11. Age-mass model of the contemporary period of Core 02aN. Depth is represented on the y-axis by cumulative dry mass down the core with event beds E1-6 removed (EFD). Within the inset graph, the y-axis is also cumulative dry mass, but with all depths represented. The three most massive beds in the contemporary period are labeled by the years in which they occurred, and with an arrow pointing to the missing value, or in the case of the inset graph, to the two occurrences of relatively instantaneously deposited sediment, represented by a gap. For both EFD, and all-depths (inset), the difference in estimated mean mass accumulation rates between the periods 1939-1978 and 1979-2012 is significant, with a difference (confidence interval) of 0.28 (0.12-0.44) g cm^{-2} y^{-1} and 0.24 (0.07-0.42) g cm^{-2} y^{-1}, respectively. See Section 4.2 for test description and Table A2 for results.

3.2.2. Early period

Terrestrial macrofossils throughout the core provided eleven dates (Table 6). Eight were used, and three were identified as outliers and were not used in further analysis. ^{14}C ages of all samples were calculated in Oxcal and resulted in the unmodeled likelihood probability distributions expressed in 2∂ ranges. Analyzing the distributions with a deposition model and an upper boundary constraint at 1939 AD ± 2 y in Oxcal resulted in modeled posterior densities (Table 6) and an initial age-depth model (Figure A8).

To construct an age model that allows interpretation of age with mass unbiased by thick event beds, the twenty-three graded layers were removed (e.g. Brown et al., 2002; Page et al., 2010; Lauterbach et al., 2012; Howarth et al., 2013; Gomez et al., 2015). Two criteria were required for event bed removal: 1) by being macroscopically visible in the x-radiograph as a graded layer, and 2) having a minimum clay % in the clay drape over the top of the graded bed (Table 4; Appendix A6). By removing these event layers, an event-bed-free stratigraphic column with accumulating mass with depth – "event-free depth" or "EFD" (Bronk Ramsey et al., 2012), that reflects the normal background sediment accumulation rate was established. Several layers that could have potentially been rapidly deposited were not removed from the core because they were either not measureable, they did not differ from the normal winter deposition in the contemporary period, or they did not have a sufficient % clay to meet clay drape criteria. These layers were distributed fairly uniformly throughout the core. Therefore, there will be a consistent error where background MAR is slightly biased high.

Sediment and mass accumulation rate were calculated for the early period with the marginal posterior densities (probability distributions). Using a Monte Carlo (MC) approach, by resampling with replacement (n=5000) from these probability distributions, a representative sample of rates was developed (Figure A13). Summary statistics on the sampling distribution could then describe an estimated sediment and mass accumulation rate. The marginal posterior densities were used for this purpose instead of median or other single central value because the single point does not accurately represent the range of years in which the calibrated year could

actually be (Telford et al., 2004) and the densities are generally not normal and are instead multimodal (e.g., ^{14}C sample LL2; Figure A9, A11). Specifically, a single age within each of the eight marginal posterior densities was drawn, weighted by its probability of ages within the distribution. With the draws from the 8 ages and their associated depths, a least squares regression line was constructed, and from this a single estimated mean mass and sediment (linear) accumulation rate (MAR, SAR) was calculated. Resampling in this manner continued until 5000 stratigraphically-correct draws were obtained and the resulting estimated rates were accrued (Appendix A6).

The output of the MC type of resampling is an estimated mean and median SAR/MAR based on the distribution, and a percentile-based 95% confidence interval (CI) with the 2.5% and 97.5% quantiles of the distribution. The mean estimated MAR (CI) for the entire ^{14}C period was and 0.44 (0.41-0.46) g cm^{-2} y^{-1} with all events in place and 0.38 (0.34-0.40) g cm^{-2} y^{-1} for EFD. This can be expressed as a mean estimated linear SAR as 0.40 (0.38-0.42) cm y^{-1} with all events in place, and 0.35 (0.34-0.36) cm y^{-1} for EFD (Table 5), which does not account for sedimentary column compaction.

A final age-mass model for the ^{14}C period was constructed (Figure 12, Figure A10) assuming an estimated mean EFD SAR of 0.38 g cm^{-2} y^{-1}. When events are replaced as shown, the overall estimated mean MAR is 0.44 g cm^{-2} y^{-1}.

Table 6. Samples submitted for radiocarbon dates. Bolded sample names are those samples used in age-depth model. Date ranges are the 95.4% (2∂) likelihood probability distribution ranges (unmodeled) and highest posterior density ranges (*hpd;* modeled). Depth is in MSCL scale. NSF Cooperative Agreement number, OCE-0753487.

Sample name	Accession #	^{14}C Age (BP)	Source core	Depth correlated in 02aN (cm)	Material	Unmodeled calibrated date range (2∂ BC/AD)	Modeled calibrated date range (2∂ cal. AD)	Median calibrated date (cal. AD)
LL1	OS-113277	270 +/- 20	02N	152-153	Coniferous/deciduous leaf	1522-1572, 1630-1666, 1784-1795	--	--
LL2	OS-113278	190 +/- 20	02aN	183-184	Coniferous/deciduous leaf; twig	1661-1684, 1735-1806, 1931-1951	1651-1688, 1733-1784	1671
LL3	OS-113279	430 +/- 20	02aN, 02bN	227-229	Coniferous/deciduous leaf	1430-1479	--	--
LL4	OS-113280	385 +/- 20	02bN	271	Deciduous leaf	1445-1521,1591-1620	1445-1515	1469
LL5	OS-113392	685 +/- 50	02bN	346	Broadleaf (or deciduous) leaf	1252-1400	1229-1327, 1353-1381	1284
LL6	OS-113281	915 +/- 20	02aN, 02bN	398-401	Coniferous/deciduous leaf; cone bract	1036-1165	1049-1165	1129
LL7	OS-113282	1190 +/- 20	02aN	484	Coniferous/deciduous leaf	773-888	812-896, 921-952	879
LL8	OS-113283	1280 +/- 20	02aN	558	Deciduous leaf	672-770	706-774	754
LL9	OS-113284	2830 +/- 25	02aN	599	Coniferous/deciduous leaf; some charred	1051-914 BC	--	--
LL10	OS-113285	1290 +/- 25	02aN	607	Twig; coniferous leaf	665-770	656-712	676
LL11	OS-113286	1560 +/- 20	02aN	666-667	Coniferous/deciduous leaf	426-549	437-555	514
LL12	OS-113287	11800 +/- 45	--	--	C5 standard (dead wood)	--	--	--

3.2.3. Gap period

Between the early ^{14}C-dated period and the contemporary ^{137}Cs-dated period, there is no direct dating. To estimate the mean mass accumulation rates in this interval, summary statistics were calculated from a distribution as was done for the ^{14}C-calibrated dates. Monte Carlo type method resampled 5000 between the marginal posterior density of the LL2 sample (1651-1688,1733-1784 AD) and 1937-41 AD (1939 ± 2 y, an error rate for varve counting). The result is an estimated mean MAR for the gap of 0.62 (0.53-0.96) g cm^{-2} y^{-1} (Table 5).

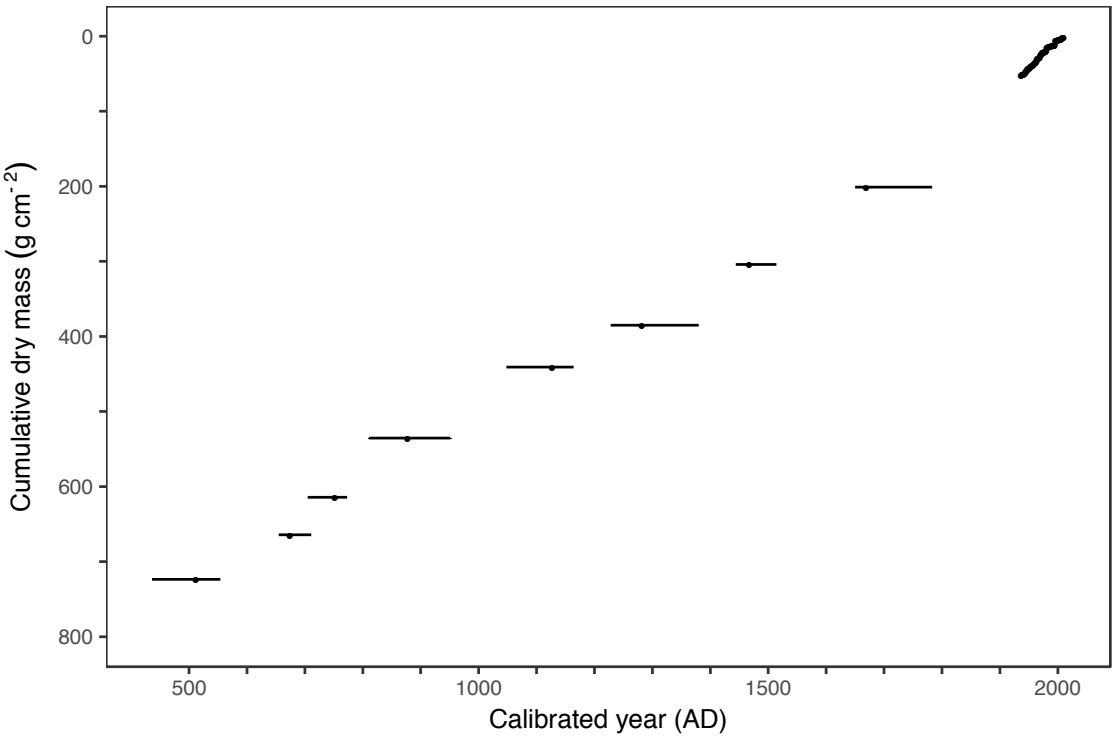

Figure 12. Age-mass model of Core 02aN. Depth is represented on the y-axis by cumulative dry mass down the core. Calibrated ages for eight radiocarbon samples are shown in green, with the median indicated by a point, and approximate 95% highest posterior density (hpd) ranges as error bars. The contemporary period is shown in the upper right corner.

CHAPTER 4 – DISCUSSION

4.1 Origin and preservation of the units

4.1.1. Distinct layers, and indistinct layered and mottled units

The geochemical signature of the distinctly layered sample intervals, %TN (0.18, mean) and low C/N (12.92, mean), are indicative of both in-lake processes and allochthonous inputs (Meyers and Lallier-Verges, 1999). When couplets of the varves in the contemporary period are examined separately, however, the specific origin of the layers becomes clearer. Dark layers have higher %TN and %TC and lower C/N ratios than light layers, strongly indicating algal productivity. Elsewhere, examination of dark layers in couplets at Lake Washington indicates diatom accumulation, which occurs during the spring and summer (Edmondson, 1991). The lighter and generally thicker layers have lower %TN and %TC, and slightly higher C/N, suggesting increased allochthonous input. Fluvial inputs of sediment are minimal during the summer in the OCR, and normal winter precipitation brings increased allochthonous materials to the lake by more voluminous and energetic fluvial inputs. These turbulent flows support coarser grain sizes. Although grain size was not measured on the light and dark layers separately, the light layers in the x-radiograph indicate denser, minerogenic material. Therefore, the couplet formation in the contemporary period is summer dark layers superimposed on light winter layers of normal annual low- to moderate-discharge floods. This seasonal deposition of couplets of fine layers suggests that these layers are varves.

It is a reasonable assumption that this process of varve formation has remained essentially the same over time within the sediment column, given that the same vegetation which has existed throughout the time of the core of the lake has adapted to the natural variability in climate (Minckley and Whitlock, 2000). So, in the early period of the core, instead of each dark layer representing annual deposition, which in the contemporary period is very thin, the thicker dark layers may consist of several years of destroyed layers by bioturbation or

some other destructive mechanism, such as gas migration. It would then be considered a mottled or indistinct layered unit.

A specific mechanism for the preservation of the varves in the contemporary period is the eutrophication of the lake, starting when logs were rafted on the lake at the beginning of major timber harvest in the catchment. Other lake sediment research has noted preserved varves and layers following eutrophication (e.g. Karlin and Abella, 1992; Page et al., 1994). See the Appendix A4.5 for a specific description of this mechanism at Loon Lake.

4.1.2. Event beds

Throughout the core there are features interpreted to not be background sedimentation, but rather deposition by events. These are preserved in the sedimentary record probably because they have increased mass and thickness compared to other deposits. The preservation of event beds increases as SAR increases, as the thickness of the bed increases, and as the distance increases from the zone of bioturbation (Wheatcroft, 1990). The smooth appearance and lack of gas bubbles visible in the x-radiograph indicate that processes of bioturbation are not as extensive in the minerogenic thick event beds.

The grain size sequence within most of the contemporary period event beds consists of a thin zone of inverse then normal grading, which is interpreted to reflect waxing and waning flows associated with hyperpycnal flows resulting from fluvial input with sustained suspended sediment, i.e., floods (Mulder and Alexander, 2001; Schillereff et al, 2014). The resulting deposit is termed hyperpycnite (e.g. Hofmann and Hendrix, 2010), and its structure can vary due to flood hydrograph differences, sediment flux and distance from inlet. For example, within floods it is possible that in changing grain interaction between waxing and waning hyperpycnal flow, the event bed itself could be eroded (Mulder and Alexander, 2001). Although there is some variation in structure in the Loon Lake contemporary period event deposits, there is not a visual clue of an erosional surface within event beds, but sometimes the inverse-graded component is lacking, as is sometimes seen in flood deposits in other lakes (e.g., Brown et al., 2000; Ambers, 2001).

Hyperpycnites support suspension of larger diameter grains to the deep basin, often traveling great distances through a lake. This would account for the coarse homogeneous layer at the base of several of the event beds. Since the lake is not thermally stratified during flooding in the winter but rather is mixing, it is expected that fine particles would remain in the water column for some time. It has been observed that for days and months following floods the lake water is still turbid and the particles continue to settle out of suspension. This is the condition by which the clay drape is deposited, composed of the finest sediment.

The grain size, magnetic susceptibility, and geochemical signatures of the contemporary event beds also support an allochthonous origin with high-energy delivery, and are outside the range of background sedimentation, as suggested in the results. The contrast between background sedimentation and event beds is consistent with research investigating changes in riverine particulate organic matter in response to discharge fluctuations in the Coast Range Alsea River north of Loon Lake. The investigators showed that with higher discharge, grain size and C/N increased (Hatten et al., 2012). The range of values they present, varying between low flows with fine grain size (C/N = 10-16), and higher flows (C/N 14-25), parallel the contrast between Loon Lake background sedimentation (C/N 12-14) and graded beds (C/N 13-19) (Figures 7, A4). Further, as the event bed grain size fines upward, the %TC and C/N decreases. The clay cap atop the graded bed is below background sedimentation levels of %TC and C/N, paralleling the low %OC associated with the fine particles carried in the Alsea River at low flow. It should be cautioned that although riverine inputs to the lake are important, the comparison of riverine results to lacustrine results does not consider actual lake sediment deposition or post-depositional diagenesis in the sediment. It is expected in the lake sediment values represent a mixing of the end members of lake algae and allochthonous material, which is what is observed.

Additional geochemical evidence of the Loon Lake event beds being of an allochthonous source is the spike in %TC and especially C/N at the bottom of the bed. This is an expected result because of an increase in coarse organic matter with high %OC and C/N from the catchment being delivered and deposited. This is consistent with other lake research: the initial increase in %OC at the onset at the base of the bed in a lake in Spain (Moreno et al., 2008), and high C/N at the base of turbidites attributed to fluvial delivery in Lake Paringa, New Zealand (Howarth et al., 2012). Other lake studies also show an agreement with the geochemical and magnetic susceptibility description of event beds described here (e.g., Brown et al., 2002; Osleger et al., 2009).

Sub-aqueous landslides from the steep walls of the lake or from resuspension of lake-bottom sediments (Karlin et al., 2004; Orpin et al., 2010) are not likely the mechanism of event bed deposition at Loon Lake in the contemporary period, because the geochemistry and grain size do not support this source of sediment. The event beds on average have different characteristics than the background sedimentation (Figures 7 and A4, Tables 2 and 3), and indicate an allochthonous input. However, this does not preclude the possibility that very high allochthonous %TC and grain size are combined with in-lake sediment to produce a moderated value of these parameters.

Event bed formation in the contemporary period can be attributed to floods in the catchment fluvial system delivered to the lake as hyperpycnites, not only because of their structure as described above, but also because of the lack of other perturbations at this time, other than timber harvest and associated activities. Therefore, the event beds in the rest of the core which share the common features of hyperpycnites, we attribute their delivery to the lake by hyperpycnal flows as well. In the contemporary period, sediment supply would have been produced by timber harvest and delivered by floods as hyperpycnites; earlier in time, wildfire and earthquakes were the perturbations.

All of the event beds earlier than E7 except E14, occur within the estimated age range of a Cascadia subduction zone (CSZ) earthquake (Table 7), so it is likely that most of these beds were deposited either co- or post-seismically. In Lake Paringa, for example, deposits indicating hyperpycnal turbidity currents were recorded on top of co-seismic megaturbidites, indicating delivery by catchment landsliding and post-seismic sediment-laden fluvial discharge after direct co-seismic delivery of sediment (Howarth et al., 2012). In a survey of lakes in the Pacific Northwest, Morey et al. (2013) also found synchroneity between the offshore earthquake record and in-land lake deposits, and recognized that at least one of the lakes had more deposits than known earthquakes, and supposed that some of the deposits were delivered by floods, not directly by earthquakes. At Loon Lake, most of the deposits have the characteristics of delivery by hyperpycnal flow, not by direct co-seismic deposition,

Table 7. Event beds within age ranges of past CSZ earthquakes. Event bed in bold print is closest to the estimated quake age. The LL ^{14}C age is the median (cal y AD) followed by the median-containing 95% hpd range. [2,3]Quake ages are estimated by mean turbidite ages and mean marsh calibrated ages of coastal subsidence. Root mean square error (RMS) and standard deviations (SD) are listed for the ranges of the turbidite and land ages, respectively. With each estimated magnitude (M_w) is a symbol indicating rupture extent, where f = full rupture of CSZ and p = partial rupture of CSZ. [3]Dashes in land evidence dates and ranges indicate only one or no recorded event, or in the case of 1700 AD, other definitive evidence. Data for all but left two columns are taken from Goldfinger et al., 2012 (Appendix 01), which compile references within, unless otherwise referenced. CSZ = Cascadia subduction zone. [4]Leonard et al., 2010; [5]Nelson et al., 2004; [6]Garrison-Laney et al., 2006.

LL event beds in stratigraphic proximity of CSZ quake	LL ^{14}C age in stratigraphic proximity (cal y AD, range)	[2]Estimated mean turbidite age (AD)	2σ (RMS) range low, high	[3]Estimated mean quake age by land evidence (AD)	2 SD range low, high	Estimated magnitude of quake (M_w)
9	1671 (1650-1687)	1685	1579-1811	1700[4]	--	9.00[f]
10	1469 (1444-1514)	1469	1377-1566	1474	1252-1696	8.70[f]
10,**11**,12	*extrapolate*	1402	1289-1524	--	--	8.19[p]
13	1129 (1048-1164)	1154	1044-1271	1199	1104-1294	8.87[f]
15,16,**17**	879 (811-895)	884	774-1008	940[5]	--	8.34[p]
17,18,19,20,**21**	676 (655-711)	707	602-831	728	605-852	8.90[f]
21,22,**23**	514 (436-554)	528	404-664	510[6]	--	8.25[p]
22,**23**	514 (436-554)	397	220-567	376	274-478	8.80[f]

so would have been a result of excavation of the sediment supply within the fluvial system, regardless of the mechanism for production of sediment. In this way, earthquakes produce sediment delivered to the lake as a post-seismic contribution, but neither the exact mass accumulation rate can be distinguished from that produced by other perturbations (e.g., Howarth et al., 2012), nor can the length of time sediment is contributed by this source be defined (e.g., Hovius et al., 2011), partly because of lack of sufficient age control early in the core. One event bed, however, does have evidence for direct delivery to the lake, possibly co-seismically, event bed E21.

The thickest, most massive event deposit of core 02aN, E21, the “sand layer”, is likely either a debris flow originating coseismically on a proximal hillslope or a “matrix-supported sediment deposit” (Giguet-Covex et al., 2012), caused by a coseismic failure of a delta (Page et al., 2010), or a massive high-fluvial discharge destruction of an unstable delta. The former is more likely because of its coincidence in time, as well as Lidar images indicating an evacuated toe-of-ridge due to failure, adjacent to Loon Lake’s surface on the west side. This appears to have been a major landslide indicated by similar landscape morphology to the landscape remaining from the formation of Loon Lake, also originating on the west side of the lake (Baldwin, 1958, 1981). Within the sand debris of this event bed, terrigenous material was abundant, including coniferous leaves, and wood pieces up to 3 cm length. On top of the sand, the deposit begins to weakly grade to silt, which could be composed of re-deposited lake sediment scoured by the debris flow. Within this transition from sand, terrigenous material dated to 1051-914 BC was found (sample LL9; Table 6). Since old terrigenous material could be found in deep soils or within the delta (e.g., Ambers, 2001), either location of failure are candidates for the origin of this layer, and the failure could have possibly been initiated by a mega-thrust earthquake, estimated to have occurred between 602-831 AD (Goldfinger et al., 2012).

As possible evidence of a proximal hillslope failure for the source of E21, it is possible that submerged wood found in the lake that was dated for the first Loon Lake ^{14}C date (Fergusson and Libby, 1962) was part of the debris flow which went on to form event bed E21.

The 95% probability range of the calibrated date on the submerged wood is 395-660 AD (conventional ^{14}C age of 1460 ± 80 y). However, the wood's calibrated median date is 541 AD, and its probability range also lies squarely within the estimated range of event bed E23 (436-554 AD), which is coeval with estimated age of a CSZ earthquake (404-664 AD; Table 7).

Event beds 7 and 8 are likely the results of a deposit motivated by floods following destabilization of hillslopes following fire, in particular, a sand-rich massive layer within each, delivered by hyperconcentrated density flows (Mulder and Alexander, 2001). Like timber harvest, fire leaves the thick soil mantle susceptible to landsliding, and plays an important role in the delivery of sediment to fluvial systems in the OCR. After event bed E9, during 1765 and 1868 AD, there are two known fires of large spatial extent in the catchment. Event beds E7 and E8 are temporally near these events. The results of magnetic susceptibility in Core 1N (Figure 8) captured the earlier event, and certainly does show an increase in MS late in the bed, following extremely low values at the beginning of the event. Each of these deposits have an inversely graded sequence and a unique 4-6 cm massive fine sand-rich layer. E7 has a graded bed on top of the massive bed, which has C/N of 28, TC of 5.3%, and 6.8% sand. E8 has the massive bed above the graded bed, and it has a C/N of 19.3, TC of 2.3% and 18% sand. Extreme storms near the time of these layers (e.g., 1890, 1909, and prehistorical floods) could have interacted with the primed landscape to create the deposits of beds E7 and E8.

4.2 Mass accumulation rates

To address how mass accumulation rates have changed in response to various forcings, different time periods were compared. First, two periods within the contemporary period were compared: 1939-1978 AD when the PDO was wet and cool and when timber harvest was at its peak (early contemporary), and 1979-2012 AD when improved forest harvest practices were assumed to be practiced, harvest rates were lower, and the climate was drier (late contemporary). Second, the early and late contemporary periods were compared to both the radiocarbon-dated period (early period) of the core, and the gap, i.e., time between the early period and the contemporary period (Table 8).

To test for significance of difference in MAR between the two contemporary periods, a multiple regression separate lines model with a climate covariate was used. The covariate used was discharge (Q) from the gaging station on the Umpqua R. at Elkton (Figures 1 and A7). Although not directly gaging Q in the catchment, there is a strong correlation between Mill Cr. Q when it was gaged and the Elkton Q (Figure A6, Appendix A5). For monthly and annual peak Q, the correlation strength by a Spearman's rank test was $r_s = 0.96$ ($p < 0.001$) and ($r_s = 0.80$, $p = 0.029$), respectively. The result of the test of difference in rates between before and after 1978 showed that there is strong evidence that the estimated mean difference in MAR of 0.24 (0.07-0.42) g cm^{-2} y^{-1} is different than null hypothesis difference of 0 between the two contemporary periods ($F_{1,69}$=7.26, p=0.0088; Table A2).

For the whole contemporary period, 2012-1939, the overall estimated mean rate and CI, provided by the separate lines model of regression without a climate covariate, is 0.69 (0.59-0.82) g cm^{-2} y^{-1}. Compare this with the CI from results of resampling the marginal posterior densities of the ^{14}C-dated samples for the other two periods of interest (for which there is not instrumental data to use as a covariate): the gap (i.e., LL2 to 1939 AD), and the early period (Table 8). These estimated mean rates are 0.62 (0.53-0.96) g cm^{-2} y^{-1} and 0.44 (0.41-0.46) g cm^{-2} y^{-1}, respectively.

Comparing the CI, the overall contemporary period CI is entirely within the MAR of the gap period. The early period MAR is slower and does not overlap the CI of either period.

When the contemporary period is divided before and after 1978, however, and compared separately to the gap period and early period, the result is striking. The early contemporary period MAR of 0.79 (0.74-0.92) g cm^{-2} y^{-1} is again entirely within the range of the gap period, and is almost twice the rate of the early period. The post-1978 contemporary period MAR of 0.58 (0.48-0.70) g cm^{-2} y^{-1}, is again significantly different than the early contemporary period MAR ($F_{1,70}$ = 8.14, p=0.0057; Table A2), but cannot be said to be different than the MAR of the gap period because of overlapping CI, and is only slightly faster than the MAR of the early period. If the CI intervals of either the late contemporary period or the early period were collectively 0.02 g cm^{-2} y^{-1} wider, the rates would overlap. In other words, after 1978, the estimated mean MAR has nearly returned to rates before 1700, but cannot be said to be significantly different than the gap.

Comparison of rates between gap and other periods is problematic possibly because it is not dated directly and also because the CI is large. The first problem has been dealt with by using the Monte Carlo method of resampling from the two end point distributions, 1939 ± 2 y and the marginal posterior density of the calibrated ^{14}C sample LL2, as was done for the entire early period. The second issue is described here with a potential solution. The CI of the gap period is quite large because resampling is from the whole of the 95% hpd ranges within the LL2 sample, 1651-1688 AD and 1733-1784 AD (Figures A9 and A11). The lower range is more probable, given prior knowledge of an event that occurred at that time, the 1700 AD earthquake. The resulting MAR could be better represented by constraining the hpd ranges to the lower interval by the following reasoning. First, the median (0.57) and the mean (0.62) of the distribution are both within the lower range, but because the whole set of 95% posterior distributions are being sampled, the mean estimated rates are very high and the distribution of rates is skewed high. Second, the median date, 1671 AD, of the ^{14}C sample collected amongst the fine sand of the homogeneous layer at the base of E9 is also within the lower range of these two 95% hpd intervals, and is a realistic date for a recently-dead coniferous needle to have arrived at this

location during an event following its death. If 1673 AD is the true value of the sample, this squarely puts event bed E9 at the date of the 1700 AD earthquake, a desirous condition so that the M_w 9.00 quake can be given some tangible and visually satisfying, if not large, credit in Loon Lake's sedimentary record. If the hpd is constrained to the lower interval, and this does seem reasonable given that this has a high probability of being the true date, consider the implications for the accumulation rates. If only the lower interval of the hpd were used and not the higher interval, the mode of the distribution would have an estimated mean MAR range of 0.53-0.62 g cm^{-2} y^{-1} (Figure A11). This is the expected result, because this is closer to the simple ratio calculation between the two periods, forcing LL2 to 1700 AD, in which the MAR is 0.63 (not shown), if the background sediment accumulation rate was uniform. This is also near the mode in which the median of the entire distribution sits (0.57 g cm^{-2} y^{-1}). The period comparison result would then be that the early contemporary period is significantly different than the gap period, in that the CI of either periods do not overlap. Additionally, when this rate is applied to this portion of the core, the events E7 and E8 land near 1890 AD and 1770 AD respectively (Figure 3), after large fires, and for E7, after and near known large regional flood events (Table A1).

It would seem then that the estimated mean MAR of the early contemporary period and the gap is higher than the whole of the early period, as described above. This is true when comparing to an overall, average MAR of the whole early period. However, the CI is narrow and it cannot be ruled out that sediment accumulation rates varied in the past within shorter periods of time. To consider how periods of time in the early period varied, the same method of Monte Carlo type resampling for the whole ^{14}C -calibrated dates was used to build distributions of possible estimated mean MAR between ^{14}C-calibrated dates of groupings based on common sediment accumulation rates and similar numbers of light layers for their statistics (Table 8, Figure 12). The results show that the MAR during the early contemporary period was still higher than most MAR, except between 879-676 AD, which largely follows event bed E21. However, when event beds are removed (EFD), the estimated mean MAR and CI of 879-676 AD are nearly identical to the MAR and CI of the early contemporary period and similar to that of the gap period.

The increased MARs in the early contemporary period and the gap period can be interpreted that during periods when multiple regolith-destabilizing forcings, such as harvest-floods OR fires-floods-earthquakes-land clearance are simultaneously acting on the landscape, the threshold for mobilization and delivery of sediment is lowered. Similarly, the elevated MAR in the period following the large E21 event bed indicates that the regolith had been destabilized by the event, sediment supply was therefore high, and subsequent floods mobilized sediment to the fluvial system and the lake.

Table 8. Summary of MAR of contemporary and early period. Contemporary rates are simple ratios for the mean, and 95% confidence interval (CI) calculated by separate lines model of least squares regression without covariates. Rates for Monte Carlo (MC) type method are mean estimated slopes calculated by regression after resampling of highest probability densities of various dated samples (LL2, etc.). Rates are presented as both "All depths" (all depths included) and "EFD" (event-free depth). Period dates are derived by varve counting in the contemporary and using the median ^{14}C age (cal y AD) of the dated samples listed in the early period.

Period (cal y AD)	Dry mass accumulation rate (g cm^{-2} y^{-1})				Method
	All depths		EFD		
	mean	95% C.I.	mean	95% C.I.	
contemporary					
2012-1979	0.58	(0.48-0.70)	0.31	(0.24-0.33)	sed/time, regression
1978-1939	0.79	(0.74-0.92)	0.57	(0.38-0.74)	sed/time, regression
2012-1939	0.69	(0.59-0.82)	0.45	(0.34-0.54)	sed/time, regression
"gap"					
1939-1671	0.62	(0.53-0.96)	0.54	(0.47-0.85)	MC (1939-LL2)
early period - overall					
1671-514	0.44	(0.41-0.46)	0.38	(0.34-0.40)	MC (LL2-LL11)
early period - core regions					
1671-1284	0.46	(0.36-0.59)	0.42	(0.33-0.54)	MC (LL2-LL5)
1284-1129	0.35	(0.21-0.58)	0.33	(0.20-0.54)	MC (LL5-LL6)
1129-879	0.40	(0.28-0.64)	0.33	(0.23-0.53)	MC (LL6-LL7)
879-676	0.69	(0.46-1.07)	0.54	(0.37-0.82)	MC (LL7-LL10)
676-514	0.36	(0.24-0.51)	0.27	(0.17-0.38)	MC (LL10-LL11)

Loon Lake's MAR and SAR are much higher than most other studied lakes in Oregon, regardless of the time period considered in the stratigraphic column. Compare Loon Lake's overall contemporary and early periods' MARs of 0.69, 0.44 g cm^{-2} y^{-1} and SAR 0.89, 0.40 cm y^{-1}, respectively (rates abbreviated here from Tables 5 and 8 for ease of comparison), to others measured in Oregon for various time periods:

In the OCR, Lost Lake's SAR was ~0.1 cm y^{-1} in the last ~1000 y (Long et al., 2007) and Little Lake's MAR was ~0.14 cm y^{-1} in the last ~1100 y (Long et al., 1998). Adjacent Triangle Lake increased from 0.09 cm y^{-1} (6.0-3.5 k y BP) to 0.17 cm y^{-1} (3.5 k y BP to 1900 AD) to 0.21 cm y^{-1} in the last century (Kusler, 2012). On the Oregon coast, Bradley Lake had a SAR of 0.83 +/-0.04 mm y^{-1} up to the last 1000 y (Kelsey et al., 2005), and Devils Lake had a background rate of 0.025 g cm^{-2} y^{-1}, spiking in 1909 at 0.14 g cm^{-2} y^{-1} and dropping, then rising steadily since 1930's to 0.06 g cm^{-2} y^{-1} in the 1990's (Eilers et al., 1996). Researchers at Triangle Lake and Devils Lake attributed the increase in SAR and MAR to anthropogenic activities in the 20th century. However, two researched lakes had much higher rates. Researchers at Upper Squaw Lake in southern Oregon reported an increase in SAR to ~4 cm y^{-1} from a background of 0.3 cm y^{-1}, attributed to land use (Colombaroli and Gavin, 2010). Dorena Lake, a reservoir in the Cascade Range, was found to have an average rate of 0.55-1.24 cm y^{-1}, with the peak in 1954-1964 AD of 2.1 and 2.7 cm y^{-1} for two cores (Ambers, 2001). Both of these lakes had been highly impacted by land use, and were within different lithologic units. Comparing to the other lakes in the OCR or on the coast, Loon Lake has both high rates of land use, as well as high elevation relief (Figure 2), which partly explain the difference. A further look at catchment to lake area ratio, precipitation, intensity and magnitude of timber harvest, and other factors would elucidate the differences in accumulation rates.

4.3 Hydrologic event correlation

A few studies have shown a correlation between event precipitation or discharge and bed thickness (Page et al., 1994; Eden and Page, 1998; Page et al., 2010; Schiefer et al., 2011) or stormy periods (Brown et al., 2000). For example, at Lake Tutira, which has a daily precipitation record from 1894 to 1988, thicknesses of storm layers were scaled to threshold precipitation amounts, and human impacts on the landscape were shown to lower the threshold of landsliding. Additionally, stormy periods at Tutira were identified based on frequency of storm layers.

Instrumentation within Loon Lake catchment is not directly tied to event deposition in the lake as in Lake Tutira and few others (Schiefer et al., 2011). However, as described in the previous section, there is a fairly strong correlation between discharge (Q) at the Mill Creek gage downstream of Loon Lake and Q at the Elkton gage. Additionally, there is a strong correlation between Elkton Q (Figure A7) and layer mass on a log-log scale (r_s = 0.62, p < 0.0001; Figure 13). The six event beds in the contemporary period (highest mass layers) are correlated with some of the highest peak flows at Elkton gage (Figure 13). However, it is evident in the varved region at the top of the sedimentary column, not all layer masses scale with flood magnitude, as recorded by the Elkton record. For example, the 1965 WY peak Q on the Umpqua at Elkton was the largest on record at that station. The Loon Lake layer mass for that year is only 2.8 g cm^{-2}, 3rd from highest in the contemporary sediment record. There are several reasons for the correlation not being stronger. Sediment exhaustion within the system is one explanation of why the layer mass does not scale with thickness. Storage of sediment is another. The thicker winter layers from 1943-1978 indicate that this was a stormy period, reflecting the cool-phase of the PDO, which is reflected in the increase in average annual precipitation and discharge. Sediment had been moving through the system, apparently already delivering to this sink for 21 years. So, perhaps at one time what would have been a very large delivery of sediment to the lake, had been lessened because of a few large storms and many moderate storms prior to 1965, removing sediment from storage in the fluvial system. The thick deposit in 1997 (E1) may be an example of the corollary, where not much sediment had been moving to the sink in previous years,

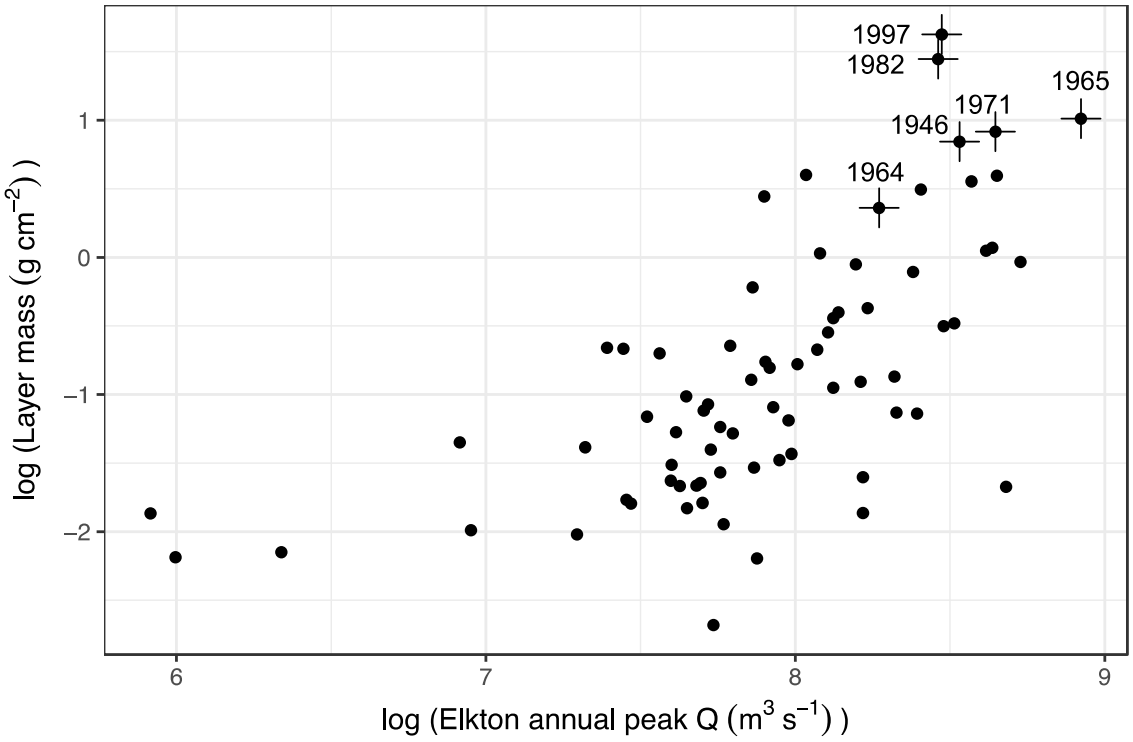

Figure 13. Layer mass and annual peak discharge at Elkton. The relationship is shown by a scatterplot (log-log) of layer mass in the varved contemporary period and annual peak discharge (Q) at the Umpqua R. at Elkton for the water years WY 1939-2012. Event beds E1-6, with the most mass in the contemporary period, are indicated by stars labeled by WY.

and a less-extreme event than the WY 1965 storm (by the Elkton record) resulted in a much larger deposit because the fluvial system was not supply-limited. There are examples in other research where the magnitude of the event does not produce the expected resulting sediment. At Lake Tutira, Cyclone Bola (1988) with a record 753 mm rainfall produced only 70% of the sediment of a 692-mm precipitation storm (1938) (Page, et al., 1994). Outside of lake settings, in Redwood Creek of northern California, two similar storms in that catchment (1955, 1964) produced much different amounts of sediment, the later one producing much more (Kelsey, 1980). In New Zealand, soil was still recovering from the 1938 storm, so 1988 produced less. In California, the first storm may have primed the landscape for the second. In both situations, the threshold of failure had apparently been lowered by land use.

4.4 Role of forcings

It has been shown that background sedimentation comprises most of the sediment (84%), which is a combination of autochthonous by-products and mass influx from the catchment during low flow and low- to moderate-discharge floods from the catchment. However, event beds bias the record with contribution of 16% of the mass of the core, within effectively instantaneous deposits. Of the 23 event beds, it is likely that 20 were deposited by high discharge fluvial events, and constitute 10% of the core by mass deposited in 1.3% of the time represented by the core (assuming 1 year per deposit; 20 y out of 1500 y, 2012-515 AD). This shows the significant impact of extreme storms in the catchment and in the sedimentary column. More emphatically, this estimate of emplacement of 10% of the mass in 1.3% of the time is a conservative estimate because it is probable that most of those deposits occurred within hours or days, not months. However, using the present as a template for the past, mass of event beds E1-E6 each fill up their entire winter varve, essentially represent 1 year because we did not separate out individual storms within a varve.

To further evaluate the relative significance of event bed mass throughout the long core, a flood frequency-type analysis was completed for mass of light layers in Core 02aN as measured on the x-radiograph. The early part of the core, well before large-scale timber harvest, was divided into twenty-nine 50-year bins (representing calibrated years AD 464 – 1912). All light layers and thick graded layers were identified within all bins. Two bins did not have visually identifiable light layers, containing only mottled beds and indistinct layers, so these were dropped from the analysis (USGS 1981). Within each of the remaining 27 bins, the layer with the greatest mass was labeled as the maximum, equivalent to the instantaneous peak discharge for flood analysis. A flood frequency analysis was performed, following methods in Colombaroli and Gavin (2010) and OSU (2007). This analysis yielded return intervals for each of the thickest light layers used in the analysis, and enabled a calculation of layer mass at the 2-, 5-, 10-, 25-, 50-, 100-, and 200-y return intervals to which a line was fit (blue points and line in Figure 14). This then allowed interpolation of return intervals of mass of layers in question (equivalent of peak discharges).

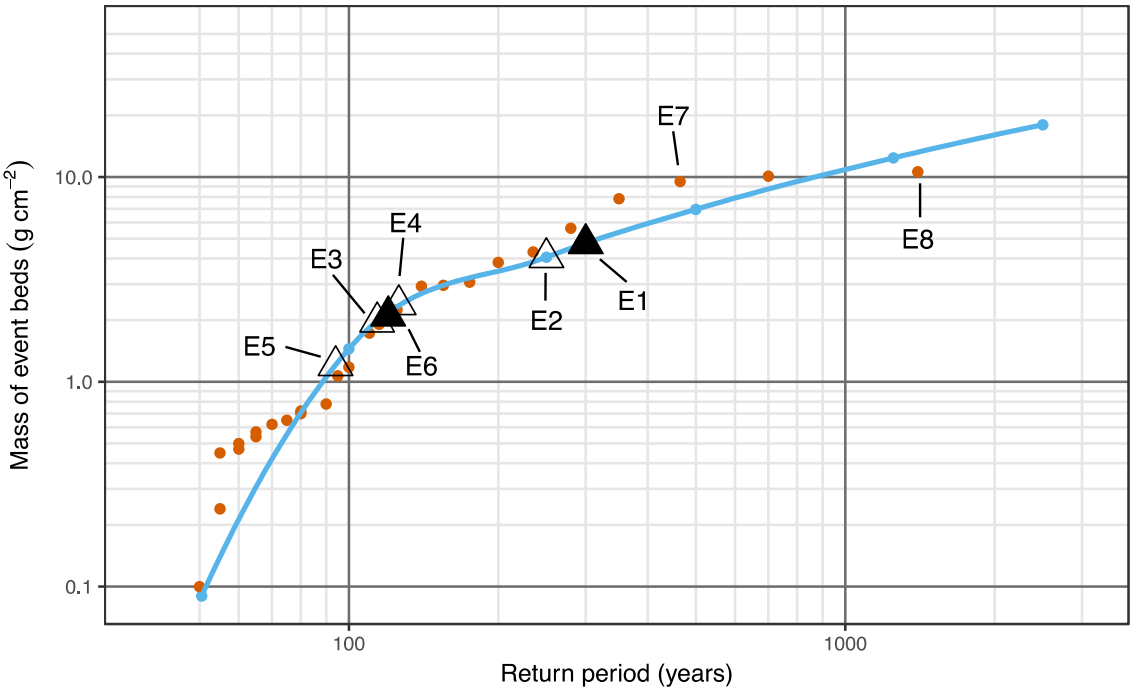

Figure 14. Flood frequency-type analysis for mass of event beds in Core 02aN. From the data analysis, the blue line and points on the line approximate a Log Pearson Type III distribution, except at an excursion in the more frequent, smaller magnitude beds. Red points represent the largest event beds by dry mass in every 50-year bin of the core back to ~460 cal year A.D., except the last 100 years, which instead are represented by two filled triangles at interpolated return periods on the distribution, WY 1946 and 1997. The open triangles show the mass of the other event beds in the last 100 years, and their interpolated return periods on the distribution. E7 and 8 were part of the analysis, and are indicated by name. The analysis excluded E21 because this event has very different sedimentary characteristics, implying a different mechanism (USGS, 1982). A loess smoothing method was applied to the blue distribution line with a span of 0.7 to control the amount of smoothing.

For example, using the line of fit, which approximates a Log Pearson Type III distribution, the two thickest layers from the two most recent 50 year bins (last 100 years) were interpolated for their return intervals, as were the other four events in the contemporary period (Figure 14). Because the whole-core time period was broken into 50-year bins, the resulting return periods were multiplied by 50. Event bed E21 was excluded from the entire analysis because it has very different sedimentary characteristics, implying a different mechanism of deposition (USGS, 1982).

The results of the flood analysis show that event beds during the contemporary and the gap period are significantly large considering the 1500-y span of the sedimentary column. For example, all six event beds in the years 1939-2012 AD apparently have return intervals from 90 to 300 years (Figure 14) so indeed are extraordinary. Further, the two largest mass beds in the last 100 years, 2.1 g/cm^2 and 4.7 g/cm^2 during 1946 and 1997, respectively, were interpolated on the distribution, whereby the result is return periods of 115 years and 300 years. Additionally, during the last 200 years, there have been more events per length of the core (Figure A12) and though they are not all the largest, they have relatively large return intervals.

During the contemporary period, there were two forcings acting upon the catchment, timber harvest and floods. The forcings acted together to produce elevated sedimentation in the lake. During the time of the cool-phase of the PDO timber harvest was at its peak in the catchment. Not only were there four graded beds indicating large storms with sustained sediment input during this period, most of the other years had thick winter layers, indicating moderate size storms, so the MAR was elevated. As the PDO phase switched to warm and dry, average annual sediment accumulation in the lake decreased immediately, even as timber harvest continued. However, the two thick event beds in 1997 and 1982 in response to large storms contributed a large portion of the sediment to the lake (e.g. Ambers, 2001), indicating that the catchment had stored sediment in the fluvial system and/or hillslopes from previous perturbation, and it was then delivered at an elevated discharge, but by storms with a lower recurrence interval than would have been necessary without a prior sediment-producing perturbation.

A second example of forces acting together to deliver sediment occurred before large-scale anthropogenic impact, during the “gap” period. During the mid-1700’s and mid-1800’s large fires and storms occurred in the catchment (Table A1). During this time, the MAR is significantly higher than the overall early period but not significantly higher than the early contemporary period. Essentially, denudation of the landscape by fire may have acted in the same role that timber harvest played later, which is to produce sediment that the moderate and extreme storms will bring to the lake. As an example from a comparison of two catchments in coastal central California, if high intensity precipitation assaults a denuded landscape, more erosion is likely to occur. Annual sediment yield following fire in one catchment was an order-of-magnitude higher than it was in a nearby catchment which was also burned, but received minimal precipitation (Warrick et al., 2012). At Loon Lake, besides fire and storms, a third and fourth actor may have been involved as well. At 1700 AD, the CSZ M_w 9.0 earthquake, which although does not appear to have left a very large event bed (most likely E9), may have primed the landscape for subsequent landsliding and increased hillslope erosion. Additionally, this gap period includes early logging which would have been impactful on soil and streambeds with felling of large old-growth trees, dragging especially large logs down hillslopes and through stream beds. This time also included the beginning of land clearance in Ash Valley above the lake, which resulted in loss of streambank vegetative root strength. It is during this time that the two unusual deposits E7 and E8 were added to the lake.

Earthquakes themselves contribute sediment at Loon Lake by either co-seismic failures, such as could have been the mechanism of delivery of event bed E21, 4% of the mass of the core, or by post-seismic failures. If E21 was seismically-related, it presented sediment to the lake much differently than all other earthquake-driven sedimentation within this sediment column. Most sedimentation in the lake driven by earthquake must be by the same delivery mechanism as fire and timber harvest: through the fluvial system, as hyperpycnal turbidity currents, following destabilization of the hillslope, primed for sediment production, and delivered by landsliding in the upper catchment and eventual fluvial entrainment. At Lake Paringa in New Zealand, it was found

that average sedimentation rate by aseismic deposition was 0.21 +/- 0.05 g cm^{-2} y^{-1}, and post-seismic was 0.60 +/- 0.21 g cm^{-2} y^{-1}, and the least mass of the three mechanisms by co-seismic deposition (Howarth et al., 2012). At Loon Lake, sediment produced and delivered strictly by earthquakes could not be separated from that produced and delivered from other perturbations, although many event beds are coeval in time with estimated ages of earthquakes. Apparently, however, besides during peak timber harvest, MAR was highest in the entire sedimentary column following two earthquakes with the largest estimations of magnitude in the lifetime of this core – 1700 and ~700 AD (Tables 7 and 8).

As for the event which created the lake, a landslide initiated by the failure of a bedding plane within the bedrock, Baldwin (1958) suggested that it was sudden and catastrophic, different than the slow earth movement of a few other OCR landslide-dammed valleys. He asked whether an earthquake may have been the trigger of the failure which formed Loon Lake. Whatever the triggering event, it apparently occurred before ~460 AD (the approximate age of the bottom of Core 02aN), possibly pre-dating the first ^{14}C age of the lake in 1962 (Ferguson and Libby, 1962), whose 95% probability range of the calibrated date is 395-660 AD, with a median date of 541 AD.

Throughout time in this core, regardless of which event occurred in the catchment and the variability of the measured parameters of each event, the background sedimentation has little variance (Figure 9). Earthquake and fires have acted through most of the history of the core, providing sediment to the lake by large storms, but also by extra sediment delivered by normal winter precipitation. Timber harvest has acted in a short time, but similarly to earthquake and fire, in increasing supply of sediment to the fluvial system, then delivered to the lake. However, all have been driven by floods of varying magnitude.

All of these forcings act on the landscape, and the landscape recovers with time. Burned over areas regenerate vegetation, harvested areas recover, evacuated hollows from landslides rebuild soil and regenerate vegetation. Timber harvest, however, can leave a legacy of road-building. Roads persist on the landscape, reroute water, and deliver sediment to streams and lower hillslope. Late last century, forest rules were implemented which would lessen the impacts

of roads by better road-building away from streams and off of vulnerable slopes. Even so, as long as timber harvest and associated roads exist, they are acting as the sediment-driving force that has replaced the catchment's next highest recurrence interval disturbance – pre-suppression forest fire (Kennedy and Spies, 2004).

CONCLUSION

During the early contemporary period of this core, 1939-1978, which is the period of onset of and peak of major timber harvest in the catchment and the cool-wet phase of the PDO, the mass accumulation rate (MAR) was significantly higher than in 1979-2012. Even when mass of large events is removed (event-free depth) and only the background sediment accumulation is considered, the difference in the rates between the two periods is still significant. The two forcings at work during this period – harvest activities and floods - cannot be disentangled, and the possible moderating influence of better forest harvest practices could not be identified with the techniques in this research.

The first 1100 y of the sedimentary column (515 – 1671 AD) has a lower estimated mean MAR than the 75 y of the contemporary period and the 270-y period in between (1671-1939 AD). It appears that the estimated MAR during the early contemporary period is higher than most of the rest of the core and that timber harvesting and associated road building may be associated with a lowering of the threshold by which extreme hydrologic events mobilize and deliver sediment to the lake.

The consequence of multiple forcings acting together, such as harvest activities and floods, is to increase MAR, as was also the case during the gap period (between 1671-1939 AD), where large fires, extreme floods, and the possible destabilization of hillslopes occurred following the 1700 AD CSZ M_w 9.0 earthquake. Earthquakes are probably recorded in the sediment by co-seismic landscape destabilization and post-seismic sediment delivery to the lake by moderate and high-magnitude flood events in the form of hyperpycnal flows, and likely on at least one occasion by a debris flow delivered directly to the lake.

The fidelity of the sedimentary record is high in the eutrophic contemporary period, deposited as varves, and throughout the core as preserved event beds. Within the varved contemporary period, known floods in the region are recorded as thick graded event beds.

The role of timber harvest and fire both can be elucidated further by use of stable isotopes to identify the specific source of organic matter within the sedimentary column, and

charcoal analysis and further use of forms of magnetic susceptibility to identify peak times of forest fire.

BIBLIOGRAPHY

Allen PA. 2008. From landscapes into geological history. Nature 451: 17-20.

Ambers R. 2001. Using the sediment record in a western Oregon flood-control reservoir to assess the influence of storm history and logging on sediment yield. Journal of Hydrology 244: 181-200.

Amerise IL, Marozzi M, Tarsitano A. 2016. Package 'pvrank'. Accessed from https://cran.r-project.org/web/packages/pvrank/index.html

Baldwin EM. 1958. Landslide lakes in the Coast Range of Oregon. Geological Newsletter, Geological Society of the Oregon Country 24: 23–24.

Baldwin EM. 1974. Eocene stratigraphy of southwestern Oregon. Oregon Department of Geology and Mineral Industries Bulletin 83. 40 pp.

Baldwin EM. 1981. Geology of Oregon, 3rd edition. Kendall-Hunt Publishing Co.: Dubuque, Iowa

Beaulieu JD, Hughes PW. 1975. Environmental Geology of Western Coos and Douglas Counties, Oregon. Oregon Department of Geology and Mineral Industries Bulletin 87. 148 pp.

Beck C. 2009. Late Quaternary lacustrine paleo-seismic archives in north-western Alps: Examples of earthquake-origin assessment of sedimentary disturbances. Earth-Science Reviews 96: 327-344.

Beschta RL. 1978. Long-term patterns of sediment production following road construction and logging in the Oregon Coast Range. Water Resources Research 14: 1011-1016.

Biosystems. 2003. Elliott State Forest Watershed Analysis. Corvallis, Oregon. Accessed from https://services.oregon.gov/ODF/Documents/WorkingForests/ElliottStateForestWatershedAnalysis.pdf

Björck S, Wohlfarth B. 2001. ^{14}C chronostratigraphic techniques in paleolimnology. In Tracking Environmental Change Using Lake Sediments. Volume 1: Basin Analysis, Coring, and Chronological Techniques, Last WM, Smol JP (eds). Kluwer Academic Publishers: Dordrecht; 1-41.

Blanton GI. 1970. The characterization and physical-chemical treatability of log pond waters. MS thesis. Corvallis, Oregon State University. 56 pp.

Bronk Ramsey C. 2009. Bayesian analysis of radiocarbon dates. Radiocarbon 51: 337-360.

Bronk Ramsey C, Dee M, Lee S, Nakagawa T, Staff R. 2010. Developments in the calibration and modelling of radiocarbon dates. Radiocarbon 52: 953-961.

Bronk Ramsey C, Staff RA, Bryant CL, Brock F, Kitagawa H, van der Plicht J, Schlolaut G, et al. 2012. A complete terrestrial radiocarbon record for 11.2 to 52.8 kyr B.P. Science 338*:* 370-374.

Bronk Ramsey C. 2013. Oxcal v4.2.4

Brown S, Bierman PR, Lini A, Southon J. 2000. 10000 yr record of extreme hydrologic events. Geology 28: 335-338.

Brown S, Bierman PR, Lini A, Davis PT, Southon J. 2002. Reconstructing lake and drainage basin history using terrestrial sediment layers: analysis of cores from a post-glacial lake in NE, USA. Journal of Paleolimnology 28: 219-236.

Cohen AS. 2003. Paleolimnology: The History and Evolution of Lake Systems. Oxford University Press: New York.

Cohen WB, Spies TA, Alig RJ, Oetter DR, Maiersperger TK, Fiorella M. 2002. Characterizing 23 years (1972-95) of stand replacement disturbance in western Oregon forests with Landsat imagery. Ecosystems 5: 122-137.

Crozier MJ. 1986. Landslides: Causes, Consequences, and Environment. Croom Helm Ltd, Kent, UK

Colombaroli D, Gavin DG. 2010. Highly episodic fire and erosion regime over the past 2000 y in the Siskiyou Mountains, Oregon. Proceedings of the National Academy of Sciences of the United States of America 107: 18909-18914.

Curtiss DA, Collins CA, Oster EA. 1984. Water-Resources of Western Douglas Co., Oregon. US Geological Survey Water-Resources Investigations, Report 83-4017. 87 pp.

Dadey KA, Janecek T, Klaus A. 1992. Dry-bulk density: its use and determination. In Proceedings of the Ocean Drilling Program, Scientific Results, Taylor B, Fujioka K et al. (eds). 126: 551-554.

Dadson SJ, Hovius N, Chen H, Dade WB, Lin JC, Hsu ML, Lin CW, et al. 2004. Earthquake-triggered increase in sediment delivery from an active mountain belt. Geology 32: 733-736.

Daily Alta California. 1891. Shipping Intelligence. March 5, 1891. 84, 64.

Dearing JA. 1991. Lake sediment records of erosional processes. Hydrobiologia 214: 99-106.

Dean WE, Bradbury JP. 1993. Characteristics of sediments from selected lakes of Oregon and Washington and their potential for obtaining high-resolution paleoclimate records. US Geological Survey Open-File Report 93-212. 21 pp.

Dietrich WE, Dunne T. 1978. Sediment budget for a small catchment in mountainous terrain. Zeitschrift für Geomorphologie, Supplement 29: 191-206.

Dodson S. 2005. Introduction to Limnology. McGraw-Hill: Boston

Douglas Co. 2009. Natural Hazard Mitigation Plan. Douglas County, Oregon. Accessed from www.co.douglas.or.us/planning/natural_hazard/PDFs/flood.pdf

Eden DN, Page MJ. 1998. Palaeoclimatic implications of a storm erosion record from late Holocene lake sediments, North Island, New Zealand. Palaeogeography, Palaeoclimatology, Palaeoecology 139: 37-58.

Edmondson WT. 1991. Sedimentary record of changes in the condition of Lake Washington. Limnology and Oceanography 36: 1031-1044.

Eilers JM, Bernert JA, Gubala CP, Whiting MC, Engstrom DR, Charles DF. 1996. Recent paleolimnology of Devils Lake, Oregon. Northwest Science 70: 13-27.

Enkin RJ, Dallimore A, Baker J, Southon JR, Ivanochko. 2012. A new high-resolution radiocarbon Bayesian age model of the Holocene and Late Pleistocene from core MD02-2494 and others, Effingham Inlet, BC, Canada; with an application to the paleoseismic event chronology of the Cascadia subduction zone. Canadian Journal of Earth Sciences 50: 746-760.

Environmental Systems Research Institute. 1998. ARCMAP. Environmental Systems Research Institute Inc.: Redlands, California

Fergusson GJ, Libby WF. 1962. UCLA radiocarbon dates I. Radiocarbon 4: 109-114.

Francus P, Bradley RS, Lewis T, Abbott M, Stoner M. 2008. Limnological and sedimentary processes at Sawtooth Lake, Canadian High Arctic, and their influence on varve formation. Journal of Paleolimnology 40: 963-985.

Franklin JF, Dyrness CT. 1988. Natural Vegetation of Oregon and Washington. OSU Press: Oregon State University, Corvallis, Oregon

Gagnon AR, McNichol AP, Donoghue JC, Stuart DR, von Reden K, Hayes JM, Schneider RJ et al. 2000. The NOSAMS sample preparation laboratory in the next millennium: Progress after the WOCE program. Beam Interactions with Materials and Atoms 172: 409-415. Accessed from http://dx.doi.org/10.1016/S0168-583X(00)00201-9

Garrison-Laney CE, Abramson-Ward HF, Carver GA. 2006. A 3,000 year record of tsunami deposition from the southern end of the Cascadia subduction zone. In Pacific Cell Friends of the Pleistocene Field Trip Guidebook—The Triangle of Doom: Arcata, Calif., Signatures of Quaternary Crustal Deformation in the Mendocino Deformation Zone (MDZ), Hemphill-Haley MA, McPherson R, Patton JR, et al. (eds); 309–323.

GLO. General Land Office. 1874. Accessed from http://www.blm.gov/or/landrecords/survey/yPlatView1_2.php?path=POR&name=t230s100w_001.jpg

Gilbert R, Crookshanks S, Hodder KR, Spagnol J, Stull RB. 2006. The record of an extreme flood in the sediments of montane Lillooet Lake, B.C.: implications for paleoenvironmental assessment. Journal of Paleolimnology 35: 737-745.

Geotek Limited. Accessed from http://www.geotek.co.uk/products/gammadensity

Giguet-Covex C, Arnaud F, Enters D, Poulenard J, Millet L, Francus P, David F, et al. 2012. Frequency and intensity of high-altitude floods over the last 3.5 ka in northwestern French Alps (Lake Anterne). Quaternary Research 77: 12-22.

Gilmore G, Hemingway JD. 1995. Practical Gamma-Ray Spectrometry. Wiley: New York

Goldfinger C, Nelson CH, Morey AE, Johnson JE, Patton JR, Karabanov E, Gutiérrez-Pastor J, et al. 2012. Turbidite Event History -- Methods and Implications for Holocene Paleoseismicity of the Cascadia Subduction Zone. US Geological Survey Professional Paper 1661-F. 170 pp.

Gomez B, Corral A, Orpin AR, Page MJ, Pouderoux H, Upton P. 2015. Lake Tutira paleoseismic record confirms random, moderate to major and/or great Hawke's Bay (New Zealand) earthquakes. Geology 43: 103-106.

Gray AB, Pasternack GB, Watson EB. 2010. Hydrogen peroxide treatment effects on the particle size distribution of alluvial and marsh sediments. The Holocene 20: 293-301.

Hairston-Strang AB, Adams PW, Ice GG. 2008. The Oregon Forest Practices Act and Forest Research. In Hydrological and Biological Responses to Forest Practices, Stednick JD (ed). Springer; 95-113.

Hatten JA, Goni MA, Wheatcroft RA. 2012. Chemical characteristics of particulate organic matter from a small, mountainous river system in the Oregon Coast Range, USA. Biogeochemistry 107: 43-66.

Hedges JI, Stern JH. 1984. Carbon and nitrogen determinations of carbonate containing solids. Limnology and Oceanography 49: 657-663.

Heimsath AM, Dietrich WE, Nishiizumi K, Finkel RC. 2001. Stochastic processes of soil production and transport: Erosion rates, topographic variation and cosmogenic nuclides in the Oregon Coast Range. Earth Surface Processes and Landforms 26: 531-552.

Ho I, Ching-Yan L. 1987. Microbial and chemical properties of log ponds along the Oregon coast. US Department of Agriculture, Forest Service, Pacific Northwest Research Station. Research Note PNW-RN-467. 8 pp.

Hofmann MH, Hendrix MS. 2010. Depositional processes and the inferred history of ice-margin retreat associated with the deglaciation of the Cordilleran Ice Sheet: The sedimentary record from Flathead Lake, northwest Montana, USA. Sedimentary Geology 223: 61-74.

Hovius N, Meunier P, Ching-Weei L, Hongey C, Yue-Gau C, Dadson S, Ming-Jame H, Lines M. 2011. Prolonged seismically induced erosion and the mass balance of a large earthquake. Earth and Planetary Science Letters 304: 347-355.

Howarth JD, Fitzsimons SJ, Jacobsen GE, Vandergoes MJ, Norris RJ. 2013. Identifying a reliable target fraction for radiocarbon dating sedimentary records from lakes. Quaternary Geochronology 17: 68-80.

Howarth JD, Fitzsimons SJ, Norris RJ, Jacobsen GE. 2012. Lake sediments record cycles of sediment flux driven by large earthquakes on the Alpine fault, New Zealand. Geology 40: 1091-1094.

Jackson M, Roering JJ. 2009. Post-fire geomorphic response in steep, forested landscapes: Oregon Coast Range, USA. Quaternary Science Reviews 28: 1131-1146.

Jerolmack DJ, Paola C. 2010. Shredding of environmental signals by sediment transport. Geophysical Research Letters 37: L19401.

Johnson MG, Beschta RL. 1980. Logging, infiltration capacity, and surface erodibility in western Oregon. Journal of Forestry 78: 334-337.

Jones BE, Stearns HT. 1928. Water-power resources of Umpqua River and its tributaries, Oregon. US Geological Survey Water Supply Paper 636-F. 121 pp.

Jones JA, Grant G. 1996. Peak flow responses to clear-cutting and roads in small and large basins, western Cascades, Oregon. Water Resources Research 32: 959-974.

Kämpf L, Brauer A, Dulski P, Lami A, Marchetto A, Gerli S, Ambrosetti W, et al. 2012. Detrital layers marking flood events in recent sediments of Lago Maggiore (N. Italy) and their comparison with instrumental data. Freshwater Biology 57: 2076-2090.

Karlin RE, Abella SE. 1992. Paleoearthquakes in the Puget Sound region recorded in sediments from Lake Washington, U.S.A. Science 258: 1617–1620.

Karlin RE, Holmes M, Abella SEB, Sylwester R. 2004. Holocene landslides and a 3500-year record of PNW earthquakes from sediments in Lake Washington. Geological Society of America Bulletin 116: 94-108.

Kennedy RSH, Spies TA. 2004. Forest cover changes in the Oregon Coast Range from 1939 to 1993. Forest Ecology and Management 200: 120-147.

Kennedy RE, Yang ZQ, Cohen WB, Pfaff E, Braaten J, Nelson P. 2012. Spatial and temporal patterns of forest disturbance and regrowth within the area of the Northwest Forest Plan. Remote Sensing of Environment 122: 117-133.

Kelsey HM. 1980. A sediment budget and an analysis of geomorphic process in the Van-Duzen River basin, north coastal California, 1941-1975 - summary. Geological Society of America Bulletin 91: 190-195.

Kelsey HM, Nelson AR, Hemphill-Haley E, Witter RC. 2005. Tsunami history of an Oregon coastal lake reveals a 4600 yr record of great earthquakes on the Cascadia subduction zone. Geological Society of America Bulletin 117: 7-8.

Kuivila KM, Murray JW. 1984. Organic matter diagenesis in freshwater sediments: The alkalinity and total CO_2 balance and methane production in the sediments of Lake Washington. Limnology and Oceanography 29: 1218-1230.

Kusler J. 2012. A 7500-year paleolimnological record of environmental change and salmon abundance in the Oregon Coast Range. MS thesis. Eugene, University of Oregon. 40 pp.

Lane JW. 1987. Relations between geology and mass movement features in a part of the East Fork Coquille River Watershed, Southern Coast Range, Oregon. MS thesis. Corvallis, Oregon State University. 107 pp.

Lauterbach S, Chapron E, Brauer A, Huls M, Gilli A, Arnaud F, Piccin A, et al. 2012. A sedimentary record of Holocene surface runoff events and earthquake activity from Lake Iseo (Southern Alps, Italy). The Holocene 22: 749-760.

Leonard LJ, Currie CA, Mazzotti S, Hyndman RD. 2010. Rupture area and displacement of past Cascadia great earthquakes from coastal coseismic subsidence. Geological Society of America Bulletin 122: 2079-2096.

Long CJ, Whitlock C, Bartlein PJ, Millspaugh SH. 1998. A 9000-year fire history from the Oregon Coast Range, based on a high-resolution charcoal study. Canadian Journal of Forest Research 28: 774-787.

Long CJ, Whitlock C, Bartlein PJ. 2007. Holocene vegetation and fire history of the Coast Range, western Oregon, USA. The Holocene 17: 917-926.

MacDonald GM, Case RA. 2005. Variation in the Pacific Decadal Oscillation over the past millennium. Geophysical Research Letters 32: L08703.

Mantua NJ, Hare SR, Zhang Y, Wallace JM, Francis RC. 1997. A Pacific interdecadal climate oscillation with impacts on salmon production. Bulletin of the American Meteorological Society 78: 1069-1079.

May CL, Gresswell RE. 2003. Processes and rates of sediment and wood accumulation in headwater streams of the Oregon Coast Range, USA. Earth Surface Processes and Landforms 28: 409-424.

May CL, Gresswell RE. 2004. Spatial and temporal patterns of debris-flow deposition in the Oregon Coast Range, USA. Geomorphology 57: 135-149.

Meyers PA, Lallier-Vergès E. 1999. Lacustrine sedimentary organic matter records of late quaternary paleoclimates. Journal of Paleolimnology 21: 345-372.

Miller RR. 2010. Is the Past Present? Historical Splash-Dam Mapping and Stream Disturbance Detection in the Oregon Coastal Province. MS thesis. Corvallis, Oregon State University. 96 pp.

Milliman JD, Syvitski JPM. 1992. Geomorphic tectonic control of sediment discharge to the ocean - the importance of small mountainous rivers. Journal of Geology 100: 525-544.

Minckley T, Whitlock C. 2000. Spatial variation of modern pollen in Oregon and southern Washington, USA. Review of Palaeobotany and Palynology 112: 97-123.

Mulder T, Alexander J. 2001. The physical character of subaqueous sedimentary density flows and their deposits. Sedimentology 48: 269-299.

Montgomery DR, Schmidt KM, Greenberg HM, Dietrich WE. 2000. Forest clearing and regional landsliding. Geology 28: 311-314.

Moreno A, Valero-Garcés BL, González-Sampériz P, Rico M. 2008. Flood response to rainfall variability during the last 2000 years inferred from the Taravilla Lake record (Central Iberian Range, Spain). Journal of Paleolimnology 40: 943-961.

Morey AE, Goldfinger C, Briles CE, Gavin DG, Colombaroli D, Kusler JE. 2013. Are great Cascadia earthquakes recorded in the sedimentary records from small forearc lakes? Natural Hazards and Earth Systems Sciences 13: 2441-2463.

Morris WG. 1934. Forest fires in western Oregon and western Washington. Oregon Historical Quarterly 35: 313-339.

Nelson AR, Asquith AC, Grant WC. 2004. Great earthquakes and tsunamis of the past 2000 years at the Salmon River estuary, central Oregon coast, USA. Bulletin of the Seismological Society of America 94: 1276-1292.

Nelson AR, Kelsey HM, Witter RC. 2006. Great earthquakes of variable magnitude at the Cascadia subduction zone. Quaternary Research 65: 354-365.

Nesje A. 1992. A piston corer for lacustrine and marine sediments. Arctic and Alpine Research 24: 257-259.

Olsson LU. 1986. Radiometric dating. In Handbook of Holocene Palaeoecology and Palaeohydrology, Berglund, BE (ed). Wiley: New York; 273-312.

ODEQ. 1992. Laboratory Analytical Storage and Retrieval (LASAR), Station 13813. Oregon Department of Environmental Quality. Accessed from http://deq12.deq.state.or.us/lasar2/

ODF. 2011. Elliott State Forest Management Plan. Oregon Department of Forestry and Department of State Lands. Accessed from www.oregon.gov/ODF/Documents/AboutODF/2011FMPElliott.pdf

Oregon. 2001. Oregon Forest Practices Act. State of Oregon. Accessed from http://www.leg.state.or.us/ors/527.html

Oregonian. 1890. “In Southern Oregon: Greatest Flood Known Since the Country Was Settled…” Morning Oregonian 30(9156): 1. Accessed from http://umpqua.library.oregonstate.edu/node/22761

OSU. 2007. Analysis Techniques: Flood Analysis. Oregon State University. Accessed from http://streamflow.engr.oregonstate.edu/analysis/floodfreq/index.htm

O’Sullivan PE. 1983. Annually-laminated lake sediments and the study of Quaternary environmental changes – a review. Quaternary Science Reviews 1: 245-313.

Orpin AR, Carter L, Page MJ, Cochran UA, Trustrum NA, Gomez B, Palmer AS, et al. 2010. Holocene sedimentary record from LakeTutira: A template for upland watershed erosion proximal to the Waipaoa Sedimentary System, northeastern New Zealand. Marine Geology 270: 11-29.

Orr PW. 1963. Windthrown timber survey in the Pacific Northwest, 1962. US Department of Agriculture, Forest Service, Pacific Northwest Region. Portland, Oregon. 48 pp.

Osleger AD, Heyvaert AC, Stoner JS, Verosub KL. 2009. Lacustrine turbidites as indicators of Holocene storminess and climate: Lake Tahoe, CA and NV. Journal of Paleolimnology 42: 103-122.

Owens P, Slaymaker O. 1993. Lacustrine sediment budgets in the coast mountains of British Columbia, Canada. In Geomorphology and Sedimentology of Lakes and Reservoirs, McManus J, Duck RW (eds). John Wiley & Sons: Chichester; 105-123.

Page MJ, Trustrum NA, DeRose RC. 1994. A high resolution record of storm induced erosion from lake sediments, New Zealand. Journal of Paleolimnology 11: 333-348.

Page MJ, Trustrum NA. 2010 Storm frequency and magnititude in response to Holocene climate variability, Lake Tutira, North-Eastern New Zealand. Marine Geology 270: 30-44.

Phillips J. 2015. Personal communication. Jerry Phillips, Retired Coos District Forester, Elliott State Forest.

Ralph FM, Dettinger MD. 2011. Storms, floods and the science of atmospheric rivers. Eos, Transactions, American Geophysical Union 92: 265–266.

Ralph FM, Dettinger MD 2012. Historical and national perspectives on extreme west coast precipitation associated with atmospheric rivers during December 2010. Bulletin of the American Meteorological Society 93: 783-790.

Reimer PJ, Bard E, Bayliss A, Beck JW, Blackwell PG, Bronk Ramsey C, Grootes PM, et al. 2013. IntCal13 and Marine13 radiocarbon age calibration curves 0-50,000 years cal BP. Radiocarbon 55: 1869-1887.

Reid LM, Dunne T. 1984. Sediment production from forest road surfaces. Water Resources Research 20: 1753-1761.

Reiter M. 2015. Personal communication. Maryanne Reiter. Hydrologist, Weyerhauser Company.

Reneau SL, Dietrich WE. 1989. Depositional history of hollows on steep hillslopes, coastal Oregon and Washington. National Geographic Research 6: 220-230.

Rinella JF. 1979. Lakes of Oregon. Volume 6: Douglas County. US Geological Survey Open-File Report. 123 pp.

Ritchie A, Bourgeois J. 2010. Lake Quaternary Sediment Source and Deposition of Lake Ozette. Department of Interior, National Park Service. Accessed from http://www.cfr.washington.edu/research.cesu/reports/J9W88050001_final_report.pdf

Roering JJ, Gerber M. 2005. Fire and the evolution of steep, soil-mantled landscapes. Geology 33: 349-352.

Roering JJ, Kirchner JW, Dietrich WE. 2005. Characterizing structural and lithologic controls on deep-seated landsliding: Implications for topographic relief and landscape evolution in the Oregon Coast Range, USA. Geological Society of America Bulletin 117: 654-668.

Roering JJ, Marshall J, Booth AM, Mort M, Jin Q. 2010. Evidence for biotic controls on topography and soil production. Earth and Planetary Science Letters 298: 183-190.

Romans BW, Castelltort S, Covault JA, Fildani A, Walsh JP. 2016. Environmental signal propagation in sedimentary systems across timescales. Earth-Science Reviews 153: 7-29.

Ruth RH, Yoder RA. 1953. Reducing wind damage in the forests of the Oregon Coast Range. US Department of Agriculture, Forest Service, Pacific Northwest Old Series Research Paper No.7. Portland, Oregon. 30 pp.

Schiefer E, Gilbert R, Hassan MA, 2011. A lake sediment-based proxy of floods in the Rocky Mountain Front Ranges, Canada. Journal of Paleolimnology 45: 137-149.

Schillereff DN, Chiverrell RC, Macdonald N, Hooke JM. 2014. Flood stratigraphies in lake sediments: A Review. Earth-Science Reviews 135: 17-37.

Schillereff DN, Chiverrell RC, Macdonald N, Hooke JM. 2016. Hydrologic thresholds and basin control over paleoflood records in lakes. Geology 44: 43-46.

Schuytema GS, Shankland RD. 1976. Effects of Log Handling and Storage on Water Quality. US Environmental Protection Agency. Environmental Protection Technology Series EPA-600/2-76-262. Cincinnati, Ohio. 86 pp.

Shephard FP. 1954. Nomenclature based on sand-silt-clay ratios. Journal of Sedimentary Research 24: 151-158.

Sims RO. 1998. Loon Lake and Ash Valley Revisited: A History of Ash Valley and Loon Lake in Douglas County, Oregon. Self-published.

Snyder K, Sullivan T, Moore D, Raymond R. 2006. Mill Creek Watershed Assessment. Prepared by E&S Environmental Chemistry, Inc. for the Umpqua Basin Watershed Council. Roseburg, Oregon. 138 pp.

Sommerfield CK, Drake DE, Wheatcroft RA. 2002. Shelf record of climatic changes in flood magnitude and frequency, north-coastal California. Geology 30: 395-398.

Sperazza M, Moore JN, Hendrix MS. 2004. High-resolution particle size analysis of naturally occurring very fine-grained sediment through laser diffractometry. Journal of Sedimentary Research 74: 736-743.

St-Onge G, Mulder T, Piper DJW, Hillaire-Marcel C, Stoner JS. 2004. Earthquake and flood-induced turbidites in the Saguenay Fjord (Québec): a Holocene paleoseismicity record. Quaternary Science Reviews 23: 283-294.

Swanson FJ. 1981. Fire and geomorphic processes. In Proceedings, Fire Regimes and Ecosystems Conference. US Department of Agriculture, Forest Service, General Technical Report WO-26, Honolulu, Hawaii: 401-420.

Telford RJ, Heegaard E, Birks HJB. 2004. The intercept is a poor estimate of a calibrated radiocarbon age. The Holocene 14: 296-98.

USACE. 2000. Water Resources Development in Oregon 2000. US Army Corp of Engineers, Portland District. 96 pp.

USDI. 2005. Mill Creek-Lower Umpqua River Watershed Analysis. US Department of Interior, Coos Bay District, Umpqua Resource Area – Bureau of Land Management. 233 pp.

USGS. 1982. United States Geological Survey. Guidelines for Determining Flood Frequency Analysis. Bulletin #17B of the Hydrology Subcommittee. 194 pp.

USGS. 2012. United States Geological Survey. Shakemap scenario. Accessed from http://earthquake.usgs.gov/earthquakes/shakemap/global/shake/Casc9.0_se/

USGS. 2013. United States Geological Survey. Surface-Water Data for the Nation. Accessed from http://waterdata.usgs.gov/nwis/sw

Voth EH. 1968. Food habits of the Pacific Mountain Beaver, *Aplodontia rufa pacifica* Merriam. PhD thesis. Corvallis, Oregon State University. 263 pp.

Wallick JR, O'Connor JE, Anderson S, Keith M, Cannon C, Risley JC. 2011. Channel change and bed-material transport in the Umpqua River basin, Oregon. US Geological Survey Scientific Investigations Report, 2011–5041. 112 pp.

Warrick JA, Hatten JA, Pasternack GB, Gray AB, Goni MA, Wheatcroft RA. The effects of wildfire on the sediment yield of a coastal California watershed. Geological Society of America Bulletin 124: 1130-1146.

Wetzel RG. 2001. Limnology: Lake and River Ecosystems, 3rd edition. Academic Press: San Diego

Wheatcroft RA. 1990. Preservation potential of sedimentary event layers. Geology 18: 843-845.

Wheatcroft RA, Sommerfield CK. 2005. River sediment flux and shelf sediment accumulation rates on the Pacific Northwest margin. Continental Shelf Research 25: 311-332.

Wheatcroft RA, Goni MA, Richardson KN, Borgeld JC. 2013. Natural and human impacts on centennial sediment accumulation patterns on the Umpqua River margin, Oregon. Marine Geology 339: 44-56.

Witter RC, Zhang YL, Wang KL, Goldfinger C, Priest GR, Allan JC. 2012. Coseismic slip on the southern Cascadia megathrust implied by tsunami deposits in an Oregon lake and earthquake-triggered marine turbidites. Journal of Geophysical Research-Solid Earth 117: B10303.

Whitlock C, Dean W, Rosenbaum J, Stevens L, Fritz S, Bracht B, Power M. 2008. A 2650-year-long record of environmental change from northern Yellowstone National Park based on a comparison of multiple proxy data. Quaternary International 188: 126-138.

Wilhelm B, Arnaud F, Sabatier P, Crouzet C, Brisset E, Chaumillon E, Disnar J, et al. 2012. 1400 years of extreme precipitation patterns over the Mediterranean French Alps and possible forcing mechanisms. Quaternary Research 78: 1-12.

Zolitschka B, Mingram J, Van Der Gaast S, Jansen JHF, Naumann R. 2001. Sediment logging techniques. In Tracking Environmental Change Using Lake Sediments. Volume 1: Basin Analysis, Coring, and Chronological Techniques, Last WM, Smol JP (eds). Kluwer Academic Publishers: Dordrecht; 137-153.

Zolitschka B, Francus P, Ojala AEK, Schimmelmann A. 2015. Varves in lake sediments – a review. Quaternary Science Reviews 117: 1-41.

Zybach B. 2003. The Great Fires: Indian burning and catastrophic forest fire patterns of the Oregon Coast Range, 1491-1951. PhD dissertation. Corvallis, Oregon State University. 475 pp.

APPENDICES

A1. History of the catchment

Where Loon Lake's waters join the Umpqua R., the effects of tidewater are felt. The proximity to the ocean influenced the area's early settlement history. In the mid 1800's, a lumber mill stood here beneath the sandstone cliffs guarding the mouth of Mill Creek (Snyder et al., 2006). Processed trees harvested from the forests above – western hemlock (*Tsuga heterophylla*), Douglas-fir (*Pseudotsuga menziesii*), and western red cedar (*Thuja plicata*) - would be moved from here to ships at nearby port towns, waiting to brave the ocean journey south (Daily Alta, 1891). Making logs out of the great forests of the Coast Range was booming all around, including tributaries to Mill Creek below Loon Lake, where splash dams would hasten the passage of trees down creeks from mountain slopes to market (Miller, 2010). In a sort of irony, the steep mountainsides in upper Mill Creek valley (below the impassable sandstone-rubble landslide that holds back the waters of Loon Lake and creates a cascade flowing from the lake) had kept it and its uplake tributaries isolated from the 19th century timber rush.

Hidden from the world, except by a long day's circuitous journey on foot or horse through nearby watersheds and over ridges from the northeast (Sims, 1998), a small community next to Loon Lake named Ash (Ash Valley), developed. Homesteaders began settling in the 1870's (GLO, 1874; Table A1), clearing the land and draining parcels of the wet, flat-bottomed 9-mile long alluvial valley at the head of the lake (Figure 2d). The flat was converted to pasture for agriculture (Jones and Stearns, 1928), which set the stage for a dairy to open in 1917 (Sims, 1998). Soon after, a county road connected the Umpqua River to the lake (Snyder et al., 2006), traversing the mountainside in upper Mill Creek and bypassing the sandstone-boulder falls. This opened the catchment to standard forest harvesting (Phillips, pers. com., 2015).

Loon Lake catchment was heavily impacted by timber harvest and associated road building in the 20th and 21st centuries, with immediate and delayed impacts to the lake. Although timber was being harvested some around the lake early in the century (USDI, 2005), it did not begin in earnest until the 1940's. From then until the 1950's, trees harvested in the upper catchment were dumped into the lake and rafted down to the distal end instead of by road

because the bridge over the outlet falls was inadequate (USDI, 2005; Phillips, 2015, pers. com.). Once the logs reached the north end of the lake, they could be hauled out and trucked down to the Umpqua River. This storage of logs left debris in the lake, and stained water brown, probably having an effect on water quality, and may have contributed to the preservation of layers in the sediment (Appendix A4.5).

Roadbuilding and harvest accelerated in the Elliott State Forest (NW portion of the catchment) in the 1950's-1960's, including salvage of timber after large windstorms in 1951 and the 1962 Columbus Day windstorm (Ruth and Yoder, 1953; Orr, 1963; Biosystems, 2003). This occurred on state as well as on private and BLM land (USDI, 2005). In the mid-1960's, there was a sharp increase in timber harvest by the largest landowner, Weyerhauser, an industrial private (IP) timber company who owns ~70% of the catchment and ~98% of the private land (Figure 2a), followed by a continued increase in harvested area on their land into the 1970's. By 1971, about 20% of the catchment had been harvested, ~12% by Weyerhauser (Reiter, 2015, personal com.; grey line in Figure A1), much of the Elliott State Forest ownership (about 7% of the catchment; not shown in Figure A1) as forests were finally ready to be harvested following fire in 1868 (Phillips, 2015, pers. com.), plus much of the BLM land (18% of the catchment; USDI, 2005; not shown on Figure A1. Annual harvesting rate remained above 1960 levels until late 1980's, when it suddenly waned for a decade before quickly returning to ~two-thirds of peak levels (Figure A1). Vegetation change detection techniques using satellite remote sensing (Landsat) available beginning 1972 show that ~50% of the entire Loon Lake catchment was harvested during the years 1972-2012 (Figure 2c; Appendix A2; Cohen et al., 2002; Kennedy et al., 2012).

Previous work at Loon Lake reveals important information about its formation, the age of the lake, the physical limnology, and its catchment. One study compared Loon Lake to other landslide-dammed lakes within the OCR marine sandstone lithology, and estimated the fill volume and other features of the Loon Lake dam (Lane, 1987). Two studies sampled the lake sediment. The first took an Ekman sample of the surface and measured the thickness of the alternating

black and medium gray to tan layers, estimating a sedimentation rate of 1 cm y^{-1} if the layers were annually deposited (Dean and Bradbury, 1993). The goal of this study was to find PNW lakes which would provide information on paleoclimate, and Loon Lake was not selected for further research. The second sediment study measured pollen in surface samples in this and tens of PNW lakes to study Holocene vegetation changes (Minckley and Whitlock, 2000). They found that in addition to conifers, the hardwood red alder (*Alnus rubra*) is also a dominant tree species in this catchment. The USGS measured water quality parameters in this and other Coast Range and coastal lakes (Curtiss et al.,1984). They found that Loon Lake develops a strong thermocline in the summer and has a seasonal oxygen deficit at depth. They noted a single mixing of the water column during the year (winter), indicating that Loon Lake is a warm monomictic lake. Finally, every curious person wants to know how old the lake is. In the early 1960's, a motivated resident writer and music teacher of Ash Valley, Harriet Ward, obtained a sample of wood from a submerged tree in the lake, and submitted it for radiocarbon dating. The result was a conventional ^{14}C date of 1460 +/- 80 y BP (Fergusson and Libby, 1962). This has been widely assumed to be the age of the lake. However, the ^{14}C dating in this research suggests that the age of the lake may be older (Sections 4.1.2 and 4.4).

Table A1. List of catchment events since 1700 AD. These may have contributed sediment to Loon Lake, or contribute to an understanding of sedimentation at Loon Lake. [1]Leonard et al., 2010; [2]ODF, 2011; [3]Phillips J, 2015; [4]Biosystems, 2003; [5]Douglas Co., 2009; [6]Sims, 1998; [7]USGS, 2013; [8]Snyder et al., 2006; [9]USDI, 2005; [10]USACE, 2000; [11]Jones and Stearns, 1928.

Year (AD)	Catchment event
1700	Cascadia subduction zone earthquake[1]
1765	Forest fire – east side of catchment[2,3]
1861	Flood reported regionally[4]
1868	Forest fire – "Coos Bay Fire" – west side of catchment[2,3]
1890	Flood reported regionally[4]
~1900	Old lakebed (Ash Valley) cultivated for hay[6]
1907-1917	Mill Cr. discharge gaging station operating[7,11]
1909	Flood reported regionally; highest Mill Cr. discharge recorded[5,7]
1917	Dairy opens in Ash Valley[6], logging of upper subwatersheds[6]
~1920	County road built up Mill Cr. to Loon Lake from Umpqua R. [8]
1940's	Loon Lake used as log storage pond[3,6,9]; U.S. Army Corp of Engineers widens lake outlet (1948) [6,9,10]
1950's	Increase in intensive logging and road building[6,8]; lake continued to be used as log storage pond until 1950's[3,9]
1962	Windstorm – "Columbus Day Storm" [4]
1964	Flood – residents report flooding in structures at Loon Lake[6]
1972	Forest Practice Rules implemented after Oregon Forest Practices Act
1981	Flood – residents report flooding in structures at Loon Lake[6]
1994	Forest practice water protection rules enhanced after SB1125[11]
1996	Flood – residents report flooding in structures at Loon Lake[6]

A2. Harvest and remotely-sensed data analysis

The quantified data presented in this research are a partial representation of the spatial and temporal extent of timber harvest in Loon Lake catchment. The results are limited to three sources: two remotely-sensed data sets (Landsat) of forest disturbance in the Pacific Northwest U.S.A. and a third data set from the largest industrial private timber (IP) landowner in the catchment. First, the two Landsat data sets are processed and georectified Landsat satellite imagery, one annually from 1985 to 2012 (Kennedy et al., 2012) and the other in larger time bins from 1972 to 1995 (Cohen et al., 2002). ArcMap GIS software (Environmental Systems Research Institute, 1998) was used to calculate area harvested cumulatively and annually in the catchment. Figure 2c shows the cumulative result for Landsat-derived area harvested from 1972 to 2012, which is 50% of the catchment during this period. Second, the IP company provided area of planting (birth) year of trees regenerating following timber harvest on their ownership in the catchment (~70% of catchment land base) for 1943 to 2014. This was converted to area harvested of the whole catchment and set one year forward for a one year lag growth following harvest.

Figure A1 shows the IP data (grey line) and the Kennedy et al. (2012) data (black line), combined here because of the annual time step for each. The two data sets here correlate well, although the Landsat data shows more area harvested during many years. Because the satellite data includes the whole catchment, not just IP's ownership, this is an expected result. (Note that for four years Landsat data rate is less than IP rate. This may be due to error in measurements or in subsequent calculations.) It should therefore be expected that if the Landsat data could extend back to 1943, i.e., have data for the whole catchment back to 1943, harvest would be greater than the IP rates, especially much higher for pre-1964 when IP timber harvest was very low and State and BLM harvest was high. This difference is not quantified here and is absent in Figure A1, so it is only a partial data set. Additionally, neither the intensity of land disturbance nor type of harvest is indicated in the data. Therefore, the data is used for discussion purposes only.

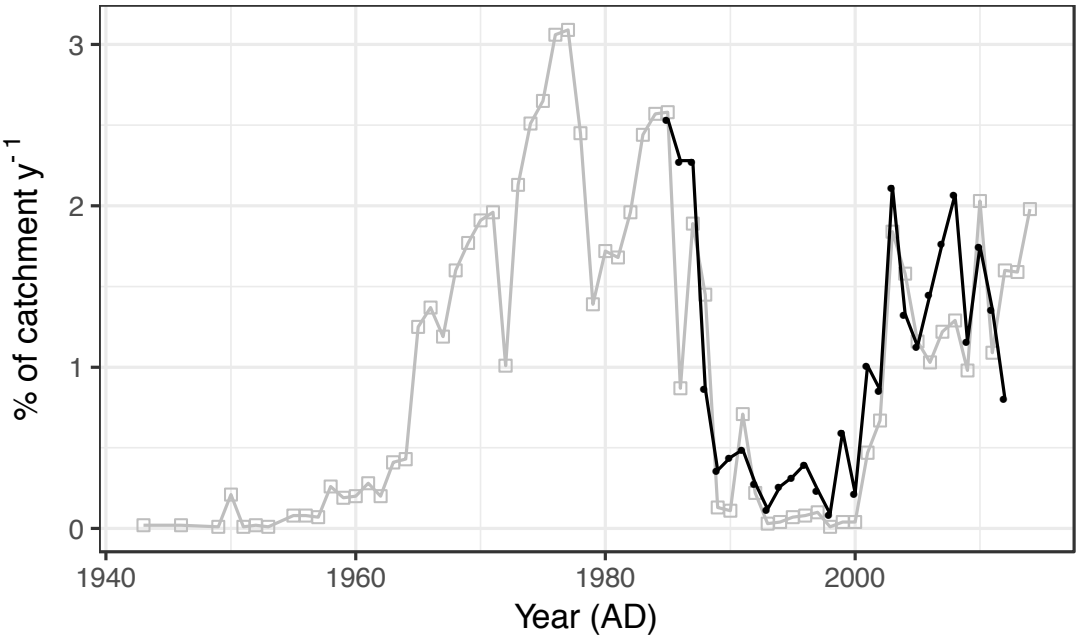

Figure A1. Total and partial percent of catchment harvested from 1943 to 2014. Black line with filled circles is satellite-derived *total* percent of catchment from 1985 to 2012. Grey line with square hollow points is *partial* percent of the total catchment which was harvested each y from 1943-2014 only by the largest private landowner (70% ownership of the catchment).

A3. Cores and coring

Twenty cores of three different types were collected in 2013 (Table 1). In April, six 5-cm diameter gravity cores of lengths up to 0.5 m in clear plastic tubes were collected with a Wildco K-B corer, initially for reconnaissance purposes. To obtain larger diameter cores with deeper sediment penetration, two methods were employed. In July, the Wildco K-B corer was modified and amount of weight increased to obtain one 10.1-cm inner diameter (ID) core. In September, a marine-application trigger core head mounted with significant weight allowed successful collection of nine more 10.1-cm ID cores in white PVC tubes, ranging in length from 0.41 m to 1.92 m. Finally, to facilitate collection of long cores also in September, a Nesje percussion-piston corer from LacCore at University of Minnesota was used, recovering three 7.34-cm ID aluminum-lined cores of length 4.30, 6.26, and 7.03 m. Coring in April and July was conducted from a davit off a 15-foot motor boat, and in September from a 4-point anchored barge-like platform previously constructed by the University of Washington (Ritchie and Bourgeois, 2010). This square platform consists of two 6.3 m-long connected pontoons with a “moon hole” in the center through which coring apparatus can be passed. Four metal poles bolted to the platform form an 8-m A-frame tower from which a pulley supports coring apparatus above the moon hole. A hydraulic winch provided power.

The specific location of coring was determined by consulting available and measured bathymetry of the lake. The reconnaissance cores were taken uplake and downlake of a large tributary (Salander Creek) and in the deepest basin, as identified in an existing bathymetric map (Figure 2b). On this same day, soundings were taken, which confirmed location and depth of the deepest basin, and added detail to the bathymetric map. Additionally, temperature and dissolved oxygen profiles were taken with a Cast-Away CTD and YSI Multi-Sonde to assess whether a thermocline had developed in the water column, and to measure the amount of dissolved oxygen (DO) present at depth. Our DO and temperature findings agree with those presented in Curtiss et al. (1984). With this added bathymetric detail, in July and September, cores were taken in a

longitudinal transect down the approximate center line of the lake, with several other cores concentrated at the deepest basin (Figure 2b; Table 1, Figure A3).

Upon recovery of each core or before MSCL measurements, excess liner materials were usually cut off near the sediment-water interface (SWI), excess water was carefully siphoned off, rigid foam was fit into any remaining gap at the top, and the liners were then capped, taped, and labeled, and then refrigerated.

Figure A2. Photo of Loon Lake sediment varves. View is of varves in the top several centimeters of a reconnaissance core, alternating olive gray and thinner brown and black.

Figure A3. Center slices of x-radiographs of thirteen sediment cores. Cores are shown from distal (left) to proximal (right). Differing heights at core tops show relative depth of the lake bottom where each core was taken. Six (6) events are correlated across cores (E1, E2, E5-E8). Solid correlation lines indicate visually apparent correlation, whereas dashed lines indicate assumed or uncertain visual correlations. Inset shows bathymetry of Loon Lake (adapted from adapted from Rinella, 1979 and Curtiss et al., 1984) and colored shapes within lake shows coring locations, which match the color and shape indicated with the core names at the tops of the cores. Hollow circle markers show location of reconnaissance coring (x-radiographs of these not shown). Correlation in two of the three longest cores, 02aN and 02bN, are continued in Figure 3. See Figure 2b for more detail on the coring locations of the most-used cores for analyses. Inner diameters of the two different types of cores are shown on left-most two cores: 10.1-cm gravity cores and longer 7.3-cm Nesje percussion piston cores. Height scale for all cores is left of Core 02aN, to sediment-water interface (SWI).

Figure A3.

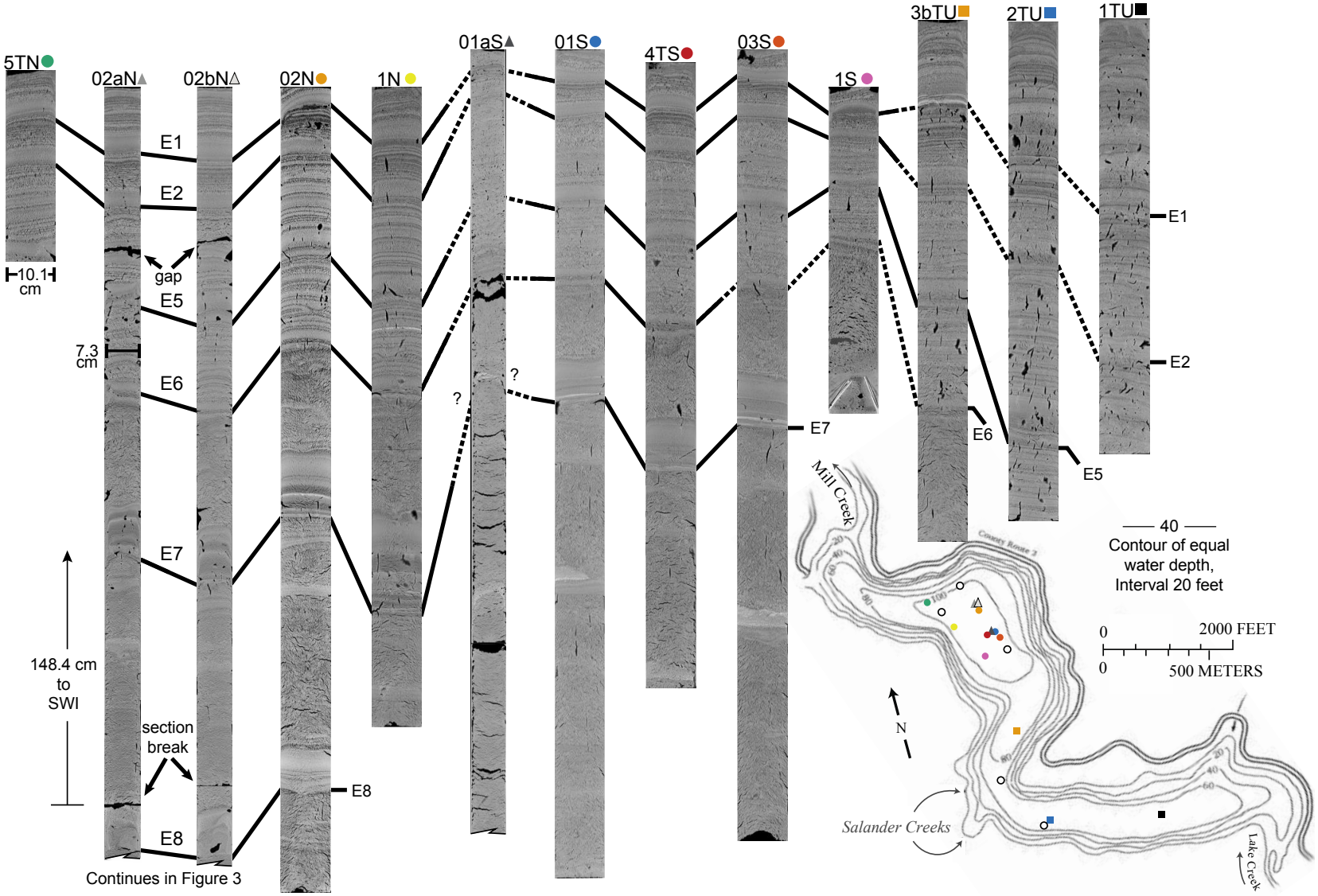
5TN
02aN
02bN
02N
1N
01aS
01S
4TS
03S
1S
3bTU
2TU
1TU
E1
E2
gap
E5
E6
E7
E8
10.1 cm
7.3 cm
148.4 cm to SWI
section break
Continues in Figure 3
?
?
E1
E2
E5
E6
E7
Mill Creek
County Route 1
40
Contour of equal water depth, Interval 20 feet
0
2000 FEET
0
500 METERS
N
Salander Creeks
Lake Creek

Figure A4. Whole-core grain size and geochemistry, photo, and stratigraphic units. Parameters included are dry bulk density, C:N (atomic), % total nitrogen, % total carbon, % clay, and median grain size (D_{50}). The sedimentary column is split into two halves: 0-340 cm and 340-694 cm in MSCL depth scale. Below the six parameters is the length scale in cm according to the MSCL depth, which is correlated with the photograph of the core. The stratigraphic unit cartoon (legend below) is correlated with the x-radiograph. D_{50} of event bed E21 spikes to 231 μm, and is shown rising above all other parameter plots. Buttons visible in the core photograph are misplaced below the top section at 143 cm, therefore use the MSCL depth scale.

Figure A4.

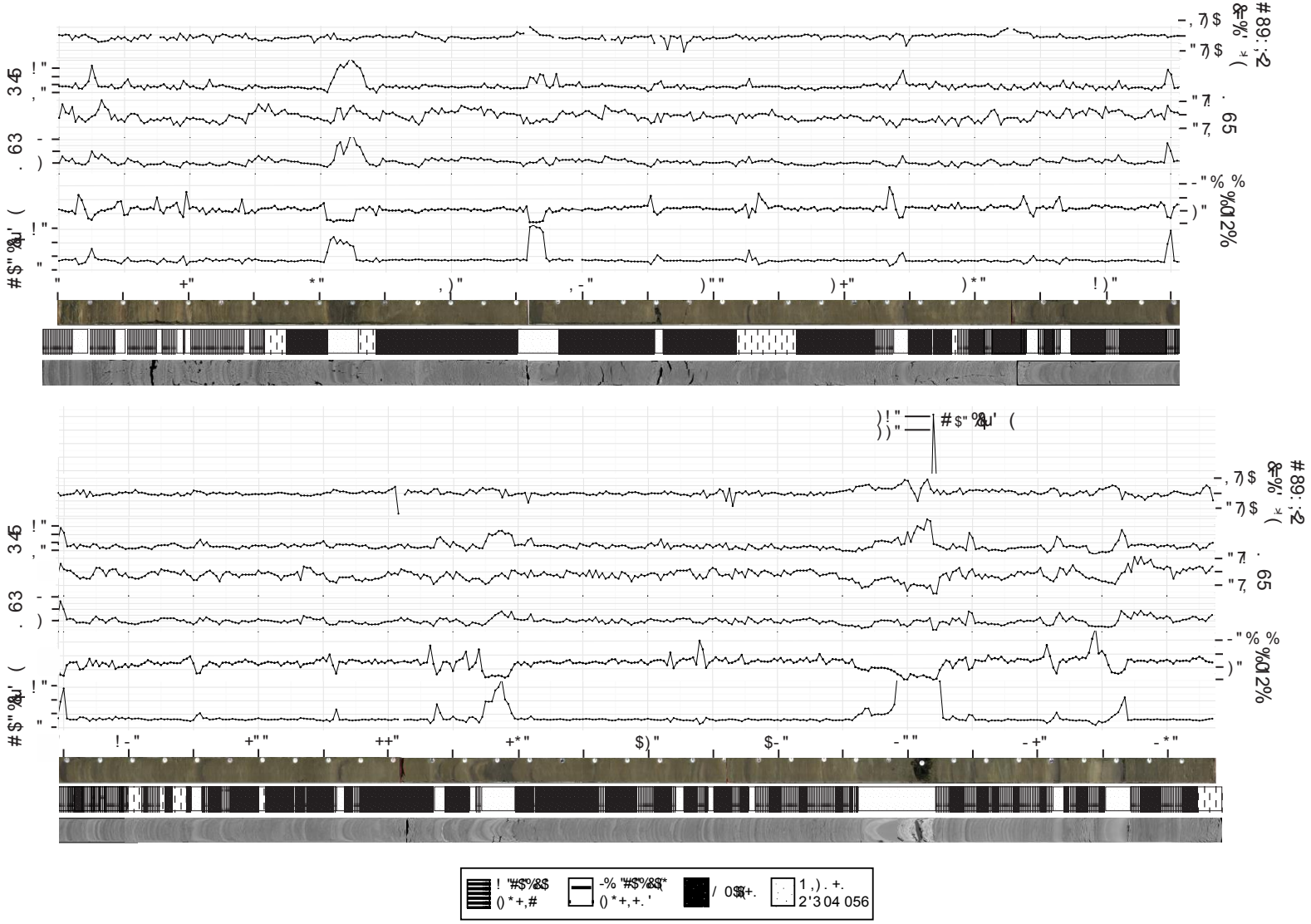

A4. Sediment analysis

A4.1. Non-destructive techniques

Cores were scanned with X-ray computed tomography (X-ray CT) at the OSU School of Veterinary Medicine. A DICOM viewer and image processing software (Osirix and IPLab) was utilized to view x-radiographs Thicknesses of laminae through core 02aN were measured manually with IPLab on the center coronal slice, with each vertical measurement taken as near the middle of the center slice as possible.

For the Multi-Sensor Core Logger (MSCL), the gamma-ray source is ^{137}Cs, and the calibration of gamma density of the cores was done according to standard methods (Geotek, 2015), with each liner type (PVC or aluminum) requiring a different calibration set-up. The measurements occurred at 1 cm intervals with 10 s sensor time per measurement. The wet bulk density measurement was used to convert linear accumulation of sediment to mass accumulation and to correct for in-situ and post-coring compaction as follows. Porosity was estimated from the wet bulk density assuming density of water (ρ_{water}) and grain density (ρ_{grain}) of 1 g/cm^3 and 2.65 g/cm^3, respectively (Dadey et al., 1992). Mass (g cm^{-2}) for every layer measured in the core was calculated as the product of the thickness of the layer (cm) and the dry bulk density (g cm^{-3}) of the 1-cm interval to which the layer belonged. Accumulated mass (g cm^{-2}) in the core is the accumulated sum of mass through the core.

Magnetic susceptibility (MS) was measured with a Bartington loop sensor on the MSCL track at 0.5 cm intervals with 10 s measurement time and measured only on the plastic-lined cores because of sensor interference by the aluminum liner. All large gravity cores were also measured with a point-MS sensor at 0.5 cm intervals on a line scan track (Zolitschka et al., 2001). After splitting and describing the cores as described in the text (Section 2.3.1), split cores were wrapped with plastic film, placed in plastic tubes, and stored at 3°C at the MGR.

A4.2. Destructive sampling

For grain size and elemental analysis, bulk sediment samples were removed in 1-cm intervals from the center of the work half of split cores 02aN and selected areas in 02bN and 02N. Approximately 6 g of sediment was removed from the surface of the split core for grain size analysis, and 4-6 g was removed from the same depth increment beneath the grain size sample for C/N analysis, thereby avoiding oxidized sediment for the elemental analysis. For higher resolution grain size data within thick graded beds, 0.25-cm and 0.5-cm sediment samples were taken in several such beds in cores 02aN and 02N.

A4.3. Grain size analysis

Grain size was measured for each 1 cm interval sample or higher resolution in core 02aN. Each ~6 g sample was placed in a 50-ml plastic centrifuge vial and refrigerated before undergoing treatment to remove organic material. This digestion process alternates cycles of unheated and heated (< 70° C in a water bath) treatment of the sediment with 30% hydrogen peroxide, centrifuging, and decanting, over four days (Gray et al., 2010). The lithic portion was then set in a dispersion solution of sodium hexametaphosphate for ≥ 24 hours before being introduced to the 2000 Malvern Mastersizer at the National Energy Technology Laboratory (Department of Energy) in Albany, Oregon by methods described in Sperazza et al. (2004). This instrument uses sonication to disperse grains and laser diffractometry to detect forward scattering of light off grains. It then models grain size under Mei light diffraction theory.

A4.4. Geochemistry

To examine the relationship of the TC from acidified and unacidified samples, several samples (n=30) representative of the different stratigraphic units in the core were acidified by vapor phase according to methods in Hedges and Stern (1984), and processed in the EA as described in the text. The outlier in the TC-TOC results was a sample from the sand layer of E21.

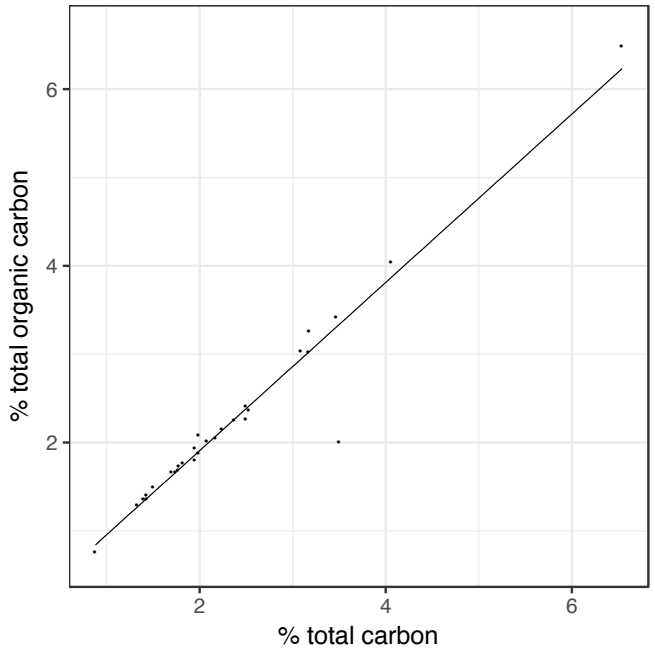

Figure A5. Results of vapor phase acidification test. Twenty-nine sediment samples of known total carbon content (%TC) were acidified to measure total organic carbon (%TOC).

A4.5. Preservation of stratigraphy in varved section (0-67 cm)

Apparently, conditions were such in the lake at certain times that layers were preserved. In particular, in the contemporary period, varves are coincident with human activities at the lake. When the lake was used as a log pond in the 1940's and early 1950's, it was reported that the color of the water was brown (Phillips, per. com. 2015) and swimmers would be stained (Sims, 1998). This suggests that leachate, probably tannins or other stable organic acids from wood and bark, were present the lake (Blanton, 1970). The colored water would have decreased light penetration, and inhibited photosynthesis by phytoplankton at depth (Schuytema and Shankland, 1976). Decomposition of bark and particulate organic carbon by heterotrophic activity increases biological oxygen demand in the water column, leading to consumption of dissolved oxygen (Curtiss et al., 1984; Ho and Ching-Yan, 1987). The hypolimnion would become hypoxic or anoxic and bioturbation would diminish. In this way, the low oxygen conditions would have led to layer

preservation (Francus et al., 2008). In Lake Washington, the sediments themselves were anoxic below 4 cm, which minimized bioturbation, although the water column itself was not anoxic (Kuivila and Murray, 1984), and this condition was attributed to preservation of layers (Karlin and Abella, 1992). Measurements of dissolved oxygen at Loon Lake later last century showed dissolved oxygen to be very low (< 2 mg l^{-1}) in the hypolimnion during water column stratification (Curtiss et al., 1984; Section 2.1). With development around the lake including septic systems, this is an indication of cultural eutrophication (O'Sullivan, 1983).

A5. Hydroclimate

Winter storms often result in flooding of streams and rivers, sometimes because of rain-on-snow events. Memorable years of historical regional floods are 1861, 1890, 1909, 1945, 1955, 1964, 1974, 1982, 1996/97, and 2005/6 (e.g. Oregonian, 1890; Eilers et al., 1996; Douglas Co., 2009; Wallick et al., 2011; USGS, 2013; Table A1), and others - 1896, 1953, and 1954 - more localized on the nearby coast (Snyder et al., 2006). After at least three of the most recent storms, 1964, 1982, and 1996, residents at Loon Lake reported that the lake level was elevated and had flooded structures. Apparently flooding in the valley above the lake had been an issue prior to this, as the U.S. Army Corp of Engineers widened the outlet of Loon Lake by blasting in 1948, under the 1941 Flood Control Act (USACE, 2000; USDI, 2005). Despite the wet, cool winters, western Oregon is warm and dry during the summer. The 30-y normal average maximum August temperature is 29.4 ºC.

Monthly peak discharge and annual peak discharge at Mill Creek gage from 1908-1914 (7 years) were regressed on the same hydrologic variables from the Elkton discharge (Q) gaging station (Figure A6). For monthly peak Q, a very strong positive monotonic relationship is shown between the two stations (r_s = 0.96, p = 0.000). Monthly peak Q was identified as the highest daily mean Q during each month of the seven years and 5 months of operation (n=89). Not as strong as monthly peak, a positive relationship is demonstrated for seven years of annual peak discharge (r_s = 0.80, p = 0.029). Both were correlated with Spearman's rank and tested for significance with permutation methods (R-package 'pvrank'; Amerise et al., 2016).

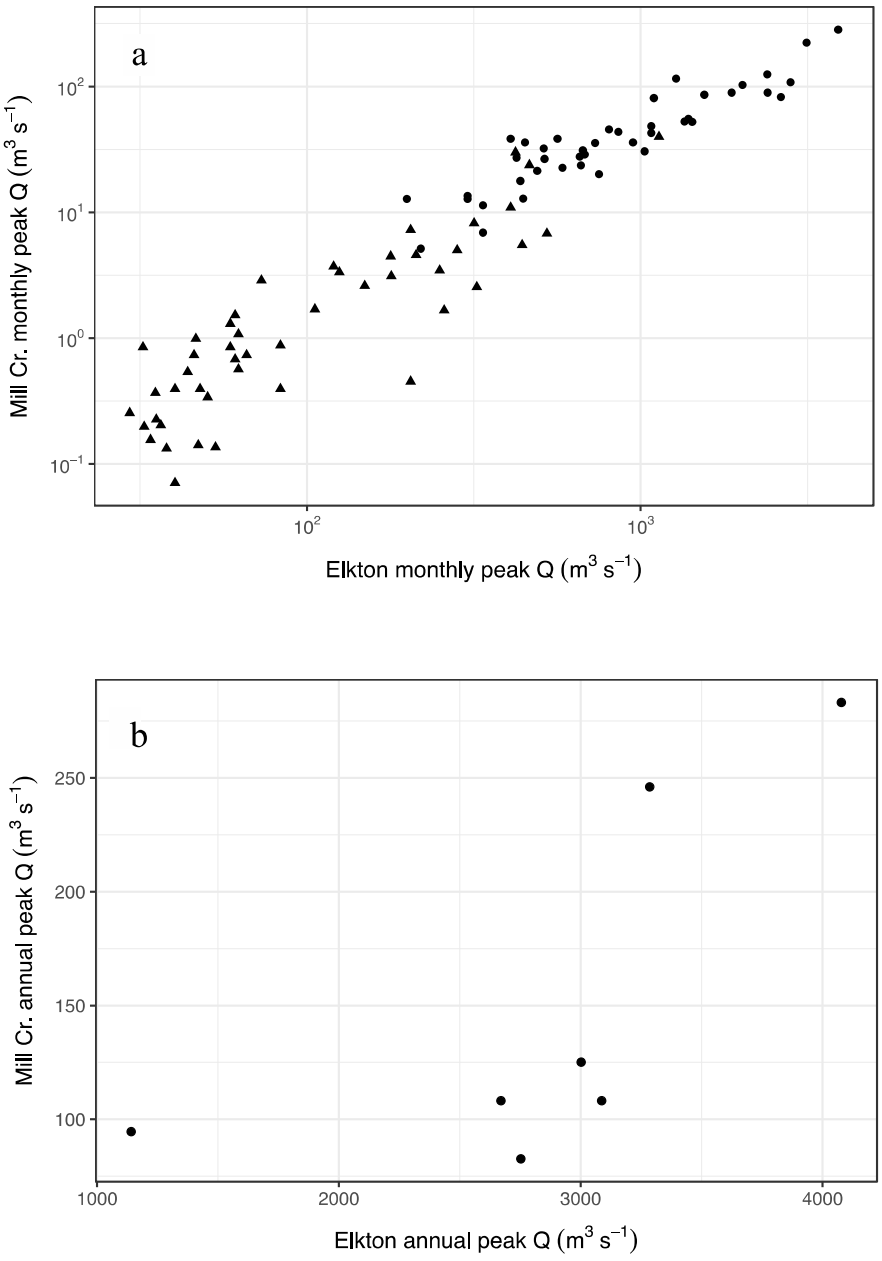

Figure A6. Bivariate plots of water discharge at Elkton and Mill Cr. Discharge is from 1908-1917 on Mill Creek and on Umpqua River near Elkton. Mill Creek gaging station (USGS #14323000) is downstream of Loon Lake and was operational for seven complete water years during this time. Elkton gaging station (USGS #14321000) is ~20 km east of Loon Lake on the Umpqua R. (Figure 1). a) Monthly peak discharge b) Annual peak discharge.

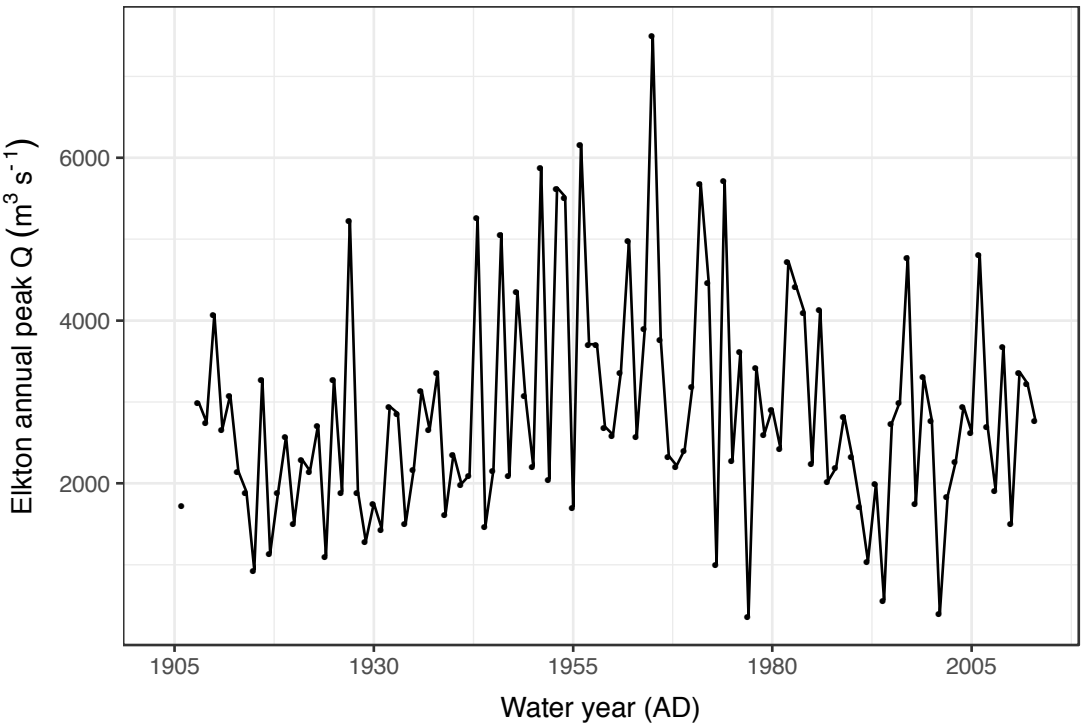

Figure A7. Annual peak discharge on the Umpqua R. at Elkton. For this station (USGS #14321000), this is the period of record, WY 1906-2013. Cool-wet phase of the PDO is shaded gray.

A6. Chronology and accumulation rate analysis

A6.1. Early period - radiocarbon dating

Targeted layers were those in which material had been identified when describing the split cores, as well as within layer types which seemed to yield the most and highest quality material, such as homogeneous layers at the bases of graded beds. Beside these layers, material for two samples came from different locations in the sand layer, one 3 cm up from the bottom of the bed, and the other near the top of the debris-laden portion. Three samples came from indistinct layered and mottled sections.

Only materials with a rapid decomposition rate (e.g. leaves and thin twigs) were collected so as to increase the probability that the year of deposition was as close to the ^{14}C age as possible (Howarth et al., 2013). In several cases, adjacent 1-cm intervals needed to be combined to accumulate enough sample mass, in one case up to 4 cm. Useable material in the Loon Lake cores consisted primarily of coniferous (Douglas-fir; *Pseudotsuga menziesii)* and deciduous/broadleaf leaf fragments and occasional other parts of these plants.

To find this material, each sliced interval was added to deionized water and sonicated in a glass beaker in a water bath for 10 – 30 minutes to break sediment aggregates and loosen organic matter from sediment, then passed through 125-µm and 1-mm sieves to collect plant material. Once identified under a dissecting scope, useable material was thoroughly cleaned with deionized water and small tools.

The samples and a dead wood standard (C5) provided by National Ocean Science Accelerator Mass Spectrometry Facility (NOSAMS) were chemically treated with an acid-alkali-acid wash (Olsson, 1986; Björck and Wohlfarth, 2001). 11 samples and the standard were placed in clean glass jars, loosely capped, and dried overnight in a 50° C oven. Samples were then sent to NOSAMS, including one small-mass sample processed according to methods described in Gagnon et al. (2000).

As stated in Section 2.3.5., the resulting ^{14}C dates (Table 6) were calibrated with Oxcal program v4.2.4 (Bronk Ramsey, 2009) with the IntCal13 atmospheric curve data set (Reimer et al., 2013), resulting in likelihood probability distributions. Oxcal uses Bayesian analysis, Markov-Chain Monte Carlo (MCMC) resampling, and Poisson modeling to calculate marginal posterior densities (Enkin et al., 2013). The following inputs were incorporated: a random deposition model (P-sequence), a variable rigidity function of deposition, allowing for different event sizes (U(-1.35,1.35) and default of k=1, an outlier model which is used to identify samples which may be stratigraphically misplaced (T-simple), and a probability of outliers of 0.05 (Bronk Ramsey et al., 2010).

Outlier analysis identified three samples as outliers. Their ^{14}C and calibrated ages were out of stratigraphic order in, and too old for their stratigraphic depth. LL1, LL3, and LL9 were found in three different stratigraphic units: at the base of an event bed, in a mottled region, and at the top of the sand and woody debris layer, respectively. These dated samples were removed from the remainder of the analysis. In the case of several samples which had combined 1-cm intervals, a weighted mid-point of depth was used. The equivalent CT-depth for all samples was used as input to Oxcal.

Analyzing the likelihood probability distributions with a deposition model in Oxcal resulted in modeled posterior distributions and an initial age-depth model (Figure A8). During this process, it was desirable to constrain the tri-modal likelihood probability distribution of the top sample, LL2, to certain age ranges when prior information allowed reasonable assumptions. In the modeling process, one parameter was constrained by placing an upper boundary at 67 cm, which is the bottom of the most recent laminated region, with an age range of 1939 ± 2 y AD accounting for varve counting error, based on the contemporary age control findings. In the model, this constraint eliminated the most recent mode of the distribution (far right) of sample LL2, shown in light gray in Figure A9. A very high MAR after this sample would have resulted if the actual date of this layer resided within its far-right distribution range. It is assumed that this is an unrealistic MAR.

As described in Sections 2.3.5. and 3.2.2., twenty-three event beds were removed to find a background sedimentation rate (Table 4; Table 8). Details here explain how the criteria were used. The clay threshold was determined by observing that several graded layers in the recent period have clay drapes of 34% clay and higher, which is the 95th percentile of percent clay in the top 350 cm of the core. This same percentile was applied to the bottom 350 cm of the core, which overall has a higher clay content. The resulting threshold for the bottom is a 38% clay drape. Event beds 8 and 21 both had lower clay drape content than 34% or 38% respectively, but were still included in the 23 removed beds because they are visually identifiable as events, and have plausible explanations for their low clay content drape. The upper event is at a section boundary and had lost part of its stratigraphy during core cutting. Stratigraphic correlation in Cores 02N and 02bN show a measured content clay drape of 42% and 38%, respectively. The lower event, E21, has a sustained high sand and silt content throughout. It could be that these two size fractions simply overwhelmed particle size distribution of sediment in the water column, and ultimately deposition. Therefore, it has a weak clay cap.

A sediment and mass accumulation rate was calculated for the ^{14}C period with the marginal posterior densities (probability distributions), as described in the text. On the occasion that a draw included sampling from the distributions and were not in stratigraphically order (specifically at samples LL8 and LL10 whose distributions overlap; Figures A8 and A10) this draw was discarded. Resampling in this manner continued until 5000 stratigraphically-correct draws and resulting estimated rates were accrued. A script for this MC approach of resampling and removed incorrect draws was written by university staff and the author with the statistics program R (Figure A13). A mass-age model was built using the resulting MAR (Figure A10), as described in the text (Section 3.2).

Figure A8. Age-depth model output from Oxcal. 68%, 95%, and 98% interpolated ranges are drawn between the marginal posterior densities. At each calibrated sample, the light gray distribution is the unmodeled likelihood probability distribution, and the darkened distribution is the posterior probability distribution. Oxcal v4.2.4 (Bronk Ramsey, 2013), based on the IntCal atmospheric curve (Reimer et al., 2013).

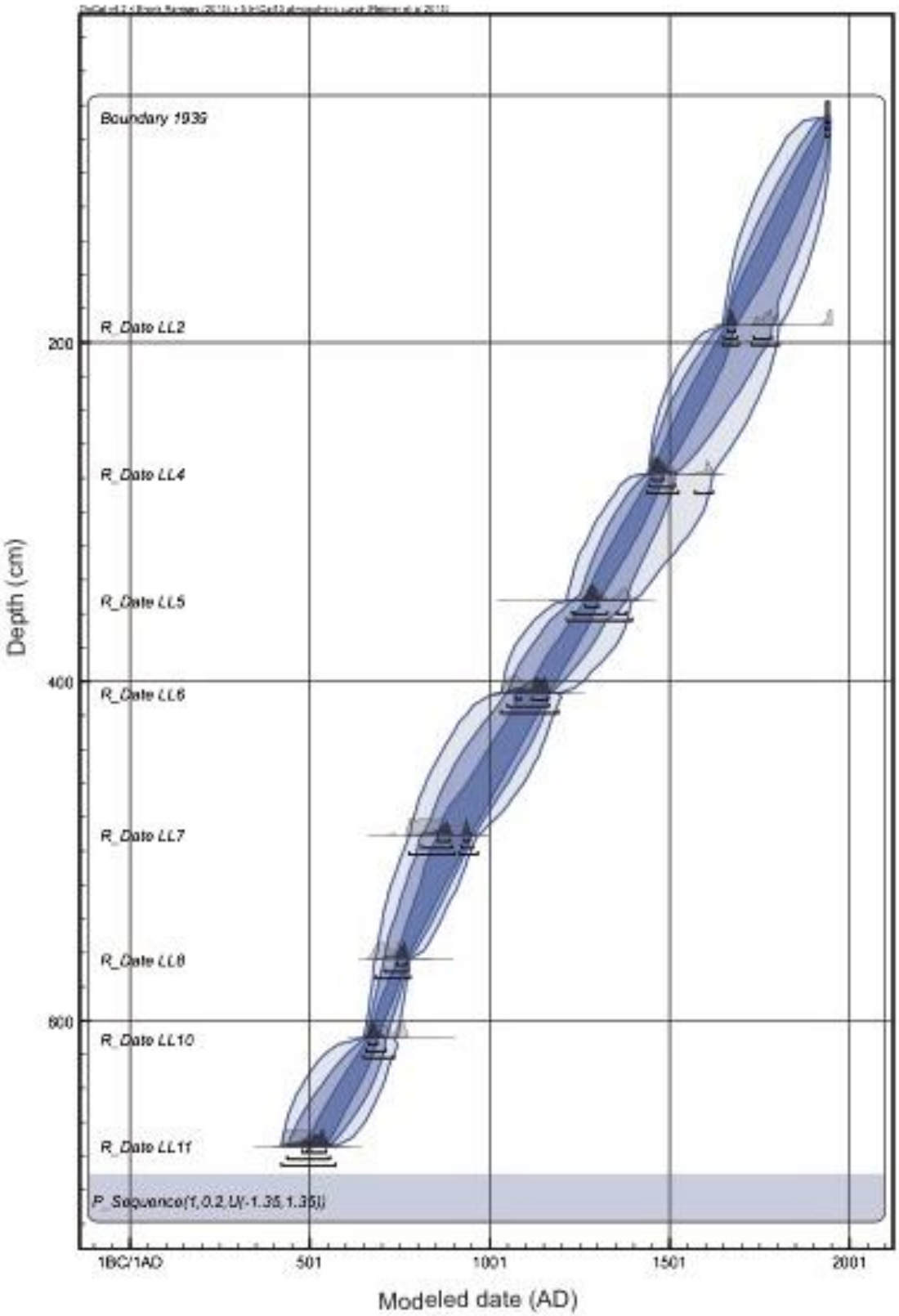
Boundary 1936
R_Date LL2
R_Date LL4
R_Date LL5
R_Date LL6
R_Date LL7
R_Date LL8
R_Date LL10
R_Date LL11
P_Sequence(1,0.2,U(-1.35,1.35))
Depth (cm)
200
400
600
1BC/1AD
501
1001
1501
2001
Modeled date (AD)

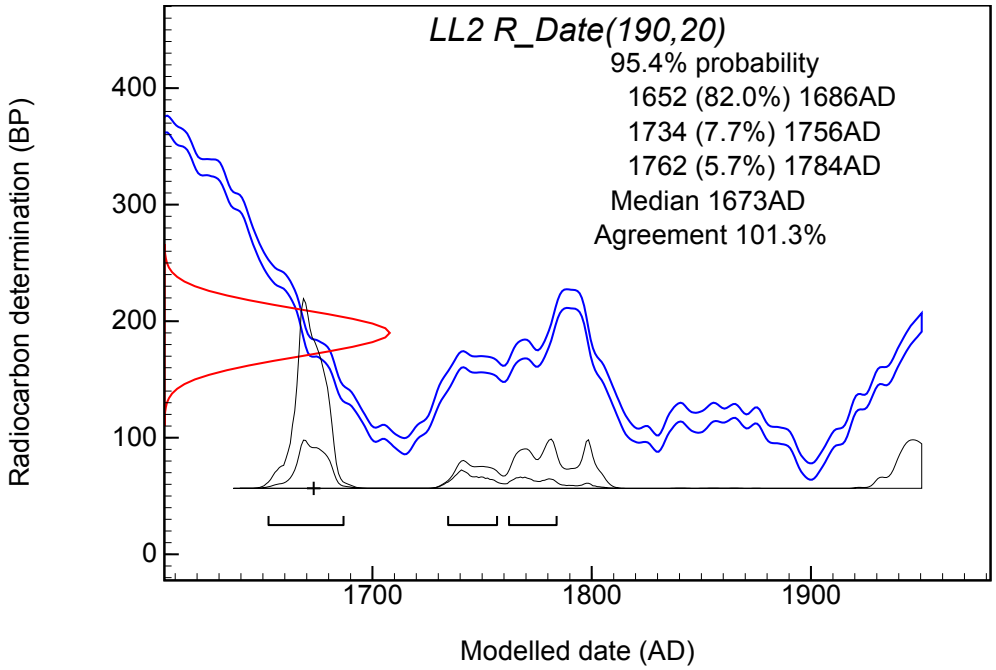

Figure A9. OxCal output of ^{14}C sample LL2 probability distributions. Blue line is the calibration curve, red distribution is the sample radiocarbon determination, light gray peaks are the likelihood probability distributions (the intersection of the unmodeled determination with the calibration curve), and dark gray peaks are the marginal posterior densities (the intersection of the OxCal modeled determination with the calibration curve), and brackets mark the 95.4% highest posterior density (hpd) range intervals. The far-right likelihood probability distribution interval (light gray, 1925 AD forward) was eliminated from the Monte Carlo resampling method when calculating accumulation rates. Source is Oxcal (Bronk Ramsey, 2013), based on the IntCal atmospheric curve (Reimer et al., 2013).

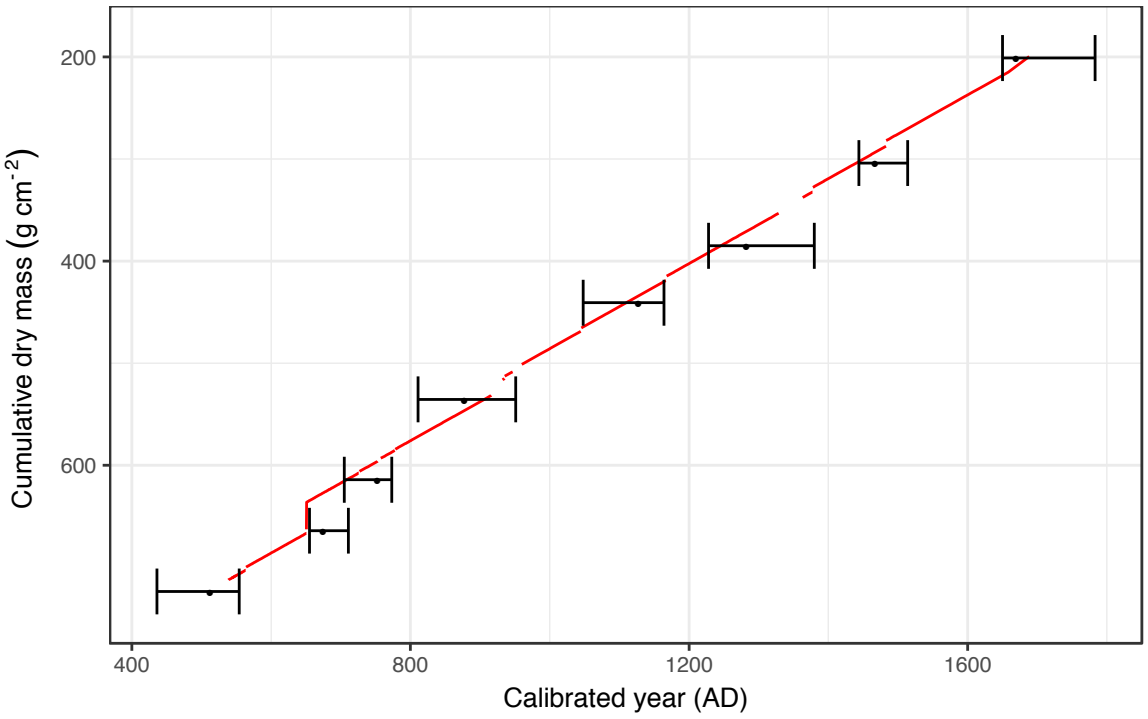

Figure A10. Age-mass model of early period. Calibrated ages for eight samples are shown in black, with the median indicated by a point, and approximate 95% highest posterior density (hpd) ranges as error bars. The red line through or near the hpd ranges is the generalized least squares regression of the calibrated ages when the 23 event beds are removed. Event beds are then replaced, evidenced by vertical regression line or gaps in the regression line. The prediction interval is shaded gray.

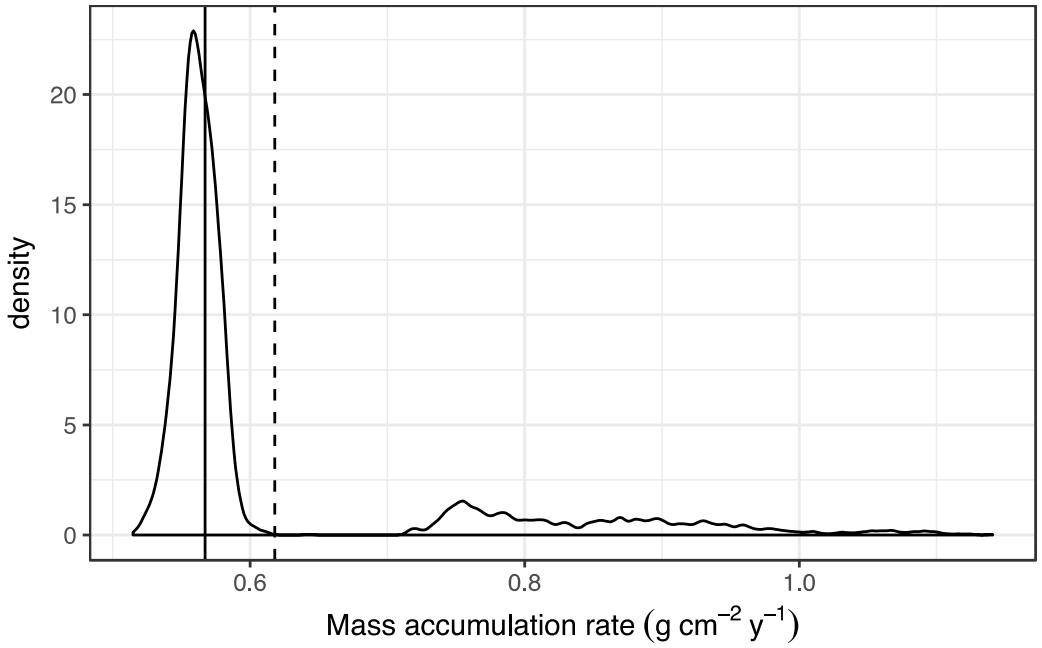

Figure A11. Distribution of mass accumulation rates between LL2 and 1939. Method is by Monte Carlo resampling of marginal posterior densities of modeled calibrated dates of ^{14}C sample LL2 and 1939 AD +/- 2y, with replacement, 5000 times. Solid line is the median of the distribution. Dashed line is the mean. The left mode of the distribution is the result of the draws from the left range of the LL2 distribution.

Table A2. Results of tests of difference in MAR. Dry mass accumulation rate (g cm^{-2} y^{-1}) of two sets of periods with different regression models are used. Each result includes the estimated mean rate (slope) and difference, 95% confidence interval (CI), F-test results with numbers of degrees of freedom, and models with normal coefficients and standardized coefficients (shaded). WY = water year; AM = accumulated mass (g cm^{-2}); Q = discharge (m^3 s^{-1}). Test is a separate lines model of multiple linear regression, where the regression is accomplished by generalized least squares and an AR1 autocorrelation function to account for autocorrelation.

MAR (all depths)			**MAR (EFD)**		
	Mean (CI) (g cm^{-2} y^{-1})	**Model**		**Mean (CI) (g cm^{-2} y^{-1})**	**Model**
2012-1979	0.59 (0.48-0.70)	AM = 0.59*WY	**2012-1979**	0.28 (0.24-0.33)	AM = 0.28*WY
(n=34)		AM = 12.67*WY	**(n=32)**		AM = 6.21*WY
1978-1939	0.83 (0.74-0.92)	AM = 0.83*WY	**1978-1939**	0.56 (0.38-0.74)	AM = 0.56*WY
(n=40)		AM = 17.79*WY	**(n=36)**		AM = 16.22*WY
Difference in slopes	0.24 (0.07-0.40)*		**Difference in slopes**	0.23 (0.09-0.34)*	
F-test	$F_{1,70}$=8.14, p=0.0057		**F-test**	$F_{1,64}$=8.77, p=0.0043	
2012-1979	0.59 (0.48-0.70)	AM = 0.59*WY + 0.0002*Q	**2012-1979**	0.28 (0.24-0.33)	AM = 0.28*WY + 0.0001*Q
(n=34)		AM = 12.66*WY + 0.26*Q	**(n=32)**		AM = 6.25*WY + 0.08*Q
1978-1939	0.83 (0.74-0.92)	AM = 0.83*WY + 0.0002*Q	**1978-1939**	0.57 (0.41-0.72)	AM = 0.57*WY + 0.0001*Q
(n=40)		AM = 17.17*WY + 0.26*Q	**(n=36)**		AM = 12.4*WY + 0.08*Q
Difference in slopes	0.24 (0.07-0.42)*		**Difference in slopes**	0.28 (0.12-0.44)*	
F-test	$F_{1,69}$=7.26, p=0.0088		**F-test**	$F_{1,,63}$=11.28, p=0.0013	

A7. Event bed and defined light layer thickness analysis

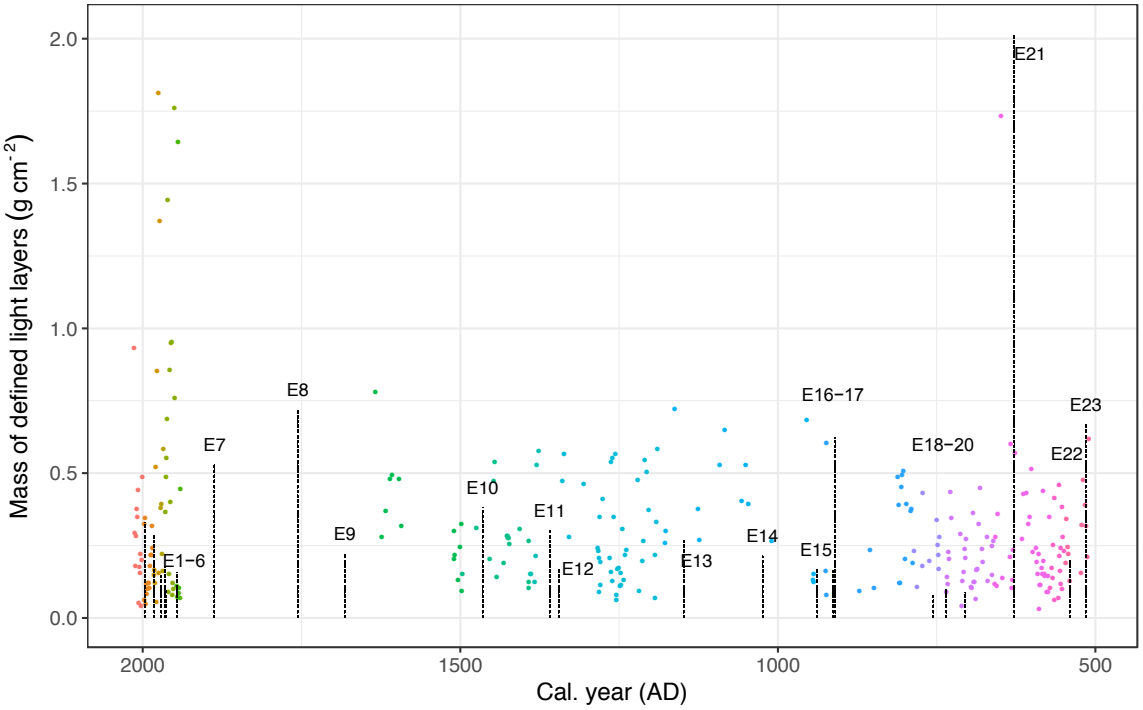

Figure A12. Mass of defined light layers and event beds through time. Mass of defined light layers are the colored points (left y-axis) and relative masses of event beds E1-E23 are the dashed vertical lines down core. To quantify mass of event beds, note that largest event E21 is 30.3 g of mass (Table 5), and all other event beds are relative to this mass. Colors of points change between events to emphasize any differences after events. Dates of layers are extrapolated before 515 AD, which is the median date of the ^{14}C sample at E23.

A8. Tools

Table A3. Crosswalk table for x-radiograph and MSCL depths. Correlated depths (cm) for Core 02aN between x-radiograph (CT) and Multi-Sensor Core Logger (MSCL). See Section 2.3.1 for explanation.

CT depth	MSCL depth	CT depth	MSCL depth	CT depth	MSCL depth	CT depth	MSCL depth	CT depth	MSCL depth	CT depth	MSCL depth
0	0	45	41	87	82	128	123	169	164	211	205
1	1	46	42	88	83	129	124	170	165	212	206
3	2	47	43	89	84	130	125	171	166	213	207
4	3	48	44	90	85	131	126	172	167	214	208
5	4	49	45	91	86	132	127	173	168	215	209
6	5	50	46	92	87	133	128	174	169	216	210
8	6	51	47	93	88	134	129	175	170	217	211
9	7	52	48	94	89	135	130	176	171	218	212
10	8	53	49	95	90	136	131	177	172	219	213
11	9	54	50	96	91	137	132	178	173	220	214
12	10	55	51	97	92	138	133	179	174	221	215
13	11	56	52	98	93	139	134	180	175	222	216
14	12	57	53	99	94	140	135	181	176	223	217
15	13	58	54	100	95	141	136	182	177	224	218
16	14	59	55	101	96	142	137	183	178	225	219
17	15	60	56	102	97	143	138	184	179	226	220
18	16	61	57	103	98	144	139	186	180	227	221
20	17	62	58	104	99	145	140	187	181	228	222
21	18	63	59	105	100	146	141	188	182	229	223
22	19	64	60	106	101	147	142	189	183	230	224
23	20	65	61	107	102	148	143	190	184	231	225
24	21	67	62	108	103	149	144	191	185	232	226
25	22	68	63	109	104	150	145	192	186	233	227
26	23	69	64	110	105	151	146	193	187	234	228
27	24	70	65	111	106	152	147	194	188	235	229
28	25	71	66	112	107	153	148	195	189	236	230
29	26	72	67	113	108	154	149	196	190	237	231
30	27	73	68	114	109	155	150	197	191	238	232
31	28	74	69	115	110	156	151	198	192	239	233
32	29	75	70	116	111	157	152	199	193	240	234
34	30	76	71	117	112	158	153	200	194	241	235
35	31	77	72	118	113	159	154	201	195	242	236
36	32	78	73	119	114	160	155	202	196	243	237
37	33	79	74	120	115	161	156	203	197	244	238
38	34	80	75	121	116	162	157	204	198	245	239
39	35	81	76	122	117	163	158	205	199	246	240
40	36	82	77	123	118	164	159	206	200	247	241
41	37	83	78	124	119	165	160	207	201	248	242
42	38	84	79	125	120	166	161	208	202	249	243
43	39	85	80	126	121	167	162	209	203	250	244
44	40	86	81	127	122	168	163	210	204	251	245

Table A3. (Continued)

CT depth	MSCL depth	CT depth	MSCL depth	CT depth	MSCL depth	CT depth	MSCL depth	CT depth	MSCL depth	CT depth	MSCL depth
252	246	293	287	334	328	375	369	416	410	458	451
253	247	294	288	335	329	376	370	417	411	459	452
254	248	295	289	336	330	377	371	418	412	460	453
255	249	296	290	337	331	378	372	419	413	461	454
256	250	297	291	338	332	379	373	420	414	462	455
257	251	298	292	339	333	380	374	421	415	463	456
258	252	299	293	340	334	381	375	422	416	464	457
259	253	300	294	341	335	382	376	423	417	465	458
260	254	301	295	342	336	383	377	424	418	466	459
261	255	302	296	343	337	384	378	425	419	467	460
262	256	303	297	344	338	385	379	426	420	468	461
263	257	304	298	345	339	386	380	427	421	469	462
264	258	305	299	346	340	387	381	428	422	470	463
265	259	306	300	347	341	388	382	429	423	471	464
266	260	307	301	348	342	389	383	430	424	472	465
267	261	308	302	349	343	390	384	431	425	473	466
268	262	309	303	350	344	391	385	432	426	474	467
269	263	310	304	351	345	392	386	433	427	475	468
270	264	311	305	352	346	393	387	434	428	476	469
271	265	312	306	353	347	394	388	435	429	477	470
272	266	313	307	354	348	395	389	436	430	478	471
273	267	314	308	355	349	396	390	437	431	479	472
274	268	315	309	356	350	397	391	438	432	480	473
275	269	316	310	357	351	398	392	439	433	481	474
276	270	317	311	358	352	399	393	440	434	482	475
277	271	318	312	359	353	400	394	441	435	483	476
278	272	319	313	360	354	401	395	442	436	484	477
279	273	320	314	361	355	402	396	443	437	485	478
280	274	321	315	362	356	403	397	444	438	486	479
281	275	322	316	363	357	404	398	445	439	487	480
282	276	323	317	364	358	405	399	446	440	488	481
283	277	324	318	365	359	406	400	447	441	489	482
284	278	325	319	366	360	407	401	448	442	490	483
285	279	326	320	367	361	408	402	449	443	491	484
286	280	327	321	368	362	409	403	450	444	492	485
287	281	328	322	369	363	410	404	452	445	493	486
288	282	329	323	370	364	411	405	453	446	494	487
289	283	330	324	371	365	412	406	454	447	495	488
290	284	331	325	372	366	413	407	455	448	496	489
291	285	332	326	373	367	414	408	456	449	497	490
292	286	333	327	374	368	415	409	457	450	498	491

Table A3. (Continued)

CT depth	MSCL depth	CT depth	MSCL depth	CT depth	MSCL depth	CT depth	MSCL depth	CT depth	MSCL depth
499	492	540	533	579	574	618	615	663	656
500	493	541	534	580	575	619	616	664	657
501	494	542	535	581	576	620	617	665	658
502	495	543	536	582	577	621	618	666	659
503	496	544	537	583	578	622	619	667	660
504	497	545	538	584	579	623	620	668	661
505	498	546	539	585	580	624	621	669	662
506	499	547	540	586	581	625	622	670	663
507	500	548	541	587	582	626	623	671	664
508	501	549	542	588	583	627	624	672	665
509	502	550	543	589	584	628	625	673	666
510	503	551	544	590	585	630	626	674	667
511	504	552	545	591	586	631	627	675	668
512	505	553	546	592	587	632	628	676	669
513	506	554	547	593	588	633	629	677	670
514	507	555	548	594	589	635	630	678	671
515	508	555	549	595	590	636	631	679	672
516	509	555	550	596	591	637	632	680	673
517	510	556	551	597	592	638	633	681	674
518	511	557	552	598	593	640	634	682	675
519	512	558	553	599	594	641	635	683	676
520	513	559	554	600	595	642	636	684	677
521	514	560	555	601	596	643	637	685	678
522	515	561	556	602	597	645	638	686	679
523	516	562	557	603	598	646	639	687	680
524	517	563	558	604	599	647	640	688	681
525	518	564	559	605	600	648	641	689	682
526	519	565	560	605	601	649	642	690	683
527	520	566	561	606	602	650	643	691	684
528	521	567	562	607	603	651	644	692	685
529	522	568	563	607	604	652	645	693	686
530	523	569	564	608	605	653	646	694	687
531	524	570	565	609	606	654	647	695	688
532	525	571	566	610	607	655	648	696	689
533	526	572	567	611	608	656	649	697	690
534	527	573	568	612	609	657	650	698	691
535	528	574	569	613	610	658	651	699	692
536	529	575	570	614	611	659	652	700	693
537	530	576	571	615	612	660	653	701	694
538	531	577	572	616	613	661	654		
539	532	578	573	617	614	662	655		

Figure A13. R-script for Monte Carlo resampling of posterior distributions

```
setwd("")
getwd()

# Work to resample from the posterior distributions of ages and fit a linear regression
  # many times in order to get an estimate of the mean accumulation rate as well as a CI

# Main part of code written by A. Muldoon; arfun_strat written by K. Richardson;
  # arfun_strat is a variant on the original code; it throws out impossible (out of
  # stratigraphic order) samples, and redraws.

library(tidyr)
library(dplyr)
library(ggplot2)

# Accumulated thickness:
posterior = read.csv("C14_postdist_18c_AT.csv", check.names = FALSE)
# csv has sample name, core depth, age, and probability

# subsets of the data, here all eight samples
posterior1102 <- posterior[posterior$depth %in% c("LL11", "LL10", "LL8", "LL7","LL6","LL5","LL4","LL2"), ]

# Function which removes the impossible SAR:
arfun_strat = function(data) {
  test <- data %>%
    group_by(depth) %>%
    sample_n(1, weight = probability) %>%
    ungroup() %>%
    arrange(coredepth)
  bad <- any(lag(test$age)-test$age <= 0, na.rm = TRUE) # results in noting if any are out of order
  while (bad == TRUE) {
    # do something
    test <- data %>%
      group_by(depth) %>%
      sample_n(1, weight = probability) %>%
      ungroup() %>%
      arrange(coredepth)
    # check for success
    bad <- any(lag(test$age)-test$age <= 0, na.rm = TRUE)
  }
  result <- lm(coredepth ~ I(-age), data = test)$coef[2]
  return(result)
}
# run once
arfun_strat(posterior1102)

# run many times
manyar_strat = replicate(5000, arfun_strat(posterior), simplify = TRUE)

# Check distribution, end result is pretty left skewed
qplot(manyar_strat, geom = "density")
qplot(manyar_strat, geom = "density", xlim = c(0,1))
summary(manyar_strat)

# Percentile based 95% CI from resampling monte carlo is just quantiles
quantile(manyar_strat, probs = c(.025, .975))

# Plot with median and 95% quantiles
ppi = 300
png('LL2_1939_mean.png', width=8*ppi, height=4*ppi, res=ppi)
qplot(manyar_strat, geom = "density") +
            geom_vline(xintercept = quantile(manyar_strat, probs = c(.025, .5, .975)))
qplot(manyar_strat, geom = "density", xlim = c(0,1)) +
  geom_vline(xintercept = quantile(manyar_strat, probs = c(.025, .5, .975)))
```

Figure A13. (Continued)

```
dev.off()

# Plot with mean instead of median
qplot(manyar_strat, geom = "density") +
              geom_vline(xintercept = quantile(manyar_strat, probs = c(.025, .975))) +
              geom_vline(xintercept = mean(manyar_strat))
qplot(manyar, geom = "density", xlim = c(0,1)) +
  geom_vline(xintercept = quantile(manyar, probs = c(.025, .975))) +
  geom_vline(xintercept = mean(manyar))

## a more sophisticated code by A. Muldoon ----

fun1.1 = function(data) {
  test1 = data %>%
    group_by(depth) %>%
    sample_n(1, weight = probability) %>%
    ungroup %>%
    arrange(-coredepth)

  while(any(with(test, age -  lag(age) <= 0), na.rm = TRUE) ) {
    test1 = data %>%
      group_by(depth) %>%
      sample_n(1, weight = probability) %>%
      ungroup %>%
      arrange(-coredepth)
  }

  lm(coredepth ~ I(-age), data = test1)$coef[2]
}

fun1.1(posterior)

# Run once
arfun()

# Run many times and save
manyar = unlist(replicate(5000, arfun(), simplify = TRUE))
qplot(manyar, geom = "density")
summary(manyar)
```